LUND UNIVERSITY

FACULTY OF SCIENCE

Characterisation of the position-sensitive ^{3}He-detector system of the BIFROST instrument at ESS

Auden Ti Yun

Thesis submitted for the degree of Master of Science, 60 hp
Project duration: 9 months

Supervisors: Irina Stefanescu and Kristina Stenström
Co-supervisor: Nicholai Mauritzson

Department of Physics
Division of Particle and Nuclear Physics
Autumn Semester 2023

Abstract

This scientific thesis focuses on the characterisation of the ^{3}He-detector system of the BIFROST instrument under construction on the European Spallation Source. To that end, the position-sensitive ^{3}He proportional counters that make up the detector system was subjected to a factory acceptance test performed at Laboratoire Léon Brillouin Saclay, France. The purpose of this is to prove that the overall performance of the ^{3}He-detector system meets the imposed requirements of the planned scientific studies that will utilise the BIFROST instrument. With the experimental results of the factory acceptance test as a foundation, the goals of this thesis work therefore is to first validate the read-out system, and subsequently, to characterise the position reconstruction performance of the detector system. The factory acceptance test consisted of separate neutron measurements with the three configurations that make up the BIFROST detector system. In each measurement, the ^{3}He proportional counters were covered with slitted cadmium masks, before being illuminated by an Am/Be neutron source. The analysis of these measurements yielded the position reconstruction resolution and intrinsic spatial resolution of the ^{3}He-detector system. These resolution results will serve as a benchmark during the commissioning phase of the BIFROST instrument, and for monitoring possible deterioration in the performance of the detector and associated read-out electronics due to long-term operation in high neutron fields.

Contents

List of Figures

List of Tables

List of Abbreviations

ADC	Analog-to-Digital Converter
Am/Be	Americium-Beryllium
CAMEA	Continuous Angle Multiple Energy Analysis
CANS	Compact Accelerator Based Neutron Sources
Cat6A	Augmented Category 6
Cd	Cadmium
CENDL	Chinese Evaluated Nuclear Data Library
ENDF	Evaluated Nuclear Data File
ESS	European Spallation Source
FPGA	Field Programmable Gate Array
FWHM	Full Width at Half Maximum
HV	High Voltage
ILL	Institut Laue-Langevin
LLB	Laboratoire Léon Brillouin
LV	Low Voltage
PC	Proportional Counter
PSD	Position Sensitive Detector
ROI	Region of Interest
SHV	Safe High Voltage

1 Introduction

This scientific thesis focuses on the characterisation of the ^{3}He-detector system of the BIFROST instrument at the European Spallation Source (ESS). The experimental work was performed at the Laboratoire Léon Brillouin (LLB) Saclay, France. The ^{3}He-detector system is an essential component of the BIFROST instrument, and therefore requires both qualitative and quantitative assessment of the performance of the position-sensitive detectors.

1.1 Background

The ESS, based in Lund, Sweden, is a multi-disciplinary research facility that is currently under construction. The facility, when operational, aims to be the brightest neutron source in the world using a pulsed spallation source. To accomplish this, firstly, a linear accelerator will be employed to deliver 2 GeV proton pulses with width of 2.86 ms, at a repetition rate of 14 Hz. Thereafter, the proton pulses impinge upon a rotating tungsten target, inducing a spallation reaction process. The fast neutrons produced by the process are then moderated to slow and cold neutrons using a moderator assembly consisting of both water and para-hydrogen. The proton pulses, combined with the moderation of the produced fast neutrons, result in a long-pulsed neutron source with a wide range of neutron energies. The monolith shielding containing the target and the moderator assembly is designed with 42 beam-ports wherein moderated neutrons may be extracted for use by neutron instruments. At present, 15 neutron instruments are selected to represent the initial instrument suite. The instruments can be further categorised for large-scale structures, imaging and engineering diffraction, diffraction, and spectroscopy [1].

The Detector Group, under the Technical Directorate at ESS, is tasked with both the development of neutron detectors, as well as the integration of neutron detectors contributed by the In-Kind partners, which are European research institutes that (on behalf of their national governments) supply equipment, documentation, personnel or other services to support the construction of ESS. One such neutron instrument is the BIFROST instrument, provided by a consortium consisting of the Technical University of Denmark, Copenhagen University, Institute for Energy Technology Norway, LLB Saclay, and Paul Scherrer Institute in Switzerland.

1.1.1 The BIFROST instrument

BIFROST is a cold-neutron, indirect geometry triple-axis spectrometer optimised to fully utilise the entirety of the long-pulsed neutrons. The 162 m long instrument is designed to study the dynamic properties of single-crystal samples subjected to extreme conditions of controlled temperature, pressure, and magnetic fields [2].

The beam transport and conditioning system, sample exposure system, and scattering characterisation system make up the three main subsystems of the instrument. The beam trans-

port and conditioning system consists of choppers that shape, and guides that transport the neutron pulse to the desired energy resolution, while the sample exposure system creates the desired environment for the sample. The scattering characterisation system consists of a filtering system, and a secondary spectrometer tank that covers a 90° scattering angle in two settings. A 3D model of the sample exposure system and scattering characterisation system is presented in Figure 1.1 (a). The purpose of the filtering system is to maximise the signal-to-noise ratio and reduce the neutron background by permitting mostly cold neutrons with energy below 5 meV to be transmitted [3]. The secondary spectrometer tank houses corresponding sets of pyrolytic graphite analysers and ^{3}He-detectors that are arranged in nine different scattering angles, known as Q-channels, realising a novel prismatic analyser concept known as Continuous Angle Multiple Energy Analysis (CAMEA) [4, 5].

A schematic diagram depicting the travel path of the neutron beam from sample to analyser to detector is illustrated in Figure 1.1 (b). The prismatic analyser concept requires each set of analysers to be placed at different angles with respect to the neutron beam axis, such that cold neutrons with different, fixed, final energies may be reflected toward the position-sensitive ^{3}He-detectors. To realise this concept, pyrolytic graphite is chosen for both its good reflectivity for cold neutrons, and very high transmission, such that cold neutrons of higher energies that are not reflected may transmit to the next set of analysers. Additionally, the beam of cold neutrons that is reflected off an analyser is Gaussian-shaped, and therefore includes slightly different energies around the mean design energy of each analyser. To account for this, each ^{3}He-detector is comprised of three side-by-side position-sensitive ^{3}He-tubes, forming a ^{3}He-triplet. In order to maximise the scattering angle coverage and minimise the scattering background and gaps between the ^{3}He-detectors, different lengths of ^{3}He-triplets are employed, positioned radially within the secondary spectrometer tank. Furthermore, cadmium (Cd) -sheets line each beam path from the set of analysers to the ^{3}He-detectors to provide cross-talk shielding. Cross-talk, in this context, refers to unwanted neutron transition between beam paths.

A sketch of the sample-analyser-detector geometry, Figure 1.1 (c), illustrates the prismatic analyser concept for the BIFROST instrument. Figure 1.1 (d) is an energy spectrum created from the results of a McStas simulation of the time-of-flight of the reflected 5.0 meV cold neutrons that are detected by a ^{3}He-triplet [6]. The spectrum features three Gaussian-shaped peaks, wherein their respective centroids is defined by the three regions of the analyser in which the cold neutrons are reflected. For the BIFROST instrument, the expected position reconstruction resolution along the ^{3}He-triplet is $\sim 1\%$ the total length of three ^{3}He-tubes. Extensive discussion on the BIFROST instrument is available at [1, 2].

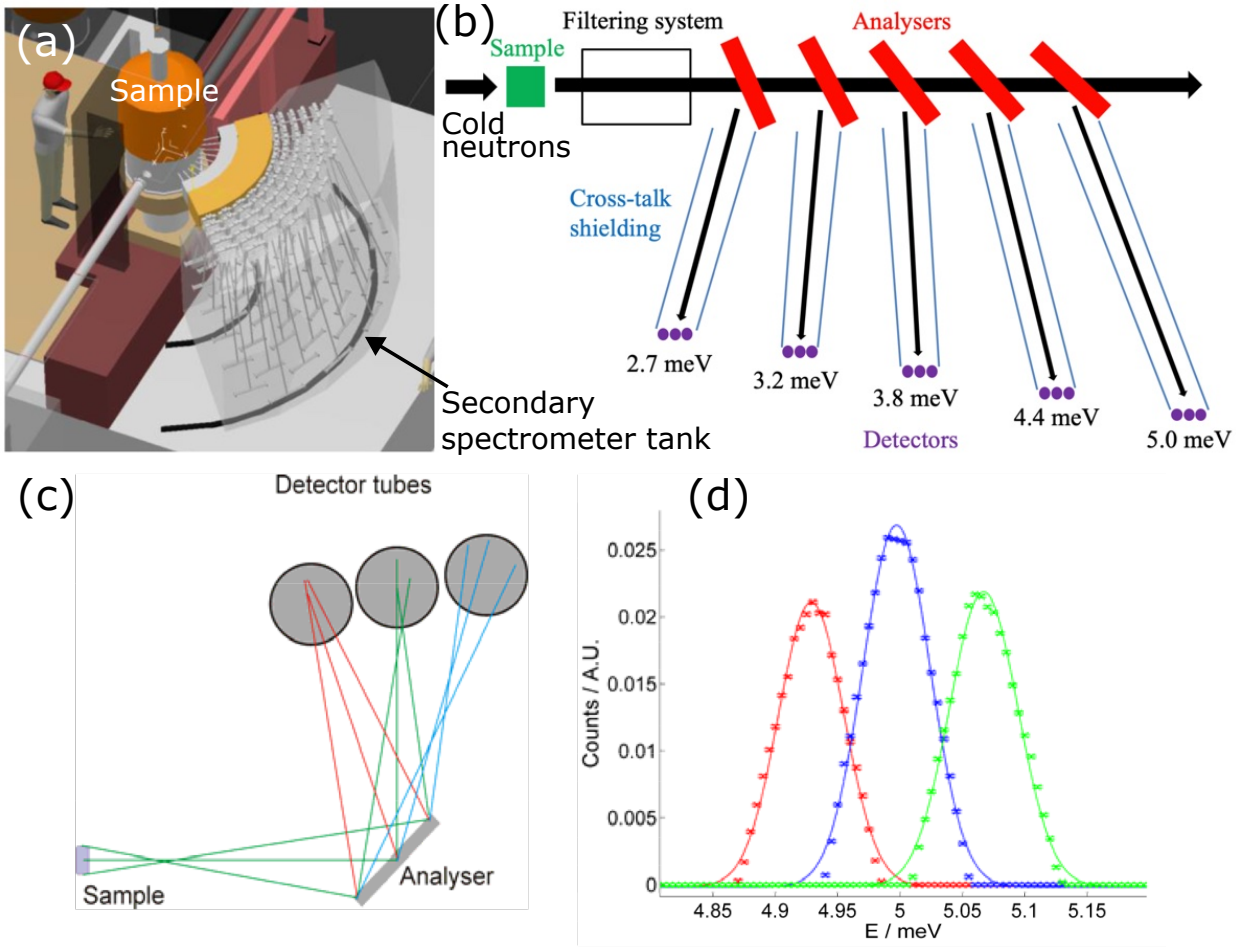

Figure 1.1: The BIFROST sample exposure system and scattering characterisation system. (a) 3D model of the two systems. (b) Side-view schematic diagram of the two systems. The black arrows signify the travel paths of the cold neutrons. Figures adapted from [2]. (c) Sample-analyser-detector geometry. The cold neutron beam scattered by the sample is reflected by an analyser to a ^{3}He-triplet (detector tubes). (d) Energy spectrum created from the results of a McStas simulation of the time-of-flight of 5.0 meV cold neutrons. In both (c) and (d), the slightly different energies are represented by the different colours. Figures taken from [6].

1.2 Project Goals and Motivation

The BIFROST instrument is currently in an advanced construction phase, and is expected to begin cold commissioning in the third-quarter of 2024. Cold commissioning refers to the operation of the instrument without a neutron source (i.e. background/cosmic measurements). At the time of writing, several instrument components designed and manufactured by the external partners are currently undergoing inspection tests at partner sites before delivery to ESS for installation. The ^{3}He-detector system, consisting of a total of 45×3 position-sensitive ^{3}He-tubes and the read-out system, is planned to arrive at ESS before the end of 2023. The ^{3}He-tubes were delivered by the American company Baker-Hughes (formerly Reuter-Stokes) and assembled in ^{3}He-triplets by the in-kind partner LLB Saclay. The associated read-out system was designed and built by the Electronics Group of Institut Laue-Langevin (ILL) in Grenoble.

The experimental work detailed in this thesis is the factory acceptance test of the BIFROST

detector system performed at LLB Saclay in September 2023 and was attended by the author. The aim of the test was to prove the overall performance of the detector system, composed of parts developed by different partners, with a specific focus on determining the position resolution of the ^{3}He-triplets. The expected position resolution is $\sim$1% of the total length of a ^{3}He-tube, serving as an important parameter for achieving the performance requirements imposed by the science cases of the BIFROST instrument.

This thesis presents the final results of the data analysis of the collected measurement data, which will be used to benchmark the results of similar testing that will be performed during the commissioning phase of the instrument. Additionally, when the ESS facility is operational, the evaluated position resolution of the ^{3}He-triplets will serve to monitor the long-term performance of the detector system and associated read-out electronics in high neutron field environments. The specific project goals of this thesis can therefore be defined as:

1. Validation of the digital pulse processing read-out system.
2. Determination of the performance of the position reconstruction of the ^{3}He-detector system.
3. Providing support for the approval of the factory acceptance test of the ^{3}He-detector system.

Project goal 1 is motivated by the novel digitiser utilised in the read-out system developed by CAEN and In-Kind partner Science and Technology Facilities Council for selected instruments at ESS, such as the BIFROST instrument. As such, there is a need to operate the read-out system in an experimental environment where multiple concurrent read-outs are sent to the digitiser. Although knowledge of the performance of position reconstruction of each individual ^{3}He-tube is available from the manufacturer, the detector system consists of ^{3}He-tubes that are electrically joined to form ^{3}He-triplets. Therefore, there is a need to determine if the position reconstruction performance is affected, hence motivating project goal 2. As an integral part of the BIFROST instrument, the ^{3}He detector system has to fulfil operational and performance requirements in order to pass the factory acceptance test. The motivation for project goal 3 is therefore to present supporting conclusions obtained from the analysis of the data from the experimental measurements performed during the test.

1.3 Thesis Structure

Following this introduction, Chapter 2 outlines the theoretical background relevant to the project work, encompassing the fundamentals of nuclear structure, neutrons, and digital pulse processing. Next, Chapter 3 describes the experimental set-up at LLB Saclay, France, and the slow neutron measurements performed. In Chapter 4, the results of the slow neutron measurements are presented and discussed. Finally, Chapter 5 summarises the project work, reflects upon the project goals, and provides recommendations for future work.

2 Theoretical Background

This chapter provides the theoretical background relevant to the experimental work. First, the nuclear structure of the atom is discussed, followed by an introduction of the free neutron, and detailed discussions of the interaction, production, and detection of free neutrons. The chapter ends with an introduction to digital pulse processing. As these topics are extensive, a summarised overview of each is instead presented.

2.1 Nuclear Structure

The building block of all materials that exist, the atom, is made up of neutrons [7], protons [8], and electrons [9]. The nucleus of an atom is composed of both neutrons and protons, collectively called nucleons, that are held together by the strong nuclear force.

Different atomic species can be identified with the number of protons (atomic number Z) and neutrons (N), where the sum of both gives the atomic mass number A. The atomic number Z determines the chemical element, and at present there is a total of 118 chemical elements recognised by the International Union of Pure and Applied Chemistry [10]. Additionally, the number of neutrons in the nucleus determines the isotope of the chemical element. A nuclide is defined as a chemical element with a specific atomic mass number A, and atomic number Z. As an example, one of the most prominent media for neutron detection, which is discussed further in Section 2.2.4, is the ${}^{A=3}_{Z=2}\mathrm{He}$ (helium-3) nuclide in its gaseous state.

The semi-empirical mass formula [11–14] approximately describes the binding energy (E_B) of nuclides as a function of the atomic mass number A, and atomic number Z. The formula contains five terms, namely, the volume term, surface term, Coulomb term, asymmetry term, and the pairing term. The first three terms are based on the liquid-drop model [11], which classically describes the nuclide as a charged liquid droplet. The latter two terms are based on the nuclear shell model [15–19], which provides a description of the individual nucleons in a nuclide. The semi-empirical mass formula is [20]:

$$E_B = a_{\mathrm{v}}A - a_{\mathrm{s}}A^{2/3} - a_{\mathrm{c}}\frac{Z^2}{A^{1/3}} - a_{\mathrm{sym}}\frac{(2Z-A)^2}{A} \pm a_{\mathrm{p}}\frac{((-1)^Z + (-1)^{(A-Z)})}{2A^{1/2}} \tag{2.1}$$

where the lower-case a terms and associated subscripts are the respective coefficients of each of the five terms. The coefficients are obtained from fitting the formula to experimental data, and is updated accordingly to the latest improved experimental measurements of the binding energies of different nuclides. Further reading is available in [20–22].

Nuclides with an atomic mass number $A \approx 60$ are the most tightly bound with respect to their binding energy per nucleon. To reach this peak, lighter nuclides have to fuse together to form heavier nuclides (nuclear fusion), while heavier nuclides have to break into lighter nuclides (nuclear fission). In either case, the resultant nuclide may be unstable, and therefore needs to decay via the emission of particle(s) and/or electromagnetic radiation in order to become stable. In this thesis, the various decay mechanisms form the basis for free neutron sources discussed in Section 2.2.3.

The main types of decay are α-decay with the emission of a ^{4}He nuclide, β-decay with the emission of an electron (β^--decay) or a positron (β^+-decay), and γ-decay with the emission of a γ-ray. There are also other avenues of decay, such as electron capture, internal conversion, nucleon emission, and spontaneous fission of heavy nuclides. More information of the various types of decay processes can be found in [23, 24].

2.1.1 Excited States and Compound Nucleus Model

The nucleus of an atom can be defined as a system with discrete energy states using the nuclear shell model [25]. To transition from a higher energy state to a lower energy state, a γ-ray may be emitted possessing the energy difference between the two energy states. The most energetically stable state for a nucleus is the ground state, and a nucleus with a high energy state may de-excite to its ground state either directly, with the emission of a single γ-ray, or indirectly. For indirect transitions, multiple γ-rays may be emitted as the nucleus transitions to lower energy states in a step-wise fashion until the nucleus reaches its ground state. Additionally, the electromagnetic process of internal conversion is a competing process to the emission of γ-ray(s), where a nucleus in an excited state may also interact directly with its bounded atomic electrons, emitting instead the now free electron. Detailed discussions of γ-ray transitions, and internal conversion can be found in [22, 25–27].

Following a particle-induced reaction to a parent nuclide, the daughter nuclide may be left in an excited state, and one or more γ-rays may be emitted for the daughter nuclide to reach its ground state. The compound nucleus model [28] extends this reaction process with the addition of an intermediate two-step process, where the incident particle becomes a part of a parent nuclide, forming a new, highly excited, and unstable, compound nucleus. The compound nucleus then decays into the daughter nuclide and other particle products such as nucleons. Further discussion of compound nuclei is available in [28, 29].

2.2 Neutrons

2.2.1 Neutron Interactions with Matter

A free neutron, when not bound in nuclei, is unstable and has a half-life of about 10 minutes, after which it undergoes β^--decay with a Q-value of $\sim 0.782\,\text{MeV}$ [30]. Since the neutron has no electric charge, a free neutron does not interact with atomic electrons or nuclei via Coulomb interactions. Instead, a free neutron interacts via the strong force only at length scales below $\sim 10^{-15}\,\text{m}$. Neutron-nuclei interactions, consequently, are therefore much less likely to occur [31].

The possible types of neutron-nuclei interactions are [30–32]:

Nuclear Scattering

- Nuclear elastic scattering - (n, n)
  - The incident free neutron loses a part of its kinetic energy from scattering with the target nuclei. The nuclei gain energy, and the total kinetic energy and momentum is conserved.
- Nuclear inelastic scattering - (n, n')
  - The incident free neutron loses kinetic energy from scattering with the target nuclei. Unlike nuclear elastic scattering, the free neutron has sufficient energy to raise the target nuclei to an excited state. The total kinetic energy is not conserved, but the total momentum is conserved. The excited nuclei decays to ground state by photon emission or internal conversion.

Neutron Capture

- Radiative Neutron Capture - (n, γ)
  - The incident free neutron is captured by the target nuclei. The resultant daughter nucleus may be in an excited state, and decay to ground state by emission of γ-ray(s).
- Fission - (n, fission)
  - The target nucleus ($Z > 80$) captures the incident free neutron, resulting in an excited compound nucleus that splits into two daughter nuclei and secondary particles (usually a few neutrons).
- Other reactions - e.g. (n, p), (n, α), etc.
  - The incident free neutron is captured by the target nuclei, which emits charged particle(s).

2.2.2 Neutron Energy and Cross-Section

The probability of the aforementioned types of neutron-nuclei interactions in Section 2.2.1 is heavily dependent on the incident free neutron energy. As a result, free neutrons are generally classified by their kinetic energy:

- Fast neutrons - above 100 keV
- Slow neutrons - lower than 10 eV
- Thermal neutrons - 0.025 eV
- Cold neutrons - between 5×10^{-5} eV to 0.025 eV.

For fast neutrons, nuclear elastic and inelastic scattering are the primary interaction mechanisms. In elastic scattering (n, n), the fast neutrons are effectively *moderated* with each scattering event, resulting in neutrons with lower kinetic energies. At high enough energies ($>1\,\mathrm{MeV}$), inelastic scattering (n, n') interactions may occur. As more energy is required to excite the target nuclei, the exiting neutron loses a larger part of its initial energy than an equivalent elastic scattering event.

For slow neutrons, elastic scattering and neutron capture interactions are the primary mechanisms. However, due to the lower neutron energies, elastic scattering events do not impart as much energy to the target nuclei, and therefore much of the slow neutron population resides around the thermal-neutron energy range.

The cross-section, σ, describes the probability of an interaction, and is given by the unit of *barn* ($1\,\mathrm{b} = 10^{-28}\,\mathrm{m}^2$). The cross-section is dependent on both the target nuclei and the neutron energy, and therefore the *total* cross-section of any target nuclei at any incident neutron energy is defined as a combination of the individual cross-sections of the different possible neutron-nuclei interactions:

$$\sigma_{\mathrm{tot}} = \sigma_{\mathrm{elastic}} + \sigma_{\mathrm{inelastic}} + \sigma_{\mathrm{rad.\ capture}} + \dots \tag{2.2}$$

Generally, the cross-section of neutron capture reactions is approximately related to $1/\nu$, where ν is the velocity of the incident neutron. Figure 2.1 presents the neutron capture cross-sections of various nuclides that are commonly found in neutron detectors and neutron absorbers. These nuclides are chosen both for their high cross-sections, and high Q-value of the neutron capture reaction, where the Q-value energy is shared between the reaction products, proportional to their masses. The higher the Q-value, the greater the energy of the reaction products, allowing for easier discrimination against low energy γ-rays (such as from (n, γ) reactions, see Figure 2.3 (b)).

The ^{3}He (helium-3) thermal-neutron capture reaction is considered the "gold-standard" for thermal-neutron detectors, with a cross-section of $\sim 5333\,\mathrm{b}$ and a Q-value of $0.764\,\mathrm{MeV}$. As ^{3}He is a noble gas, it can only be employed in gaseous form in neutron detectors, and its supply of which is becoming scarce [33]. An alternative is ^{10}B (boron-10), which has a thermal-neutron cross-section of $\sim 3840\,\mathrm{b}$, with Q-values of $2.792\,\mathrm{MeV}$, or $2.310\,\mathrm{MeV}$ if the reaction product ^{7}Li (lithium-7) is produced in its first excited state. Another alternative is ^{6}Li (lithium-6), which has a thermal-neutron cross-section of $\sim 940\,\mathrm{b}$, and a Q-value of $4.78\,\mathrm{MeV}$.

Among the highest thermal-neutron capture cross-section is ^{157}Gd (gadolinium-157) at $\sim 255\,000\,\mathrm{b}$, where the reaction products are γ-rays and internal conversion electrons. The γ-ray product, however, may create a problematic γ-ray background component that requires discrimination techniques in order to obtain information of the incident free neutrons from the internal conversion electrons. Instead, ^{157}Gd is utilised in the application of neutron imaging, where the electrons leave tracks on e.g. a photographic film, recording the position of the thermal-neutron capture reaction.

The high cross-section for neutron capture of (n, γ)- or (n, α)-type reactions can also be utilised for the purposes of neutron shielding. Neutron absorbers can be used for neutron shielding, or included in the design of neutron detectors to minimise the background component from uncorrelated neutrons. One such example is ^{113}Cd (cadmium-113), which has a thermal-neutron capture cross-section of $200\,000\,\mathrm{b}$, with reaction products of γ-rays and a stable ^{114}Cd (cadmium-114) nuclide. Another example is borated polyethylene, where boron

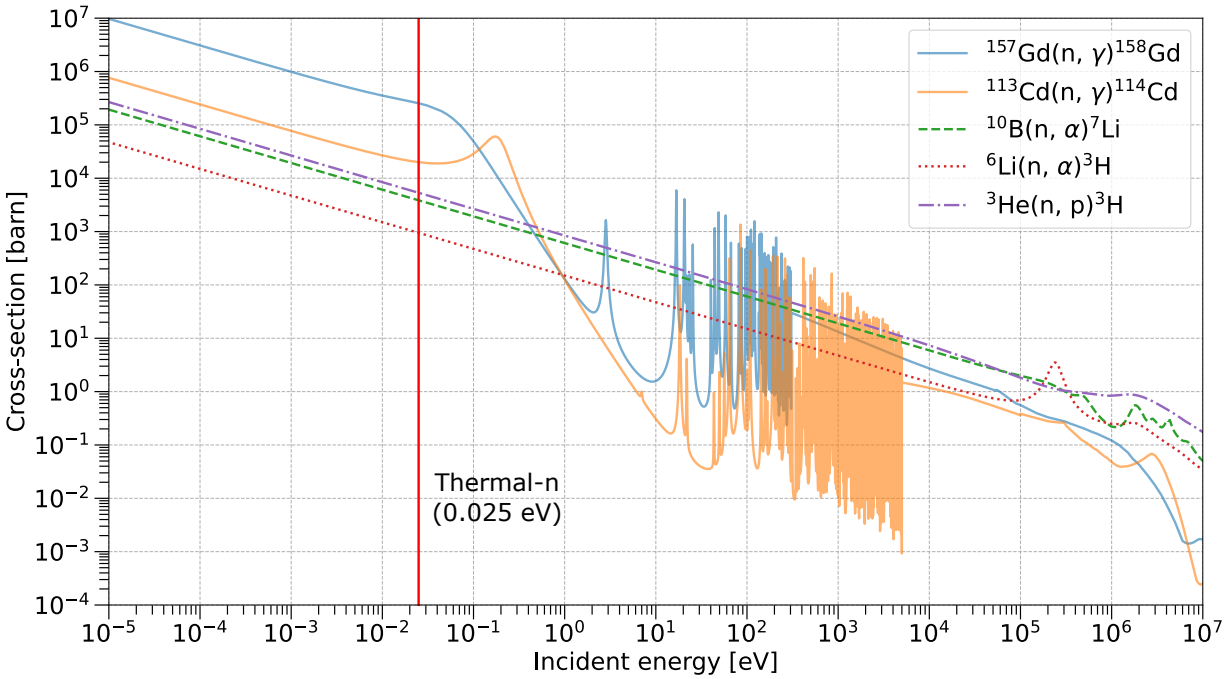

Figure 2.1: Neutron capture cross-sections of various nuclides as a function of the incident neutron energy. The red vertical line shows the thermal-neutron energy. Data retrieved from Evaluated Nuclear Data File (ENDF) [36] and Chinese Evaluated Nuclear Data Library (CENDL) [37] databases.

is mixed into polyethylene in the form of boron carbide (B_4C).

Further reading of thermal-neutron detection media are available in [34, 35].

2.2.3 Sources of Free Neutrons

There are various sources of free neutrons that can be classified by the way the neutrons are produced, these include radioisotopic decay, spontaneous or induced fission reactions, nuclear reactions from accelerated charged-particles, and photo-neutron sources.

Radioisotope sources produce neutrons through nuclear reactions such as (α, n). A common radioisotope source is the Americium-Beryllium (Am/Be) neutron source, which is used in the experimental work of this thesis. The reactions are summarised as [38, 39]:

$$
\begin{aligned}
^{241}\mathrm{Am} &\longrightarrow {}^{237}\mathrm{Np} + \alpha \qquad \text{Q-value} = 5.71\,\mathrm{MeV} \\
^{9}\mathrm{Be} + \alpha &\longrightarrow {}^{13}\mathrm{C}^{*} \longrightarrow \begin{cases} {}^{12}\mathrm{C}^{*} + \mathrm{n} + 4.44\,\mathrm{MeV}\ \gamma\text{-ray} \\ {}^{12}\mathrm{C} + \mathrm{n} \end{cases}
\end{aligned}
\tag{2.3}
$$

The ^{241}Am (americium-241) nuclide decays via α-decay to its daughter nuclide ^{237}Np (neptunium-237) and an α-particle. The α-particle is then absorbed by ^{9}Be (beryllium-9) to form the excited compound nucleus ^{13}C* (carbon-13), which quickly decays into different routes depending on the compound nucleus's excitation energy. The dominant decay routes are either to the ground state or the first excited state of ^{12}C (carbon-12). The first excited state ^{12}C* decays to ground state by emission of a 4.44 MeV γ-ray. In both cases, a free neutron is

emitted. The neutron has an energy range $\sim 0-11\,\text{MeV}$, and average energy of $\sim 4\,\text{MeV}$ [40].

Nuclear reactions from accelerated charged-particles consists of, but are not limited to, spallation sources, neutron generators, and Compact Accelerator Based Neutron Sources (CANS). Specifically, spallation sources utilise accelerated charged-particles that impinge on a heavy nuclei target at high energies to induce a spallation reaction [41, 42]. Spallation reactions encompass a string of complex reactions that can be categorised into various stages, with the ultimate goal of producing a considerable amount of free neutrons. The high-energy particles used are usually protons that have been accelerated with a linear accelerator to energies of $> 1\,\text{GeV}$. Figure 2.2 illustrates the stages of the spallation process using an accelerated proton beam.

The first stage, referred to as intranuclear cascade, begins when a highly energetic proton collides with the target nuclei, leaving the target nuclei in a highly excited state. At this stage, the excess energy may give rise to proton, neutron and pion emissions with sufficient energy to collide into other nuclei and further create more excited nuclei. This cascading process continues until there is insufficient energy to excite further nuclei. The second stage comprises of two competing processes, evaporation and fission, which describe how the highly excited nuclei decays in order to become stable (discussed in Section 2.1). The evaporation process involves the de-excitation of the excited target nuclei. The excited nuclei lose their energies by "evaporating" mainly neutrons, but also other particles such as deuterons, protons and/or α-particles. Fission, on the other hand, occurs when neutrons emitted from the first stage are captured by other target nuclei, resulting in the splitting of the nuclei into two daughter nuclei, and may include the emission of further neutrons and other particles. The final stage, referred to as residual de-excitation, is when the nuclei decays via β-decay and γ-ray emission, giving the final spallation/fission product(s).

As introduced in Section 1.1, the ESS is one such spallation source facility which is currently under construction. The solid heavy metal tungsten is chosen as a target for its high neutron yield (~ 35 neutrons per proton at $2\,\text{GeV}$ [43]) due to its high density and atomic mass, as well as favourable physical properties such as good thermal conductivity [44]. Quantitatively, the ESS facility is expected to deliver around 2 magnitudes of thermal neutron flux (neutron/cm^2/s) higher than that delivered by fission research reactors.

More detailed descriptions of the various sources of free neutrons are available in [38, 39, 41].

2.2.4 Neutron Detection

Neutron detection techniques are indirect, where information of incident neutrons are inferred from secondary radiation emitted via neutron-nuclei interactions described in Section 2.2.1. There are several types of neutron detection techniques available (but not limited to): proportional counters (PCs), scintillation detectors, and semiconductor detectors.

The PC belongs to the family of ionisation detectors, where incident neutrons interact with the gas-filled detector, producing free electrons and ions. The charge of the electron-ion pairs is amplified through gas multiplication, and the final induced charge is proportional to the produced number of original electron-ion pairs. This proportionality property, obtained from operating in the proportional region, separates the PC from its siblings, the ionisation chamber, which does not apply any amplification, and the Geiger-Müller counter, which amplifies the electron-ion pairs to an extent where proportionality to energy deposition is lost.

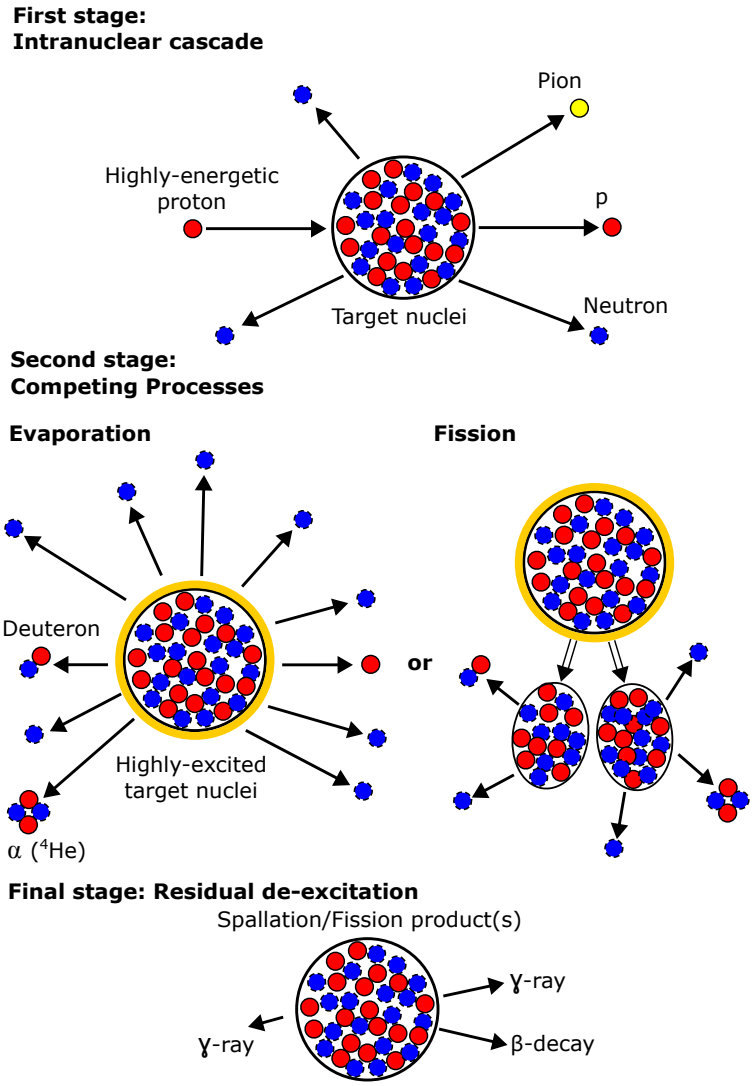

Figure 2.2: The stages of the spallation process. In the second stage, evaporation and fission are competing processes. Adapted from [41].

In a PC, the applied high-voltage (HV) creates an electric field that is the strongest at the anode wire located at the centre of the PC. Figure 2.3 (a) illustrates a schematic diagram of a typical gas-filled PC. When incident neutrons react with the fill gas, the reaction products subsequently produce electron-ion pairs. The free electrons are accelerated to the anode wire, while the ions drift towards the cathode wall. The accelerated free electrons may collide with the gas, producing secondary ionised electrons close to the anode wire. This gas multiplication process creates a cascading effect called the Townsend avalanche [45]. The movement of the free electrons and ions induce current pulses [46] that are registered by the pulse processing system (see Section 2.3).

The inert ^{3}He gas is one of the most commonly used fill gases for a thermal-neutron PC due to its high thermal-neutron capture cross-section of $\sim$5333 barns. The (n, p) neutron capture process is:

$$^3\mathrm{He} + {}^1\mathrm{n} \longrightarrow {}^3\mathrm{H} + {}^1\mathrm{p} \qquad \text{Q-value} = 0.764\,\mathrm{MeV} \tag{2.4}$$

The Q-value is shared between the reactions products as kinetic energy, where the lighter proton (^{1}p) has energy $E_\mathrm{p} = 0.573$ MeV, and the heavier triton (^{3}H) has energy $E_\mathrm{H} = 0.191$ MeV. Figure 2.3 (b) is the expected pulse-height spectrum from a ^{3}He PC purposed for neutron

counting. Contributors such as fast neutrons, γ-rays, and electronic noise lead to noise at low energies of the spectrum. At higher energies, slow neutrons undergo the (n, p) neutron capture process, creating a double-plateau feature ending with a *full-energy* peak.

The double-plateau feature is a result of the *wall effect*, and can be described by considering the combination of two different cases. In the first case, the triton nuclide fully deposits its energy in the PC, forming the edge of the lower plateau at 0.191 MeV. The proton may deposit part of its energy before escaping the walls of the PC, or it may fully deposit its energy, creating a continuous range of deposited energy, from $(E_{\mathrm{H}} + 0)$ to $(E_{\mathrm{H}} + E_{\mathrm{p}})$. In the second case, the roles are swapped, where the proton instead fully deposits its energy in the PC, forming the edge of the higher plateau at 0.573 MeV. The triton nuclide, in this case, may deposit some part or all of its energy within the PC, creating a continuous range from $(E_{\mathrm{p}} + 0)$ to $(E_{\mathrm{H}} + E_{\mathrm{p}})$. By combining these two energy deposition cases, the double-plateau feature shown in Figure 2.3 (b) is formed as a continuous range of the combined deposited energies of both reaction products, ending with a full-energy peak where both reaction products deposit their energies fully within the PC.

The ^{3}He gas-filled PC is designed to be used as a thermal neutron counter, which counts the number of thermal neutrons that have interacted with the fill gas, but any information about the neutrons kinetic energy is lost in the conversion. Further reading about neutron detectors, the phenomena of gas multiplication and application for PCs are available in [23, 26, 34, 46].

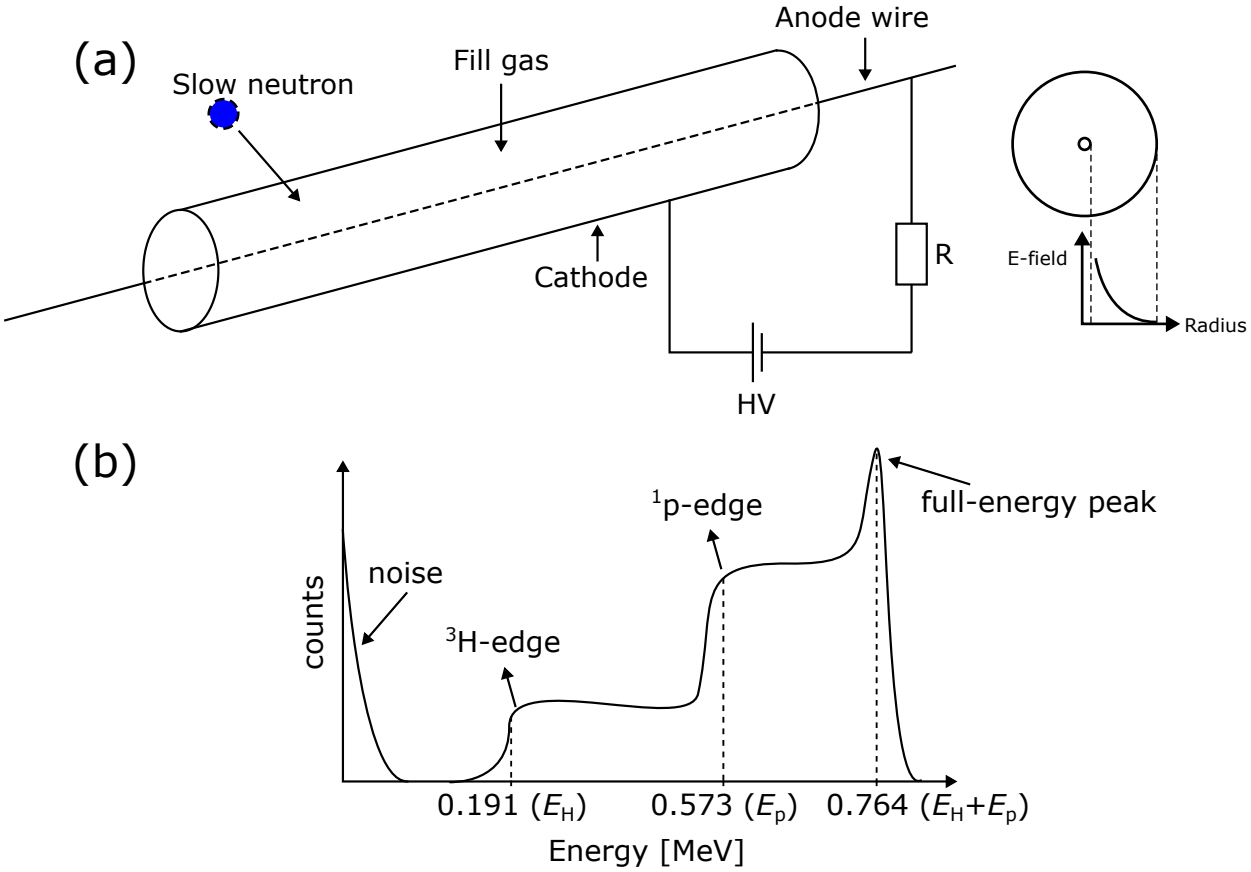

Figure 2.3: (a) Schematic diagram of a typical cylindrical gas-filled PC with an incident slow neutron. To the right is the electric field as a function of the radius of the cylinder. (b) The expected pulse-height spectrum of a ^{3}He gas-filled PC.

2.2.5 Position-Sensitive ^{3}He PC

The ^{3}He gas-filled PC introduced in Section 2.2.4 can be extended with the function of position-sensitivity. These detectors are called position-sensitive detectors (PSD), where a resistive anode wire is used. By having a preamplifier on each end of the anode wire, the collected charge pulses can be divided between the two ends, allowing for the position reconstruction of the neutron capture event along the detector, through charge-division:

$$\mathrm{X} = \frac{\mathrm{A} - \mathrm{B}}{\mathrm{A} + \mathrm{B}} \tag{2.5}$$

where X is the event position along the detector, and A and B are the amplitudes at each end of the detector. For the experimental work described in this thesis, ^{3}He PSDs are used. Further discussion on the principle of charge-division and its application to PSDs can be found in [23, 47–49].

2.3 Digital Pulse Processing

As introduced in Section 2.2.4, neutrons are indirectly detected through secondary radiation from neutron-nuclei interactions. For PC detectors, the energy deposited by the secondary radiation is proportional to the collected induced charge, and is delivered in the form of current pulses with varying amplitudes to a pulse processing system. Within the pulse processing system, the current pulse is first amplified through a *pre-amplifier*. The pre-amplifier is usually mounted as close to the detector as possible, so as to minimise electronic noise such as from the pickup of stray electromagnetic fields, and maximise the signal-to-noise ratio. Charge-sensitive pre-amplifier types are usually employed, which integrate the pulses to produce an output voltage proportional to total charge.

For this work, the analog output voltage signal is sampled by a digitiser, in which its basic function is to convert the features of analog signals to digital signals using an analog-to-digital converter (ADC). Computer software can then be used to process and analyse the digital signals to produce relevant results and histograms. Figure 2.4 illustrates a typical digital pulse processing chain. Detailed discussions of this chain is available in [50–53].

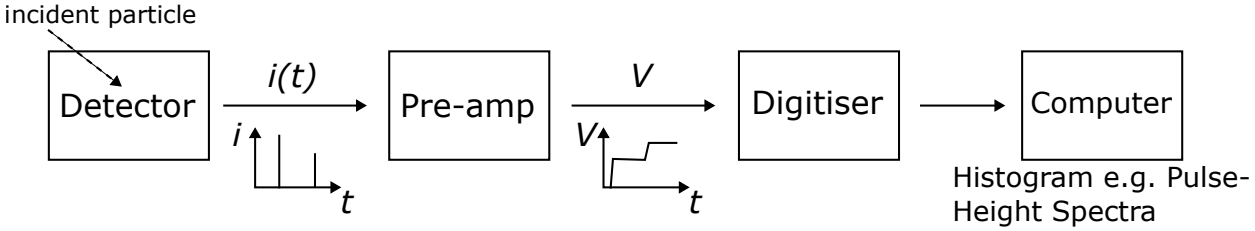

Figure 2.4: Block diagram of the processing of analog signals from a detector to digital signals in a computer.

3 Experiment

This chapter describes the experimental set-up at the LLB Saclay, France in September 2023. Firstly, the ^{3}He-triplet, and the three configurations that make up the detector system, are detailed. Next, the pulse processing chain is discussed, and finally the measurement procedure is described.

3.1 Experimental Set-up

Three position-sensitive ^{3}He PCs are electrically joined to form a ^{3}He-triplet, as shown in Figures 3.1 (a) and (b). All the ^{3}He-tubes are 12.7 ± 0.5 mm in diameter, and are filled with 10 bar of ^{3}He gas. Resistors are used to join the ^{3}He-tubes, such that each ^{3}He-triplet functions as one long single position-sensitive detector. As introduced in Section 2.2.5, position reconstruction of a neutron event is achieved using Amplitudes A and B, at the two ends of a ^{3}He-triplet. Each of the two ends of the ^{3}He-triplet is connected to a pre-amplifier which amplifies the two amplitudes. The ^{3}He-tubes are designated as tube 0, 1, and 2, with total length L.

The design of each ^{3}He-triplet includes sheets of Cd-sheets (0.5 mm thick) which are placed at the perimeter, and between and behind each tube, to minimise cross-talk and background noise. Similar to the cross-talk mentioned in Section 1.1.1, in the context of a ^{3}He-triplet, cross-talk refers to unwanted neutron transition between the individual ^{3}He-tubes. During the experiment, a Cd-mask (≈ 3.0 mm thick) with asymmetric slits (3.0 mm wide) covers the ^{3}He-triplet. These slits allow for the study of the position reconstruction performance by defining specific areas of illumination along the ^{3}He-triplet (see Figure 3.1 (a)). The slits are positioned asymmetrically to the centre of the ^{3}He-triplet so that the two read-out amplitudes may be identified in the position reconstruction spectra, which is discussed in Section 4.2. The isotropic Am/Be neutron source (unmoderated: nominal activity 50 GBq, i.e. 2.804×10^6 neutrons/s in 4π steradian) is contained in a box that moderates the produced fast neutrons to slow neutrons.

For the detector system of the BIFROST instrument, there are a total 45 ^{3}He-triplets, which are split up into three sets of 15 ^{3}He-triplets, named configurations A, B, and C. The configurations are presented in Figure 3.2. In each configuration, the 15 ^{3}He-triplets are further grouped into sets of three, called arcs, where each of the five arcs correlate to specific neutron energies (see Section 1.1.1). Additionally, each arc of ^{3}He-triplets is embedded into the borated polyethylene of each detector module. Finally, the pre-amplifiers of each ^{3}He-triplet are assigned a channel number between 0 to 14 (per configuration). The channel number corresponding to each ^{3}He-triplet, and the total (L) and active lengths of each individual ^{3}He-tube are listed in Table 3.1. The same naming convention and lengths of the ^{3}He-triplets apply for each configuration. The slit distances from the centre of each Cd-mask (aligned with the centre of each ^{3}He-triplet) are listed in Table 3.2. The values listed correspond to d_1 and d_2 of the Cd-mask seen in Figure 3.1 (a).

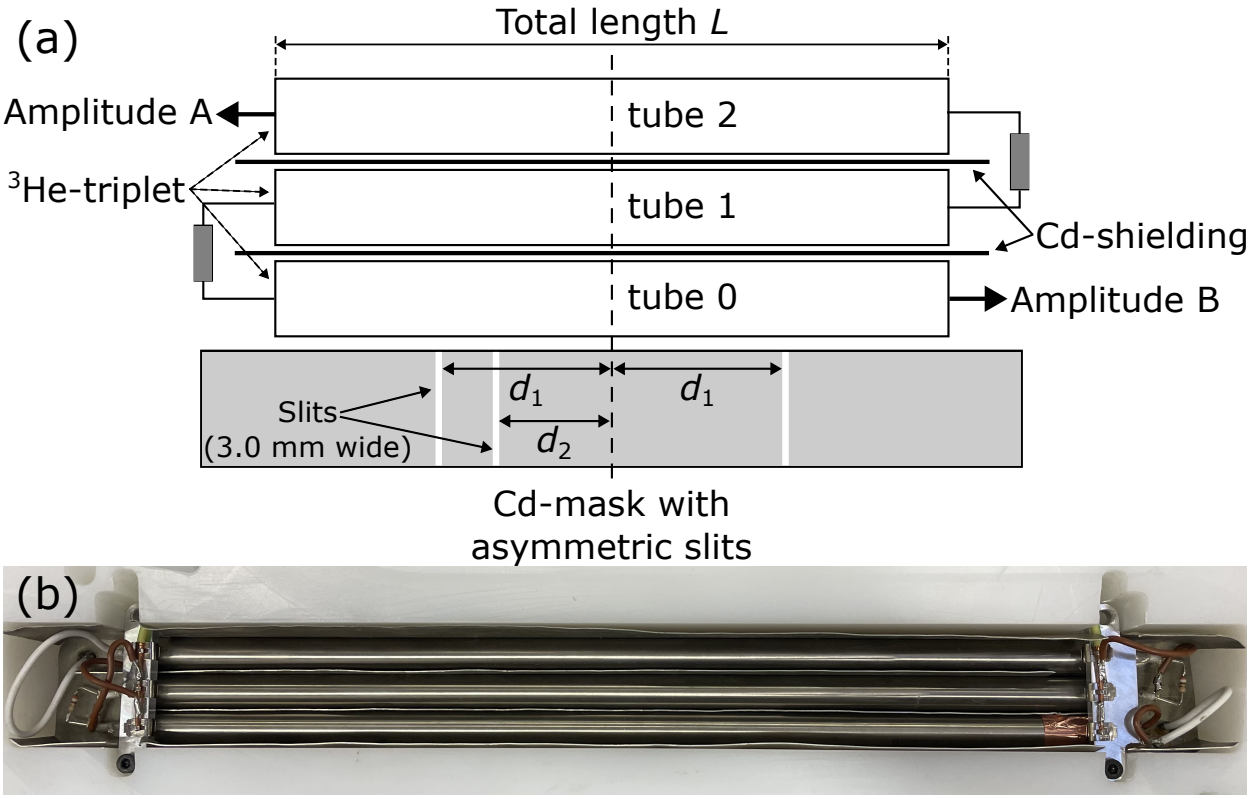

Figure 3.1: (a) Schematic diagram of a ^{3}He-triplet, electrically joined in a series with resistors between each tube. A Cd-mask is mounted in front of the ^{3}He-triplet when illuminated by the Am/Be neutron source. The asymmetric slits are positioned with distances d_1 and d_2, measured from the centre of the mask. (b) Photo of a ^{3}He-triplet embedded in a borated polyethylene of a detector module.

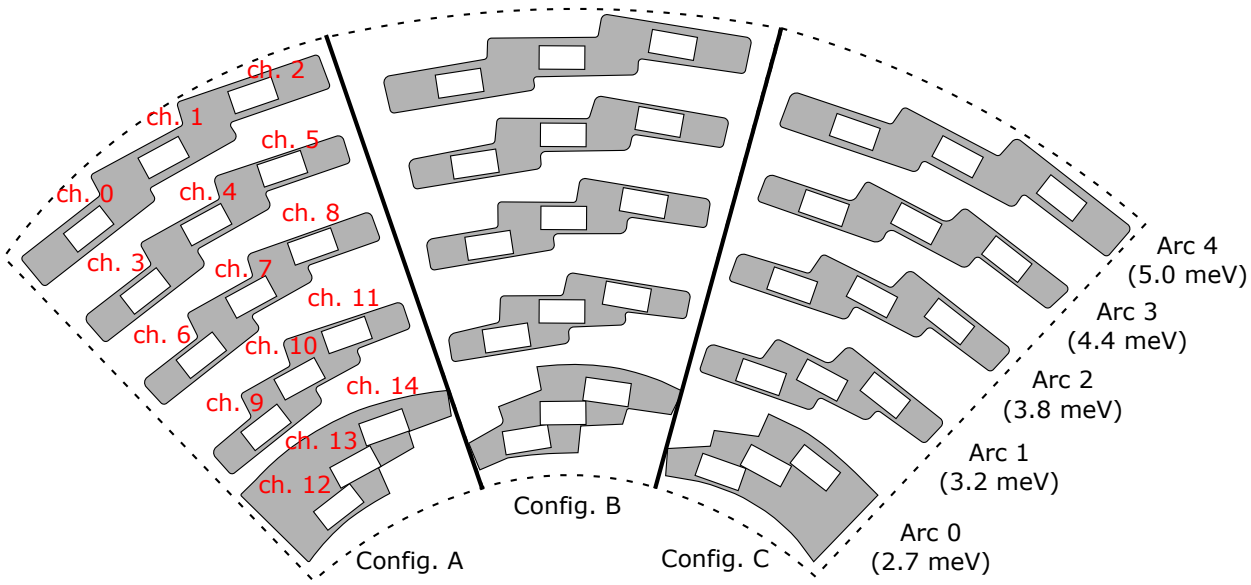

Figure 3.2: Schematic diagram of the 45 ^{3}He-triplets split into 3 configurations, named A, B, and C. Each borated polyethylene detector module (grey) contains three ^{3}He-triplets. In each configuration, the pre-amplifiers of each ^{3}He-triplet (white rectangles) are numbered from channel 0 to channel 14.

Table 3.1: Total (L) and active lengths of a ^{3}He-tube for all 15 ^{3}He-triplets, listed in its corresponding channel and arc number.

Channel #	**Arc # (E_n)**	**Active length [mm]**	**Total length (L) [mm]**
0	4 (5.0 meV)	312.0	353.0
1	4 (5.0 meV)	305.0	346.0
2	4 (5.0 meV)	299.0	341.0
3	3 (4.4 meV)	294.0	336.0
4	3 (4.4 meV)	287.0	329.0
5	3 (4.4 meV)	278.0	320.0
6	2 (3.8 meV)	275.0	317.0
7	2 (3.8 meV)	268.0	310.0
8	2 (3.8 meV)	261.0	303.0
9	1 (3.2 meV)	256.0	298.0
10	1 (3.2 meV)	249.0	291.0
11	1 (3.2 meV)	242.0	284.0
12	0 (2.7 meV)	234.0	276.0
13	0 (2.7 meV)	226.0	268.0
14	0 (2.7 meV)	218.0	260.0

Table 3.2: Position of the slits on the Cd-mask, as shown in Figure 3.1 (a). The distances are the same for each configuration.

Arc #	d_1 **[mm]**	d_2 **[mm]**
4	115	65
3	106	56
2	97	47
1	88	38
0	79	29

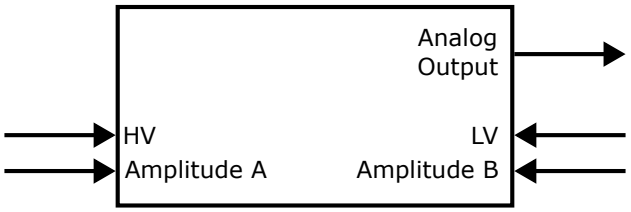

Figure 3.3: Schematic diagram of the input and output connections of the pre-amplifier box.

The measurement runs were performed with the Am/Be neutron source with Cd-masks mounted and facing the neutron source. The pre-amplifier boxes are custom-made by ILL, a schematic of which is shown in Figure 3.3. The HV input and two detector connections for Amplitudes A and B all use Safe High Voltage (SHV) type connectors. The low voltage (LV) powers the pre-amplifier circuits and use LEMO FFA 0S 303-type connectors. The analog output of the amplified signals of Amplitudes A and B are merged onto a single RJ45-type connector (Analog Output in Figure 3.3). Figures 3.4 (a) and (b) are photos of the experimental set-up taken from the point-of-view of the Am/Be neutron source, and show the five detector modules (making up one configuration) mounted on the configuration holder, with and without Cd-masks. Figure 3.4 (c) shows the back of the detector modules, where the pre-amplifiers are located.

A schematic diagram of the experimental set-up and pulse processing chain is shown in Figure 3.5. The analog output of the pre-amplifier is sent to a *signal collector*, which merges the analog output from two ^{3}He-triplets onto one RJ45 connector. Subsequently, the signals are then processed through a CAEN R5560 Open FPGA Digitiser [54] which contains four separate Field Programmable Gate Array (FPGA) modules. Finally, the digitiser outputs to a computer running the CAEN SciCompiler data acquisition software. In total, a detector configuration occupies 15 of the input signal collector ports, which after the signal collector fills all 8 RJ45-type ports of one FPGA module of the digitiser. Figure 3.4 (d) shows the electronics rack where the HV, LV modules, signal collector, and digitiser is mounted, with cables connected to the pre-amplifiers, and the computer.

The output of the pre-amplifiers are merged through the use of a standardised augmented category 6 (Cat6A) cable, which allows for up to four independent analog signals to be transported simultaneously with low noise and high bandwidth (up to 10 Gb/s), up to distances of 100 m [55]. As the Cat6A cables minimise the number of cables required to transport a large number of independent analog signals, the novel CAEN R5560 digitiser is designed to complement this by being able to process up to 128 analog signals simultaneously. Additionally, the relatively long distance that the cables are able to transport signals allows for the pulse processing system (excluding the pre-amplifiers) to be placed far away from the anticipated high neutron field environments (discussed in Section 1.2).

(a) Front of detector modules without Cd-masks.

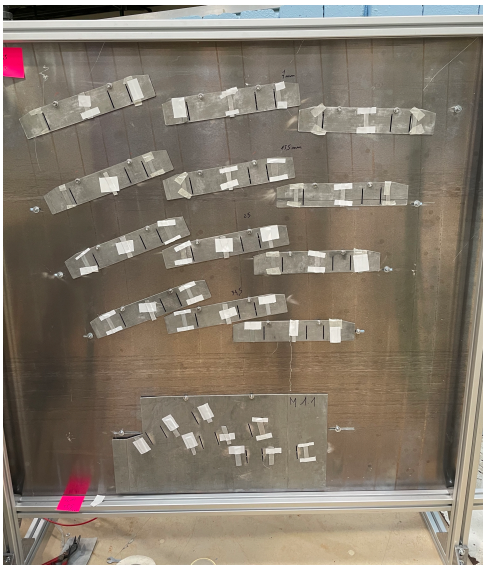

(b) Front of detector modules with Cd-masks.

(c) Pre-amplifiers fixed on the back of the detector modules, mounted on the configuration holder.

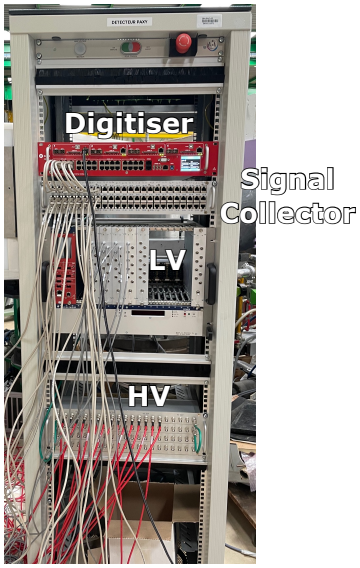

(d) Rack containing the HV, LV modules, signal collector, and digitiser.

Figure 3.4: Photos of the experimental set-up of a configuration mounted on the configuration holder, and cables connecting the electronics rack and pre-amplifiers.

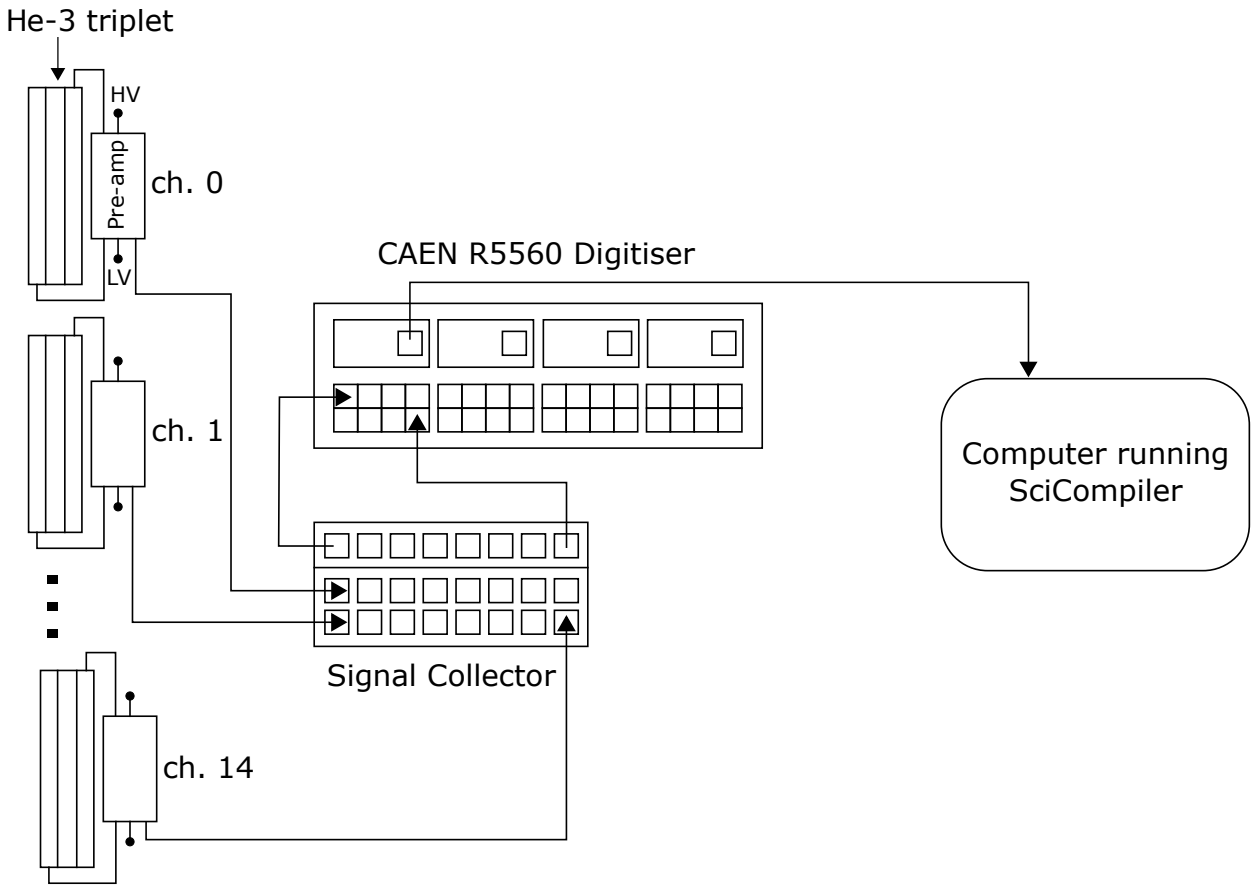

Figure 3.5: Schematic diagram of the experimental set-up and pulse processing chain. The analog output of the 15 pre-amplifiers is collected at and merged by the signal collector, and sent to the FPGA module. A computer running SciCompiler reads and stores the digital signals.

3.2 Measurement Procedure

In total, five measurements runs, two for each configuration A and C, and one for configuration B, were performed at various source-to-detector distances and heights of the Am/Be neutron source. The additional measurement run for configurations A and C was performed to ensure that all ^{3}He-triplets were illuminated. Details, and result analyses of all measurement runs is available in the appendices.

One measurement for each configuration was chosen and are further discussed in Chapter 4. The corresponding neutron source locations, and measurement times are as listed:

- Configuration A
  Source-to-detector distance: 140 cm, Height: 120 cm, Run-time: 3.33 hrs
- Configuration B
  Source-to-detector distance: 185 cm, Height: 120 cm, Run-time: 15.07 hrs
- Configuration C
  Source-to-detector distance: 175 cm, Height: 100 cm, Run-time: 24.04 hrs

Figures 3.6 (a) and (b) illustrate the experimental set-up. The neutron source location is different for each configuration, as marked by the corresponding coloured circles. The five detector modules are mounted upon the module holder. The source-to-detector distance is measured from the box containing the Am/Be neutron source to the front plane of the Cd-masks. The red dashed-line at height 120 cm signifies the centre of the detector module, channels 6, 7, and 8 (arc 2). Details of these additional measurements are found in Appendix A.

For all measurement runs, the HV supplied to the ^{3}He-triplets was 1400 V, with a LV supply of ± 6 V to the pre-amplifiers. According to the manufacturer (Baker-Hughes), the recommended HV range for operating the position-sensitive ^{3}He PCs in the proportional region is between 1000 to 1500 V [56]. An output voltage signal threshold (i.e. amplitude threshold) of ~ 100 mV for Amplitude A and B was applied in the data acquisition SciCompiler software.

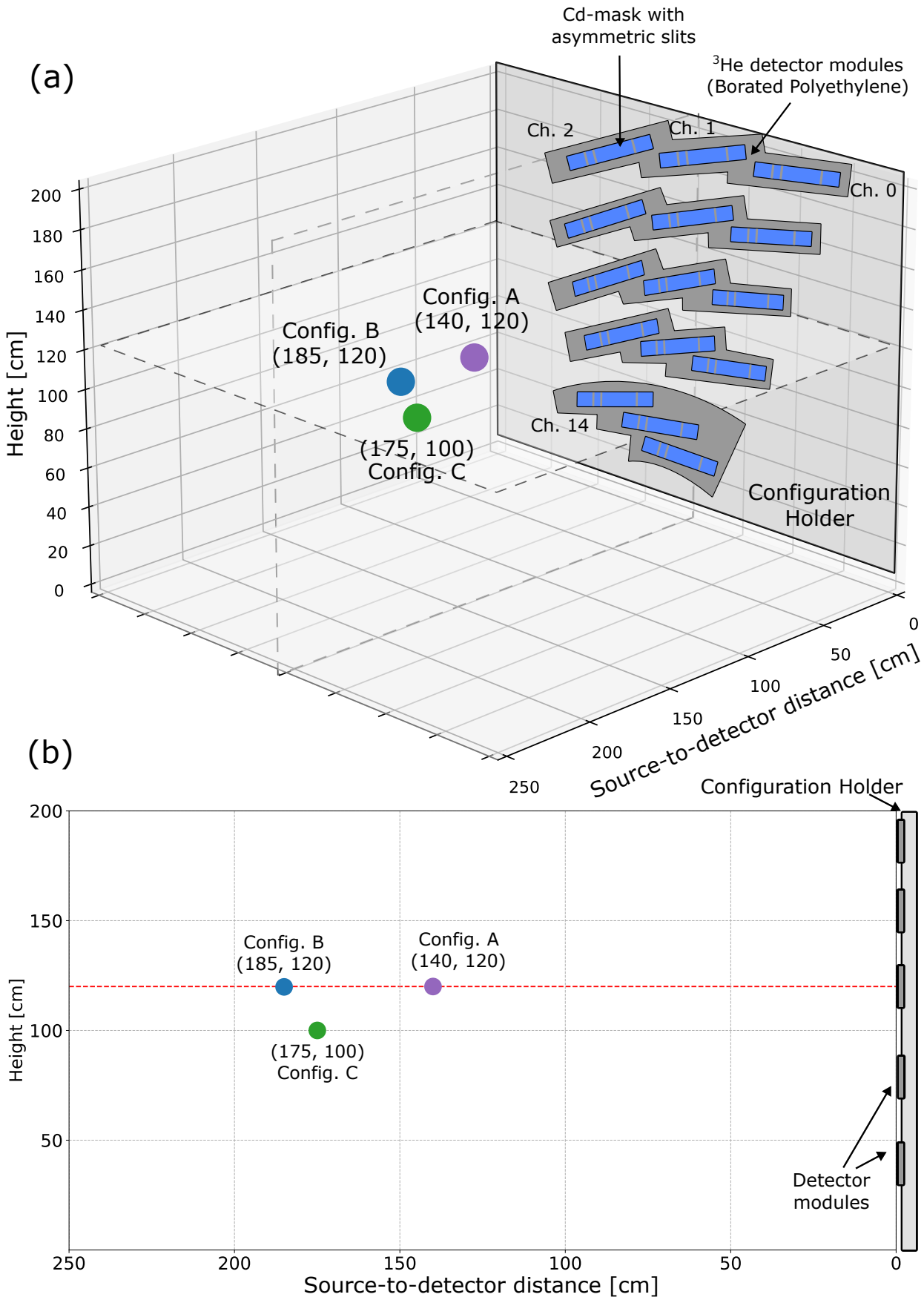

Figure 3.6: (a) Isometric view of the experimental set-up. (b) Side-view of the experimental set-up. The neutron source locations for the three configurations are marked with their source-to-detector distances and height positions. The red dashed-line represents arc 2 of the configuration.

4 Results and Discussion

This chapter presents the results obtained from the slow neutron measurements performed at LLB Saclay. The pulse-height spectra of selected ^{3}He-triplets are first discussed, followed by the position reconstruction spectra and subsequent fitting of the spectra. Lastly, the performance of the position reconstruction of the detector system is calculated and discussed.

All data analysis was performed using Python 3.11 [57], with packages Pandas 2.0.0 [58], Numpy 1.24.2 [59] and Scipy 1.10.1 [60].

4.1 Pulse-Height Spectra

The pulse-height spectra of channel 7 are shown for each configuration A, B, and C in Figures 4.1 - 4.3, and is made up of the sum of Amplitudes A and B. Channel 7 of each configuration is chosen as its ^{3}He-triplet has the most direct line-of-sight to the Am/Be neutron source (see Figure 3.6). The statistical uncertainty, $\sqrt{\text{counts}}$, is not shown as the uncertainty is too small to illustrate at each bin. The pulse-height spectra of all channels of each measurement run is shown in Appendix A.

All three pulse-height spectra show the applied amplitude threshold (see Section 3.2), resulting in no stored data points below bin channels of 3000, which corresponds to $\sim 100\,\text{mV}$. From the pulse-height spectrum of configuration B and C, the triton-, proton-, and full-energy peaks can be observed (as discussed in Section 2.2.4). These features are not as distinct in the pulse-height spectrum of configuration A, owing to the shorter measurement time. Comparing the experimental pulse-height spectra to the expected pulse-height spectrum presented in Figure 2.3 (b), a difference is that the noise contributions at low bin channels are filtered out due to the applied threshold. However, across all configurations, the continuous range of the double-plateau feature is not as apparent, due to the chosen HV supplied to the ^{3}He-triplets. As introduced in Section 2.2.4, the applied HV determines the proportionality property of the PC. At lower HV ($\sim 1100\,\text{V}$), the proportionality is preserved, and therefore the pulse-height spectrum would be as expected in Figure 2.3 (b). However, at higher HV ($\sim 1500\,\text{V}$), there is a slight loss in proportionality as the applied HV is close to the recommended upper limit by the manufacturer (see Section 3.2) for operation in the proportional region. The applied 1400 V therefore leads to a "compression" of the pulse-height spectra (see Figures 4.1 - 4.3). However, the benefit of operating the detectors at higher HV is greater gas multiplication, and therefore sharper current pulses. This makes it easier to differentiate between pulses of different amplitudes registered at Amplitudes A and B by the pre-amplifier, resulting in a more accurate position reconstruction [61]. For the purposes of the BIFROST instrument (see Section 1.1.1), the performance of position reconstruction of the ^{3}He-triplets is deemed more important.

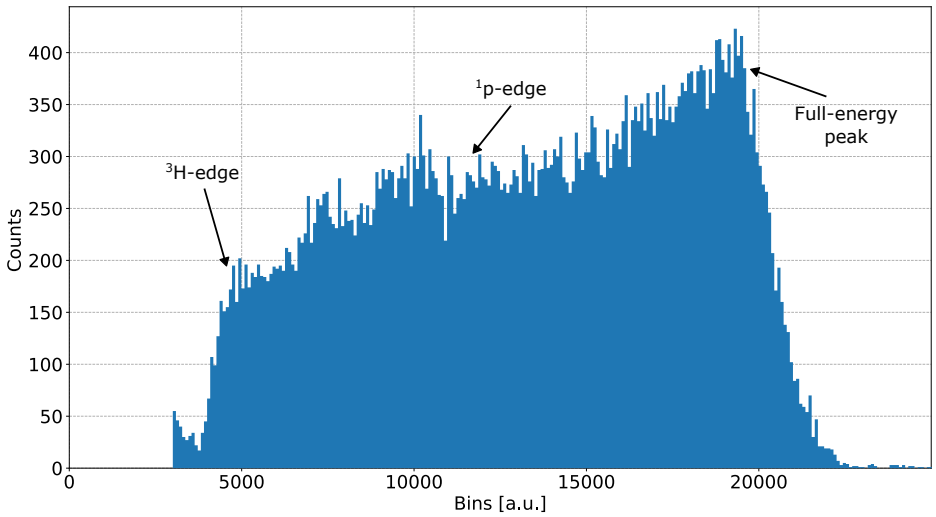

Figure 4.1: Pulse-height spectrum (Amplitude A+B) of channel 7 of configuration A.

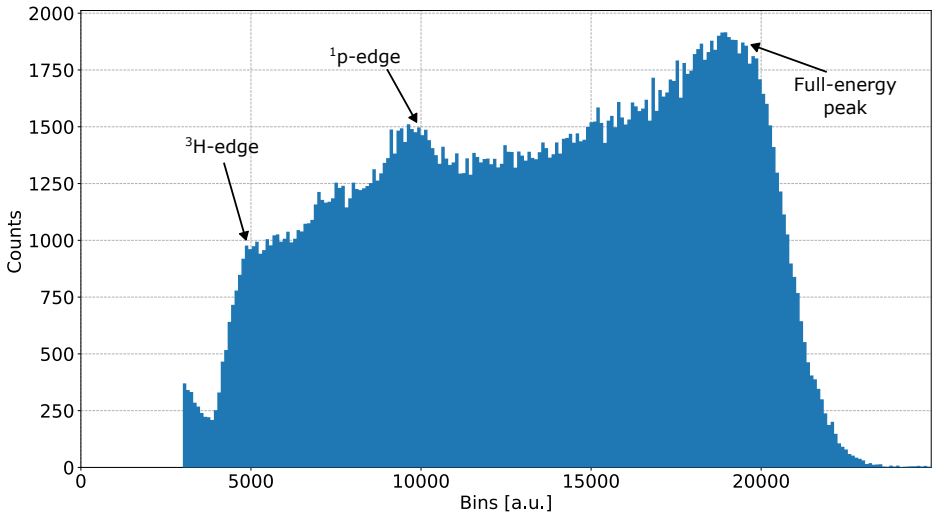

Figure 4.2: Pulse-height spectrum (Amplitude A+B) of channel 7 of configuration B.

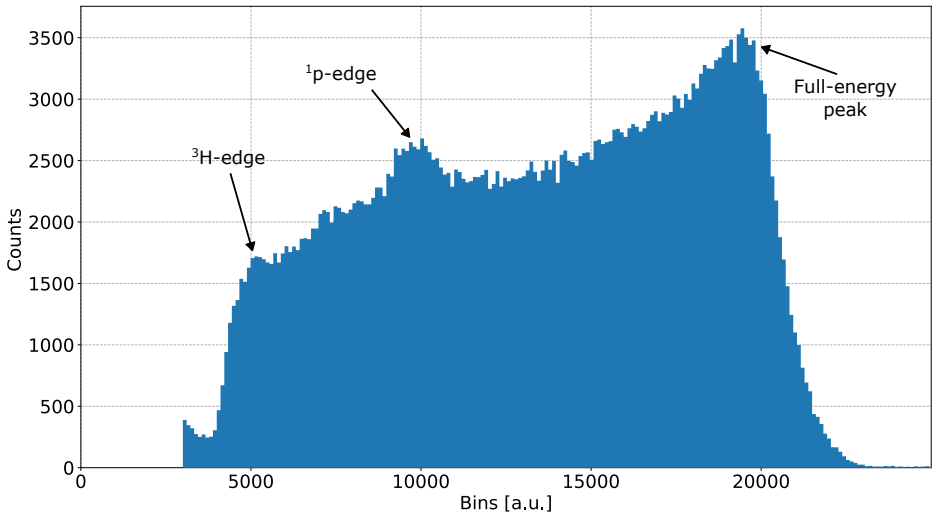

Figure 4.3: Pulse-height spectrum (Amplitude A+B) of channel 7 of configuration C.

4.2 Position Reconstruction Spectra

The position reconstruction spectra of the ^{3}He-triplets are created using Amplitudes A and B and the charge-division equation (Equation 2.5) introduced in Section 2.2.5. Figures 4.4 - 4.6 show the position spectra of all 15 channels of each configuration, respectively. The x-axis of the position spectra ranges from -1 to 1 due to the charge-division equation used, while the y-axis is the number of counts. Tube 0 is represented by the first third of the position spectra with a range of $[-1, -0.33]$, tube 1 is the second third with range $[-0.33, +0.33]$, and tube 2 is the final third with range $[+0.33, +1]$. The read-out end Amplitude B is at position -1, and the read-out end Amplitude A is at position $+1$ (see Figure 3.1 (a)). The separation between the tubes, where there are no significant counts, is created by both the non-active length of the ends of the ^{3}He-tubes, and the resistors electrically joining them together.

Beginning with the position spectrum of configuration A (Figure 4.4), there are a total of nine peaks visible in most channels. These correspond to the position of the slits of the Cd-mask, three for each ^{3}He-tube of a ^{3}He-triplet. The three peaks of tube 1 is mirrored in position as compared to tube 0 and tube 2. This is due to the design of the ^{3}He-triplet, where the three ^{3}He-tubes are electrically joined in a series (see Figure 3.1 (a)). Additionally, there are also no observable peaks that correspond to the slits of the Cd-mask in tube 2 of channels 12 and 13, possibly due to lower statistics owing to the relatively shorter measurement run-time.

Similar features as discussed for configuration A are observed in the position spectrum of configuration B (Figure 4.5). Finally, in the position spectrum of configuration C (Figure 4.6), no peaks can be observed in channels 12, 13, and 14, but their functionality was proven in a separate measurement run (discussed in Appendix A). For the other channels, similar features as discussed for configurations A and B are observed.

Common to all position spectra is the "background" on top of which the position peaks are located. As the applied threshold has filtered out most of the noise contributions (see Figures 4.1 - 4.3), contribution to the background is likely to be from neutron capture events. Although the fast neutrons emitted from the Am/Be neutron source is moderated, fast neutrons may still escape and scatter around the laboratory space, contributing to the background. The borated polyethylene of the detector module could also moderate and scatter the fast neutrons, contributing further to the background. A feature that can be observed in several position spectra of each configuration is the "flash" peak. Apparent examples of this feature are in channel 14 of configuration A (Figure 4.4) around bin position -0.9, channel 3 of configuration B (Figure 4.5) around bin position 0.9, and channel 9 of configuration C (Figure 4.6) around bin position -0.2. These flash peak features, which appear in different bin positions, and in different magnitudes, are not part of the expected position spectrum. Therefore, the flash peaks are unlikely to have originated from neutron capture events. The flash peak features observed in the position spectra of all three configurations can be attributed to several factors. Dust and moisture present on the ^{3}He-tubes and connecting wires may contribute to sparking during operation, which can be interpreted as the observed flash peaks. Additionally, contributions from grounding issues of the ^{3}He-triplets and the detector modules can also be a factor. These ^{3}He-triplets were returned to the lab after the factory acceptance test for further inspection by the detector technician at LLB.

Another feature observed is a consistent lower peak height of tube 2 (right most in the spectra) for all channels of each configuration. This could be due to geometric effects of the travelling incident free neutrons, where the components around the ^{3}He-triplets may cause

shadowing effects due to the position of the Am/Be neutron source. To better understand if the position of the neutron source indeed affects the reduced counts in tube 2, or due to some other factor, heat-maps consisting of the number of event counts in each ^{3}He-tube of each configuration are available in Appendix A. Likewise, in an effort to further understand the issue of the flash peaks, a study of the time-dependency of these flash peaks during a measurement run is available in Appendix B. Additionally, the position reconstruction spectra of the additional measurement runs are also available in Appendix B.

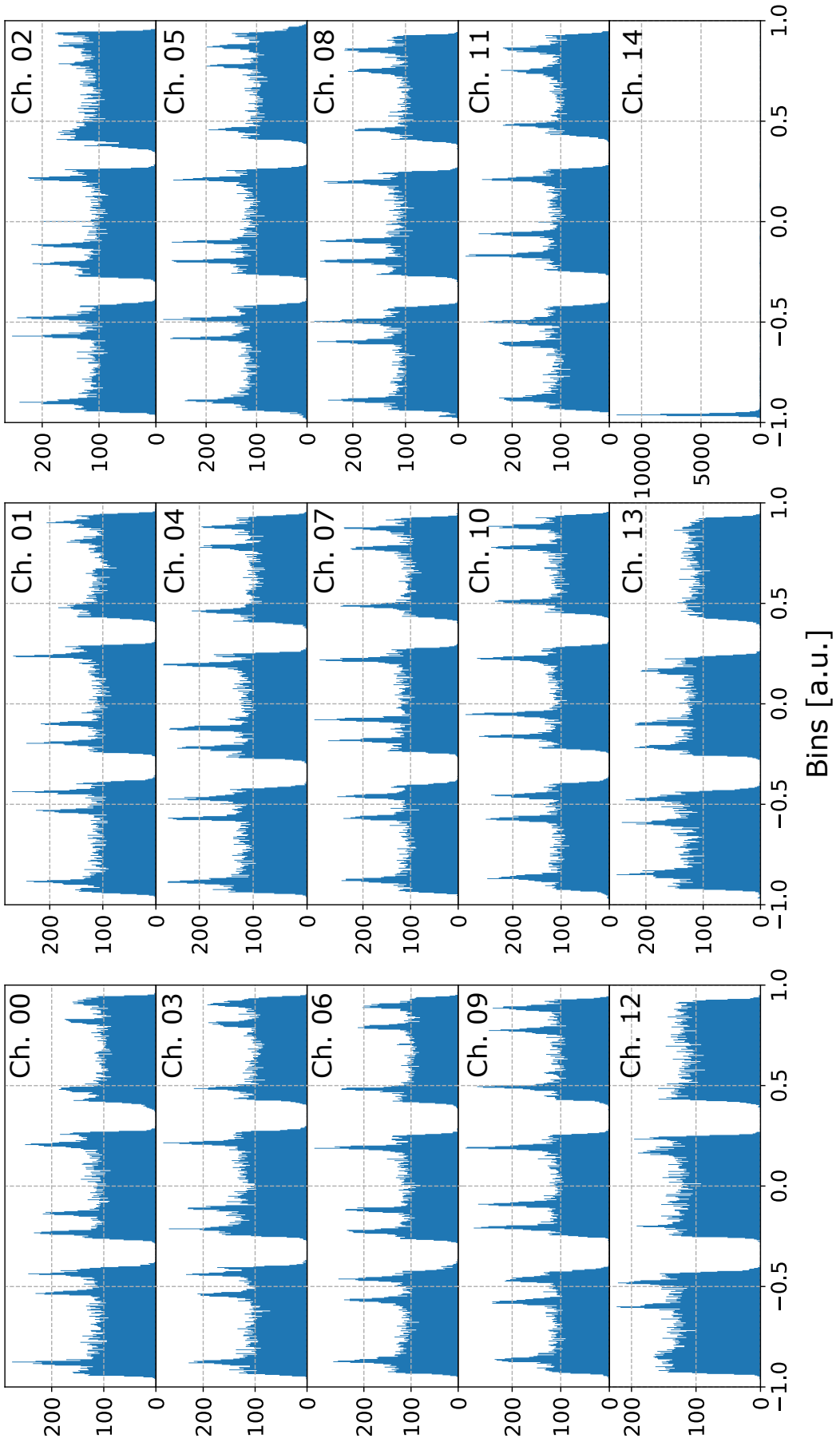

Figure 4.4: Position spectrum of configuration A of all 5 detector modules.

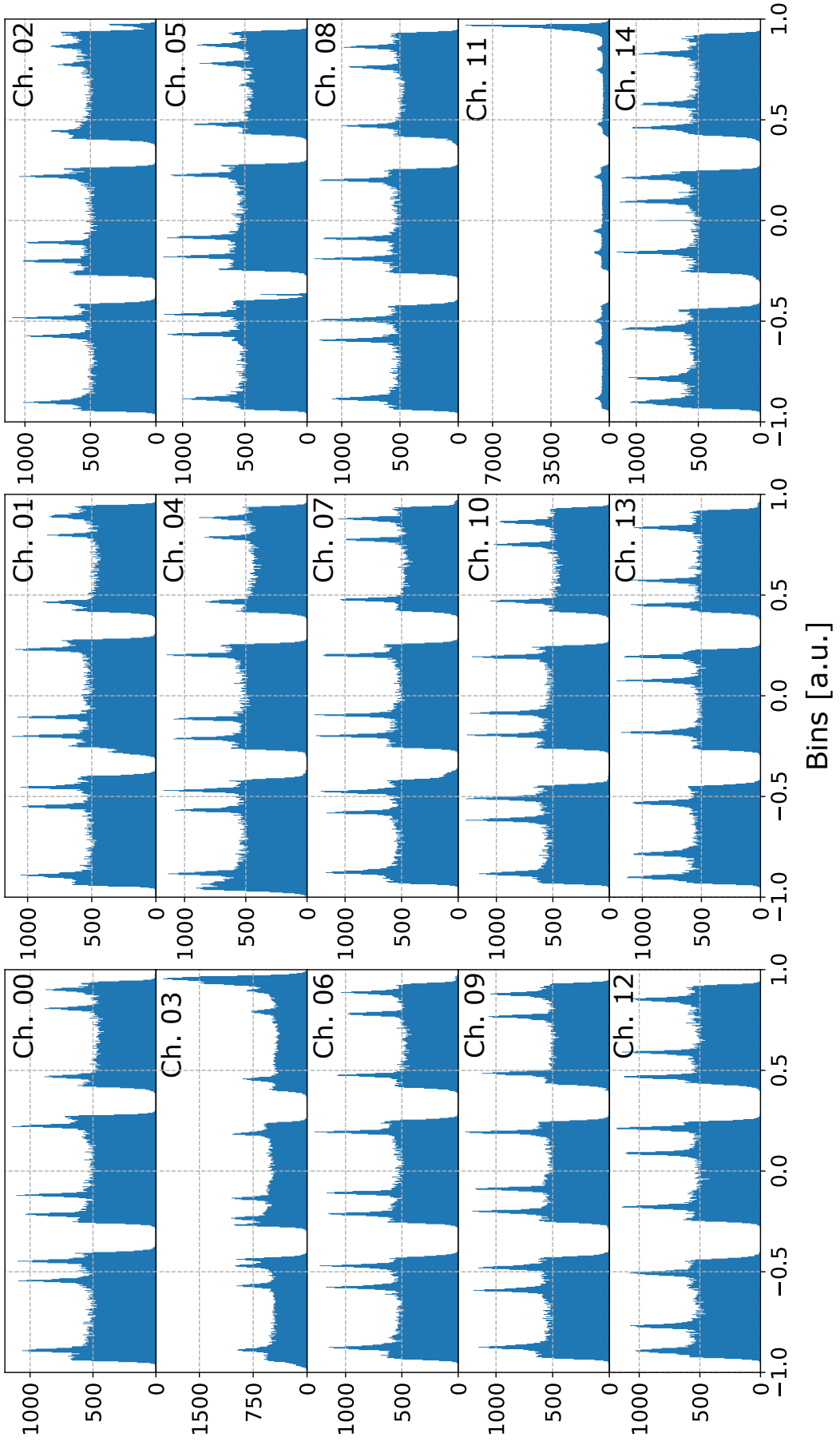

Figure 4.5: Position spectrum of configuration B of all 5 detector modules.

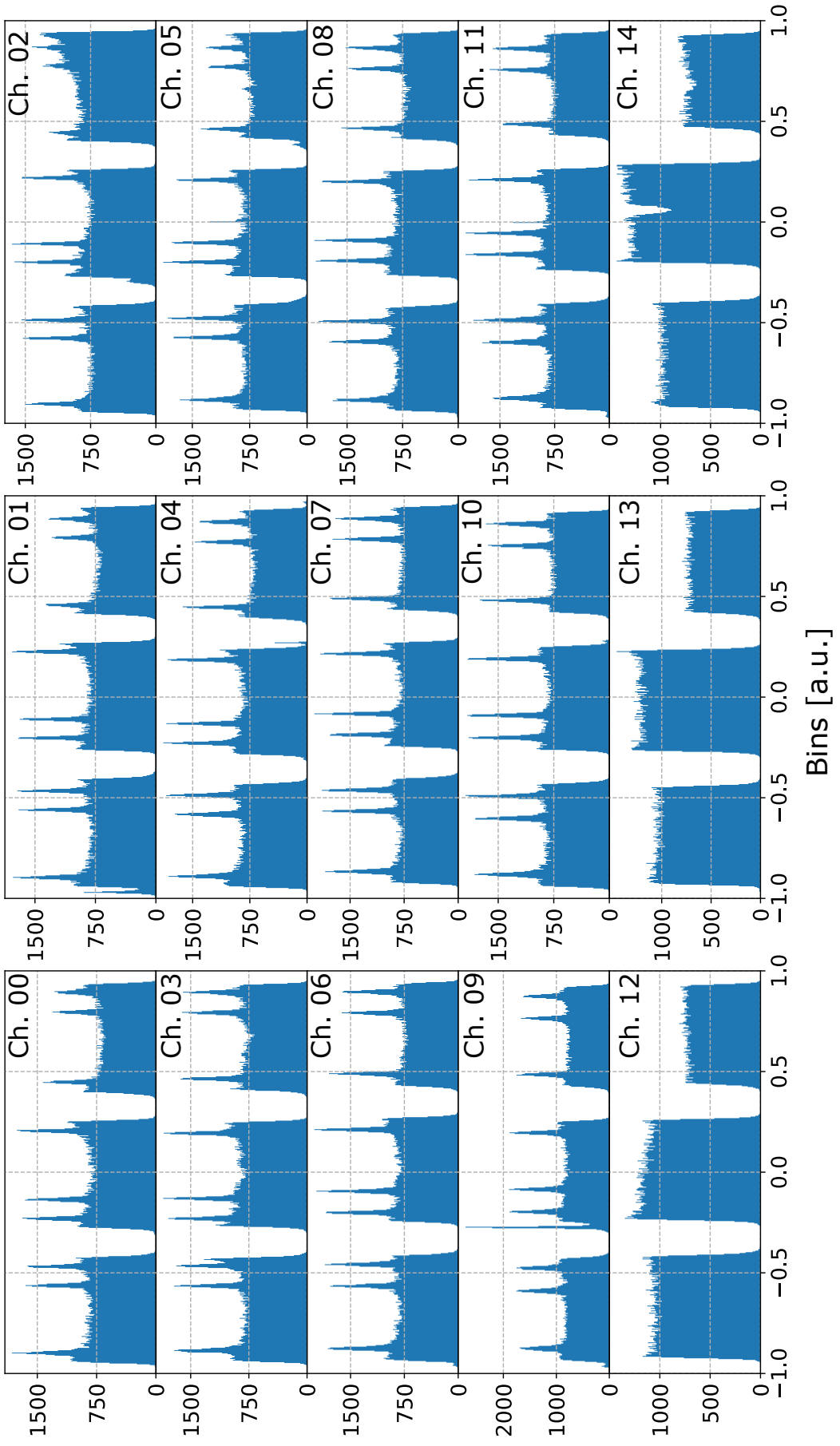

Figure 4.6: Position spectrum of configuration C of all 5 detector modules.

4.2.1 Fitting the Position Spectra

To fit the nine peaks of a position spectrum, a *superfunction* is employed for each *tube*, so that background subtraction is not required. The superfunction is defined as:

$$f(x) = \underbrace{ax^2 + bx + c}_{\text{2nd-order polynomial}} + \underbrace{A_0 \exp -\frac{(x-\mu_0)^2}{2\sigma_0^2}}_{\text{Gaussian peak 1}} + \underbrace{A_1 \exp -\frac{(x-\mu_1)^2}{2\sigma_1^2}}_{\text{Gaussian peak 2}} + \underbrace{A_2 \exp -\frac{(x-\mu_2)^2}{2\sigma_2^2}}_{\text{Gaussian peak 3}} \tag{4.1}$$

The function is a superposition of four sub-functions. The quadratic (2nd-order) polynomial has three variables a, b, and c, which forms the background. The subsequent three Gaussian functions fit the three peaks from the slits of the Cd-mask, with amplitude A_i, centroid μ_i, and standard deviation σ_i, where index i corresponds to each peak position. The boundaries of the function is chosen to be between the step-like function of each tube.

The position spectrum of a ^{3}He-triplet will have a total of nine peaks, three in each ^{3}He-tube. The nine peaks are first located, such that its position and amplitude values may be used as a starting point for fitting with Equation 4.1. The superfunction is then fitted to each tube, obtaining the centroid (μ) and standard deviation (σ) values of each peak.

As an example, Figure 4.7 displays the process of fitting the position spectrum for channel 7 of configuration B. Part (a) of the figure illustrates the first step of identifying the nine peaks across the three tubes, as well as the region of interest (ROI) that sets the boundaries of the fitting function of each tube. An unique ROI is chosen for each tube, of each channel, owing to the difference in total and active lengths of the ^{3}He-tubes (see Table 3.1). Part (b) of the figure illustrates the three separate fitted superfunctions overlaid upon the position spectrum.

The rest of this section discusses the fitting results of channel 7 of configurations A, B, and C. The code, written in Python, used to fit all the position spectra is available in Appendix B.

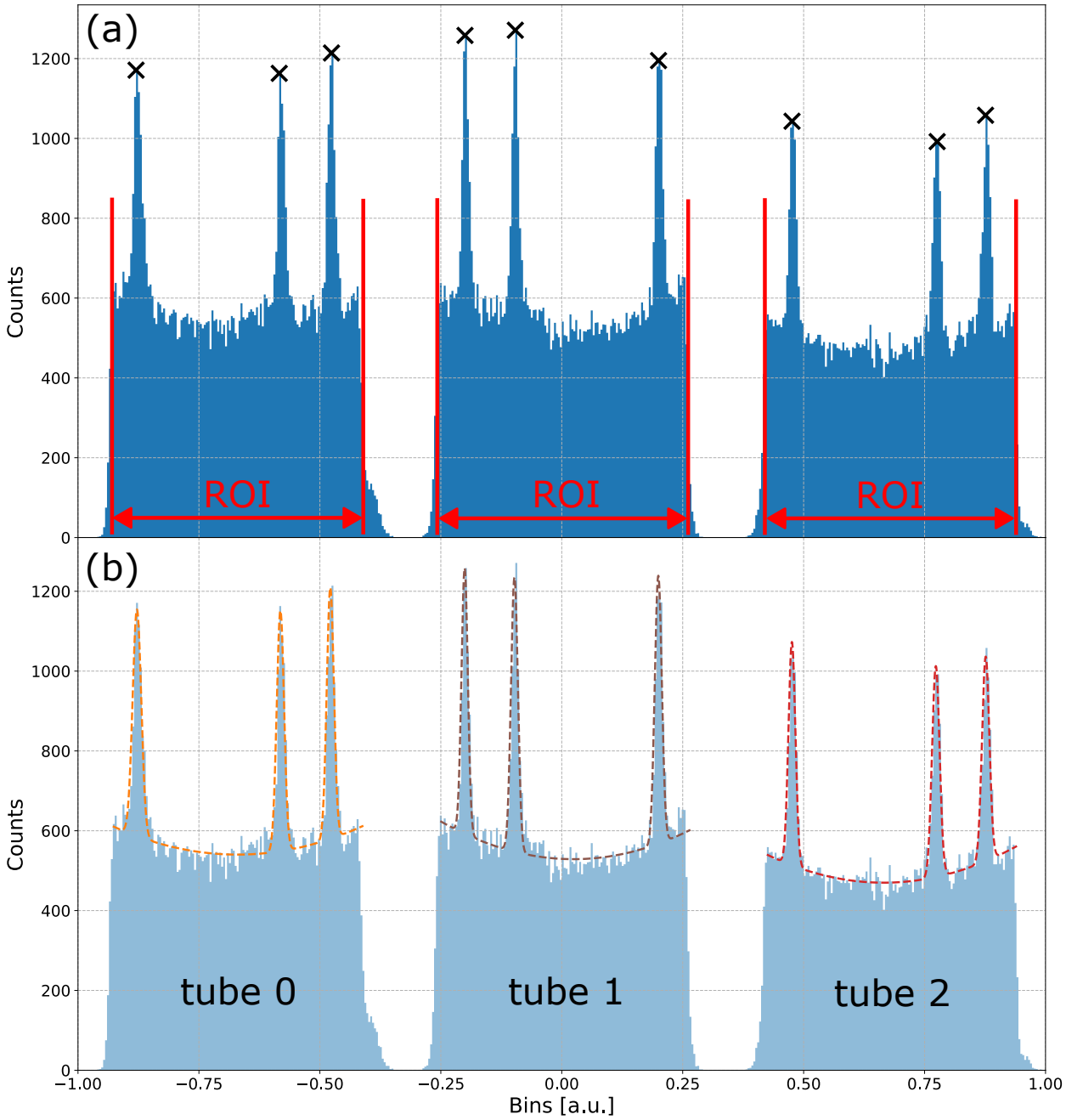

Figure 4.7: Peak identification and fit applied on position spectrum of channel 7 of configuration B. (a) Peak identification ("×") and ROI for the fitting function. (b) Fitting function overlaid upon the position spectra of each tube (dashed lines).

In order to evaluate the goodness-of-fit of the fitted superfunction, a reduced chi-squared (χ^2_ν) metric is utilised. The reduced chi-squared is defined as:

$$\chi^2_\nu = \frac{\chi^2}{\nu} \quad ; \text{ and } \quad \chi^2 = \sum_i^N \frac{(y_i - f_i)^2}{\sqrt{y_i}^2} \tag{4.2}$$

The value of ν is the number of data points (N) minus the number of fitted parameters. In general, $\chi^2_\nu \approx 1$ indicates a good fit. In the case of the superfunction (Eqn. 4.1), there is a total of 12 parameters. The chi-squared (χ^2) expression has the variables of data count y_i, fitted count f_i, and statistical uncertainty $\sqrt{y_i}$.

The reduced-chi squared values of the superfunction is tabulated in Table 4.1. The relatively large values indicate under-fitting of the superfunction, however, the data points used is the entire span of the ROIs. When using the data points around the Gaussian peaks to obtain the respective reduced-chi square values, tabulated in Table 4.2, the values are much closer to 1, indicating a relatively good fit. In each tube, the three Gaussian peaks are marked as i, ii, and iii, in order of increasing bin position.

Table 4.1: Reduced chi-squared values for the fitted results of Equation 4.1 on channel 7 for configurations A, B, and C.

	Tube 0	Tube 1	Tube 2
Configuration A	10.2	10.1	12.4
Configuration B	14.8	14.1	12.0
Configuration C	13.2	14.0	12.1

Table 4.2: Reduced chi-squared values for the fitted results of Equation 4.1 only on the Gaussian peaks of channel 7 for configurations A, B, and C. The reduced chi-squared value of each individual peak (i, ii, and iii) are shown.

	Tube 0			Tube 1			Tube 2		
Gaussian Peak	i	ii	iii	i	ii	iii	i	ii	iii
Configuration A	2.0	1.3	1.2	1.7	1.6	1.8	1.8	2.4	1.9
Configuration B	2.7	3.3	2.6	2.8	3.4	1.6	0.6	2.8	3.3
Configuration C	2.1	2.3	2.2	2.5	3.5	1.9	1.9	1.9	2.5

4.2.2 Capacitive Coupling Issue

The quadratic background of the position spectra is visualised with the fitted quadratic polynomial part of the superfunction, as observed in Figure 4.7 (b). An initial thought would be that some fast neutrons may escape from the Am/Be neutron source are moderated by the borated polyethylene of the detector module surrounding each of the ^{3}He-triplets. These moderated neutrons would most likely react with the edges of the ^{3}He-tubes, contributing to a quadratic background. A more probable reason, however, would be due to the characteristic RC-circuit from the design of a position-sensitive PC. The resistive anode wire and the cathode cylindrical surface form a continuous RC-circuit, such that a current pulse travelling to the read-out ends is affected. The resistance of the anode wire dampens the amplitude

of the current pulse, while the RC-circuit delays and broadens the current pulse [62, 63]. For the case of the ^{3}He-triplets, the capacitive coupling issue may be reduced by selecting different values for the resistors joining the tubes.

In order for a current pulse to be counted as a neutron event in a ^{3}He-triplet, both read-out ends should register the same current pulse-shape. For a neutron event in the middle of a ^{3}He-triplet, i.e. the middle point of tube 1, the current pulse reaches both read-out ends at the same time. On the other hand, for a neutron event close to read-out end A, the current pulse recorded at each end would be different in pulse-shape. The current pulse that reaches read-out end A would be sharp, while the current pulse that reaches read-out end B would be shaped and delayed. The difference in current pulse-shape at each read-out therefore shifts the position reconstruction closer towards read-out end A than expected. As a result, current pulses created close to either read-out end would not be differentiable by the digitiser, and therefore be placed in the same bin position. This leads to a non-linear response of the digital pulse processing chain, resulting in the quadratic background observed in the position spectra (see Figure 4.7).

4.3 Performance of Position Reconstruction

4.3.1 Position Calibration

Having obtained the centroid values and validated the goodness-of-fit of the Gaussian peaks of the superfunction, the bin positions of the position spectra can now be calibrated to physical lengths of the respective ^{3}He-tubes.

First, an origin point is established at read-out end Amplitude B, corresponding to bin position -1 of the position spectra. An ^{3}He-triplet is "unpacked", as illustrated in Figure 4.8, such that using the total length, L, of a ^{3}He-tube (Table 3.1), the range of the bin position $[-1, 1]$ is assumed to be the physical range of three ^{3}He-tubes $[0, 3\mathrm{L}]$.

As the slit positions of the Cd-mask is defined from the centre of a ^{3}He-tube (Table 3.2), a conversion step is needed to define the respective positions from origin. The centroid (μ_i) values obtained from the fitted superfunction (Equation 4.1) and converted slit positions of each Gaussian peak of each tube for channel 7 are tabulated in Tables 4.3 - 4.5, for configurations A, B, and C. The Gaussian peak positions of each tube in marked i, ii, and iii, in order of increasing position.

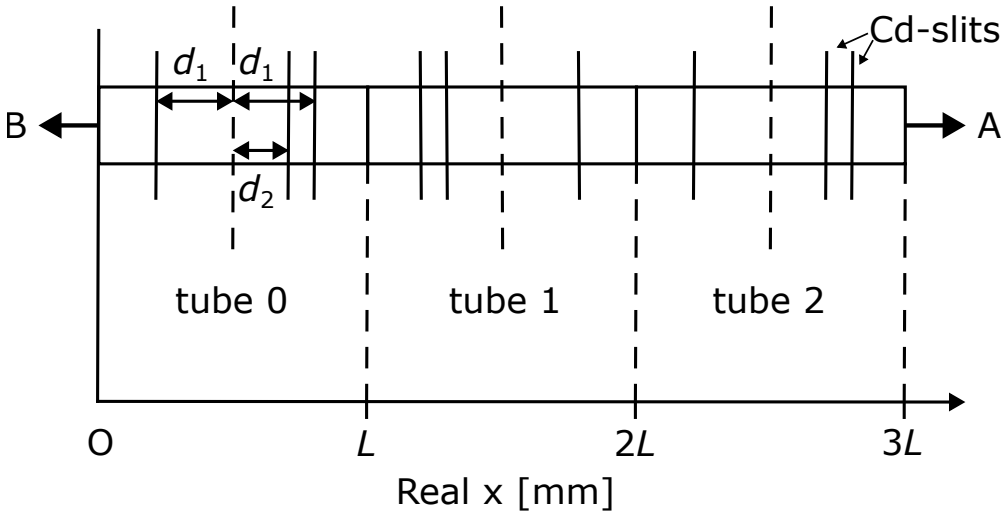

Figure 4.8: Schematic diagram of an unpacked ^{3}He-triplet. The origin is at read-out end B, extending to read-out end A with real length of $3L$. L is given by the total length of the tube. The solid, vertical lines across the tubes denote the slit positions of the Cd-mask.

These converted slit positions are then compared with the fitted centroid values of the nine Gaussian peaks, and is related with a linear calibration function defined as:

$$y = kx + m, \tag{4.3}$$

where y is the slit positions, x is the fitted centroid (μ) of the Gaussian peaks, k is the slope of the straight line, and m is the y-intercept. Utilising this linear calibration function, the bin channels of the position spectra are linearly calibrated, converting the bin channels to a defined physical range.

Table 4.3: Centroid (μ) from the superfunction and converted slit position values of each Gaussian peak of each tube for channel 7 of configuration A.

Configuration A - Channel 7			
Gaussian Peak	i	ii	iii
Tube 0			
μ [a.u.]	$-0.88 \pm (5.5 \times 10^{-4})$	$-0.57 \pm (5.5 \times 10^{-4})$	$-0.46 \pm (5.0 \times 10^{-4})$
Slit position [mm]	58	202	252
Tube 1			
μ [a.u.]	$-0.18 \pm (4.7 \times 10^{-4})$	$-0.08 \pm (3.9 \times 10^{-4})$	$0.22 \pm (4.4 \times 10^{-4})$
Slit position [mm]	368	418	562
Tube 2			
μ [a.u.]	$0.49 \pm (5.5 \times 10^{-4})$	$0.77 \pm (6.0 \times 10^{-4})$	$0.87 \pm (5.9 \times 10^{-4})$
Slit position [mm]	678	822	872

Table 4.4: Centroid (μ) from the superfunction and converted slit position values of each Gaussian peak of each tube for channel 7 of configuration B.

Configuration B - Channel 7			
Gaussian Peak	i	ii	iii
Tube 0			
μ [a.u.]	$-0.88 \pm (3.6 \times 10^{-4})$	$-0.58 \pm (3.1 \times 10^{-4})$	$-0.48 \pm (2.9 \times 10^{-4})$
Slit position [mm]	58	202	252
Tube 1			
μ [a.u.]	$-0.20 \pm (2.4 \times 10^{-4})$	$-0.10 \pm (2.4 \times 10^{-4})$	$0.20 \pm (2.5 \times 10^{-4})$
Slit position [mm]	368	418	562
Tube 2			
μ [a.u.]	$0.48 \pm (2.6 \times 10^{-4})$	$0.77 \pm (2.9 \times 10^{-4})$	$0.88 \pm (2.9 \times 10^{-4})$
Slit position [mm]	678	822	872

Table 4.5: Centroid (μ) from the superfunction and converted slit position values of each Gaussian peak of each tube for channel 7 of configuration C.

Configuration C - Channel 7			
Gaussian Peak	i	ii	iii
Tube 0			
μ [a.u.]	$-0.87 \pm (2.3 \times 10^{-4})$	$-0.57 \pm (2.0 \times 10^{-4})$	$-0.46 \pm (2.0 \times 10^{-4})$
Slit position [mm]	58	202	252
Tube 1			
μ [a.u.]	$-0.19 \pm (2.2 \times 10^{-4})$	$-0.09 \pm (1.9 \times 10^{-4})$	$0.21 \pm (1.9 \times 10^{-4})$
Slit position [mm]	368	418	562
Tube 2			
μ [a.u.]	$0.49 \pm (1.9 \times 10^{-4})$	$0.78 \pm (2.0 \times 10^{-4})$	$0.88 \pm (2.2 \times 10^{-4})$
Slit position [mm]	678	822	872

Additionally, the goodness-of-fit of the linear calibration function is evaluated using the coefficient of determination, R^2. The R^2 equation is:

$$R^2 = 1 - \frac{\sum_i^N (y_i - f_i)^2}{\sum_i^N (y_i - \bar{y})^2}, \tag{4.4}$$

where y_i is the slit positions, f_i is the fitted centroid values, and $\bar{y}$ is the mean of the nine slit positions. The closer the R^2 value is to 1, the better the goodness-of-fit.

The linear calibration variables, k and m, and the evaluated R^2 value for channel 7 of configurations A, B, and C is tabulated in Table 4.6. The percentage uncertainty for variable k is 0.8% for configuration A, and 0.6% for configurations B and C. All three linear-fits had a R^2 value of 0.99, indicating a good fit and reliable linear calibration variables.

As an example, Figure 4.9 shows the linear calibration for channel 7 of configuration B. The fitted centroid (μ) from the superfunction and converted slit position values from Table 4.4 are used in the linear calibration function (Equation 4.3).

Table 4.6: Linear calibration variables and R^2 value for channel 7 of configurations A, B, and C.

	Configuration A	Configuration B	Configuration C
k [mm]	462.9 ± 3.7	460.2 ± 2.9	461.0 ± 2.8
m [mm]	461.4 ± 2.1	465.7 ± 1.7	461.4 ± 1.6
R^2	0.99	0.99	0.99

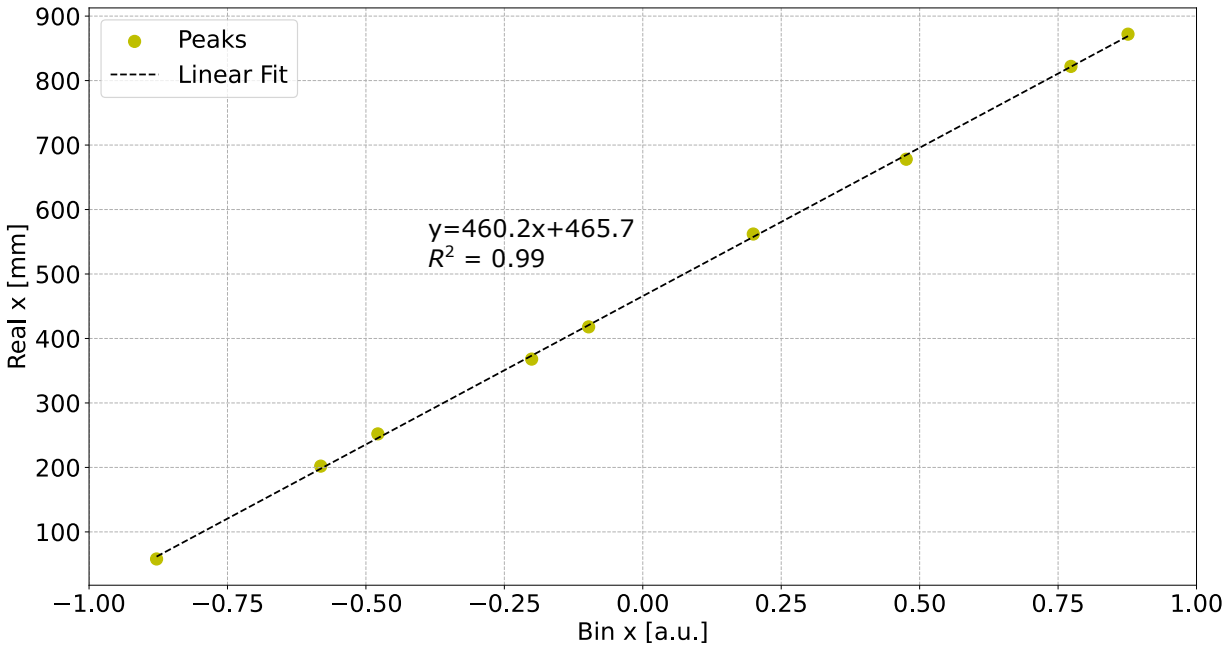

Figure 4.9: Linear calibration of channel 7 for configuration B. Yellow points denote the Gaussian peak points in bin and real position. The linear-fit is denoted by the dashed line, with linear calibration and R^2 value.

4.3.2 Position Resolution

The linear calibration, unique to each channel of each configuration, is then applied to their respective position spectra, converting the bin range $[-1, 1]$ to the physical range of $[0, 3L]$. The fitted variables of the quadratic polynomial of the superfunction (Equation 4.1) are then used to perform background-subtraction upon a position spectrum for visualisation purposes.

The full width at half maximum (FWHM) is related to the standard deviation with the following equation,

$$\text{FWHM} = 2\sqrt{2\ln 2} \cdot \sigma \tag{4.5}$$

From the fitting of the superfunction, the standard deviation (σ) of each Gaussian peak is converted to FWHM_f. By scaling up FWHM_f with the variable k of the linear calibration function (Equation 4.3 and Table 4.6), the reconstructed width, FWHM_k, illuminated by the incident free neutrons on each ^{3}He-tube is obtained. Note that this is not the real physical width of the illuminated area on the ^{3}He-tube, but is rather the width limited by the performance of the position reconstruction of the digital pulse processing chain.

The intrinsic ^{3}He-triplet spatial resolution of the detector system can now be derived. To determine the intrinsic spatial resolution of the chosen ^{3}He-triplet (channel 7) of each configuration, the physical illuminated width X upon each tube needs to be known. Figure 4.10 illustrates the top-down view of the experimental set-up, where the Am/Be neutron source illuminates a ^{3}He-triplet. Although the slit width of the Cd-mask is 3.0 mm, the actual illuminated width X would be slightly larger. The thickness t is defined as the thickness between the Cd-mask to the ^{3}He-triplet. In this experiment, the thickness of the module holder is 8.0 mm, the depth of the detector module is measured to be 23.2 mm, and the Cd-mask is estimated to be 3.0 mm, giving a total of $t = 34.2$ mm. Together with the source-to-detector distances of each configuration measurement run (see Section 3.2), the illuminated width X is calculated to be 3.1 ± 0.1 mm for all configurations.

The position reconstruction resolution FWHM_k is related to the intrinsic spatial resolution FWHM_d of the detector system and the FWHM_s of the illuminated width X, and therefore the intrinsic FWHM_d can be expressed as:

$$\begin{aligned} \text{FWHM}_k^2 &= \text{FWHM}_d^2 + \text{FWHM}_s^2 \\ \implies \text{FWHM}_d &= \sqrt{\text{FWHM}_k^2 - \text{FWHM}_s^2} \end{aligned} \tag{4.6}$$

The intrinsic spatial resolution of the detector system describes the limit in which it is able to differentiate the position between two neutron events, and is therefore independent to the slit width, or the reconstructed width. The FWHM_s is taken to be the illuminated width X, and the evaluated values of reconstructed FWHM_k and intrinsic FWHM_d is tabulated in Tables 4.7 - 4.9. In each table, the lowest value of reconstructed FWHM_k and intrinsic FWHM_d is highlighted in bold.

Figures 4.11 - 4.13 show the background-subtracted position spectrum of channel 7 of Configuration A, B, and C, respectively. In each, the nine Gaussian peaks are labelled with the associated reconstructed FWHM_k value. A lower reconstructed FWHM_k implies a better position reconstruction resolution, which also leads to a lower intrinsic FWHM_d, resulting in a better intrinsic spatial resolution (FWHM_d) of the detector system. Between the three configurations, the best position reconstruction resolution and intrinsic spatial resolution attained is in tube 1, Gaussian peak i of configuration B, where reconstruction

$\text{FWHM}_k = 7.1 \pm 0.3$ mm and intrinsic $\text{FWHM}_d = 6.4 \pm 0.3$ mm. As a comparison, the expected position reconstruction resolution (discussed in Section 1.1.1) is $\sim 1\%$ of the total length of an unpacked ^{3}He-triplet ($3L$), or 9.3 mm for channel 7, and almost all of the reconstructed FWHM_k values presented in Tables 4.7 - 4.9 are under, or around the expected value. In general, the position reconstruction resolution obtained in this work is within the range of, and in agreement to other works [64, 65]. A compilation of the evaluated FWHM_k and FWHM_d for other channels and measurement runs is available in Appendix C.

In all three configurations, the value of FWHM_k is observed to be lower in tube 1, with widths around $7 - 8$ mm, than compared to that of tube 0 or tube 2. The cause of this trend could be due to the location of tube 1 in the detector module between tube 0 and tube 2, where it is more shielded from neutrons scattered from the detector module, module holder, or the Cd-mask. Another factor, as discussed in Section 4.2.2, could stem from the reliability of position reconstruction being the best in the centre of tube 1, but decreases towards the read-out ends at tube 0 and tube 2, due to the capacitive coupling effect.

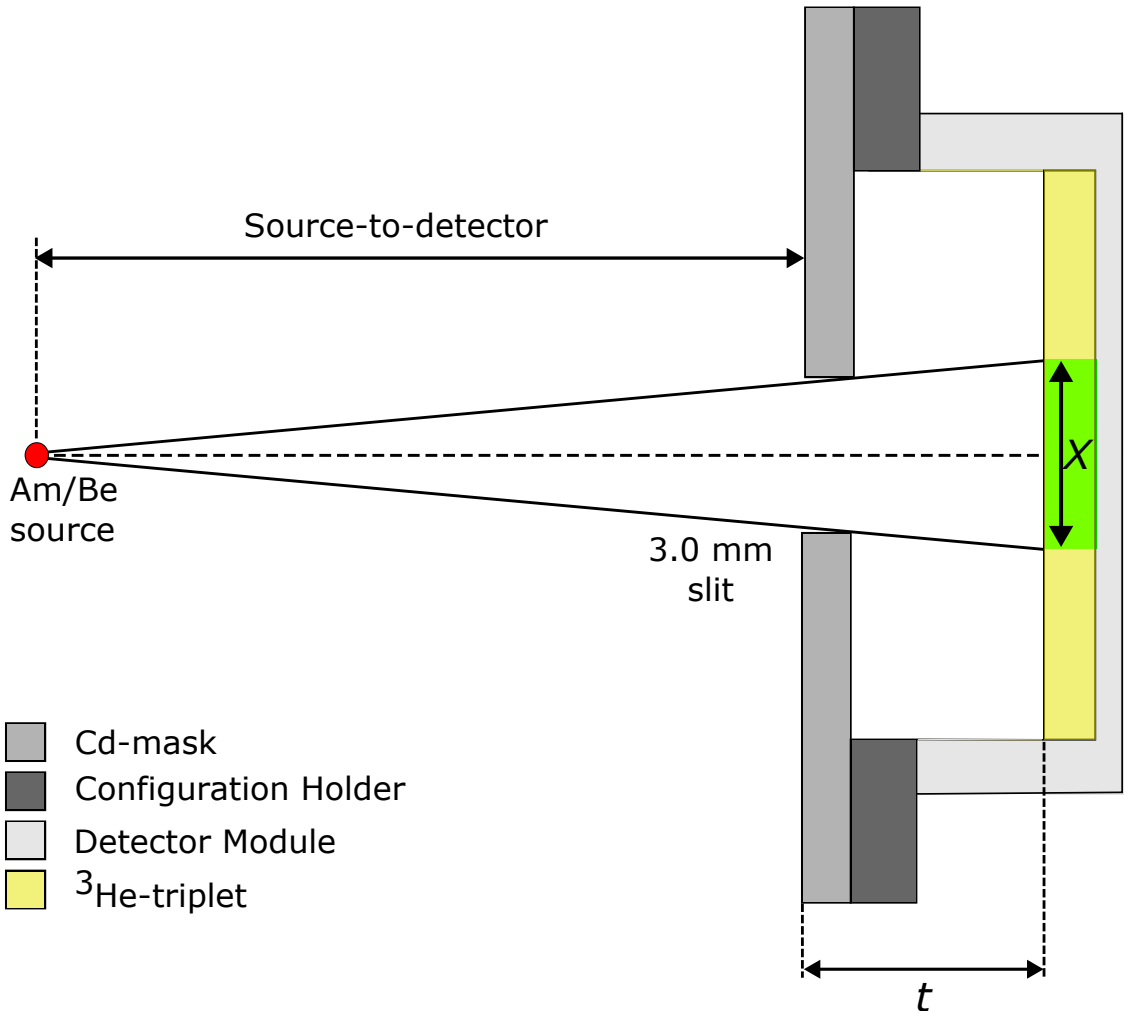

Figure 4.10: Top-down view of the experimental set-up. The different contributions to the thickness t together with the source-to-detector distance, gives the actual illuminated width X.

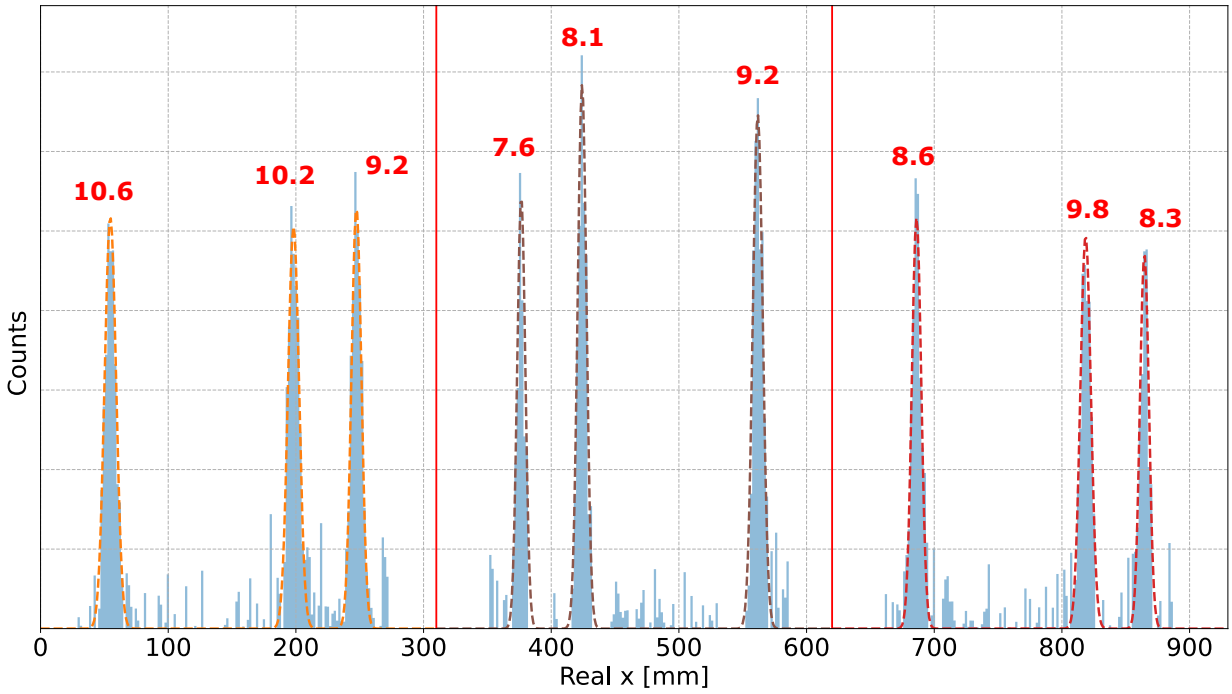

Figure 4.11: Real background-subtracted position spectrum of channel 7 of configuration A. The red horizontal lines denote the separation of each ^{3}He-tube. The reconstructed FWHM_k of each Gaussian peak is denoted by the red texts, in units of mm.

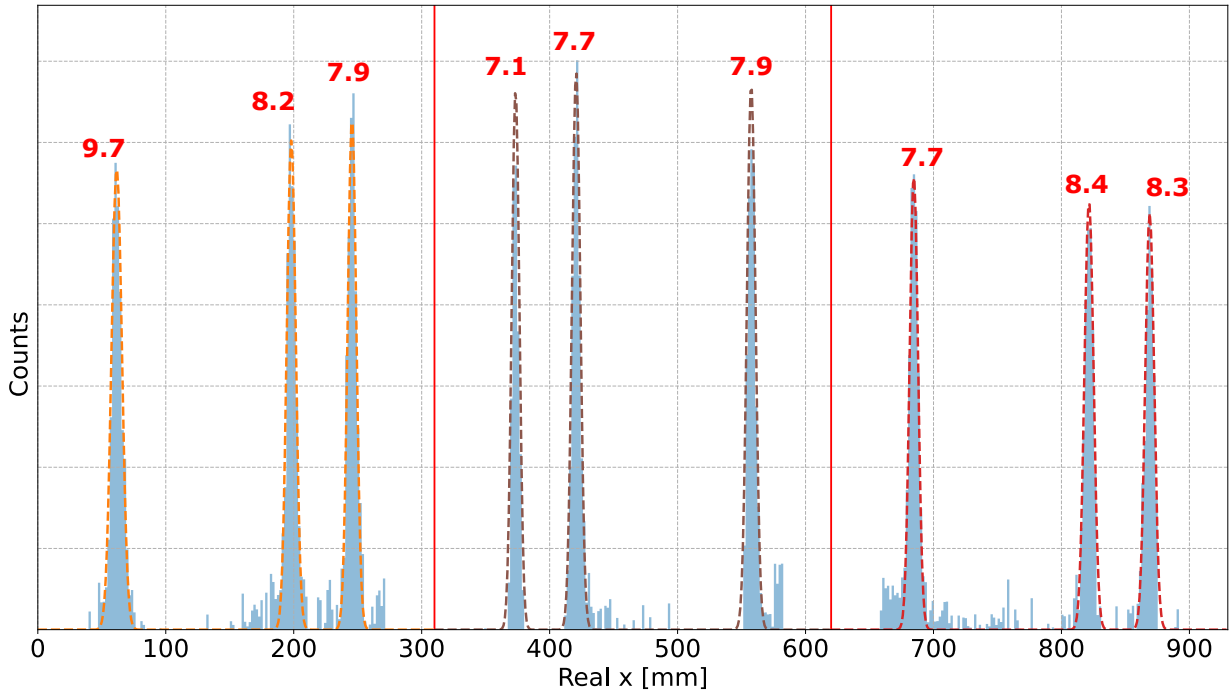

Figure 4.12: Real background-subtracted position spectrum of channel 7 of configuration B. The red horizontal lines denote the separation of each ^{3}He-tube. The reconstructed FWHM_k of each Gaussian peak is denoted by the red texts, in units of mm.

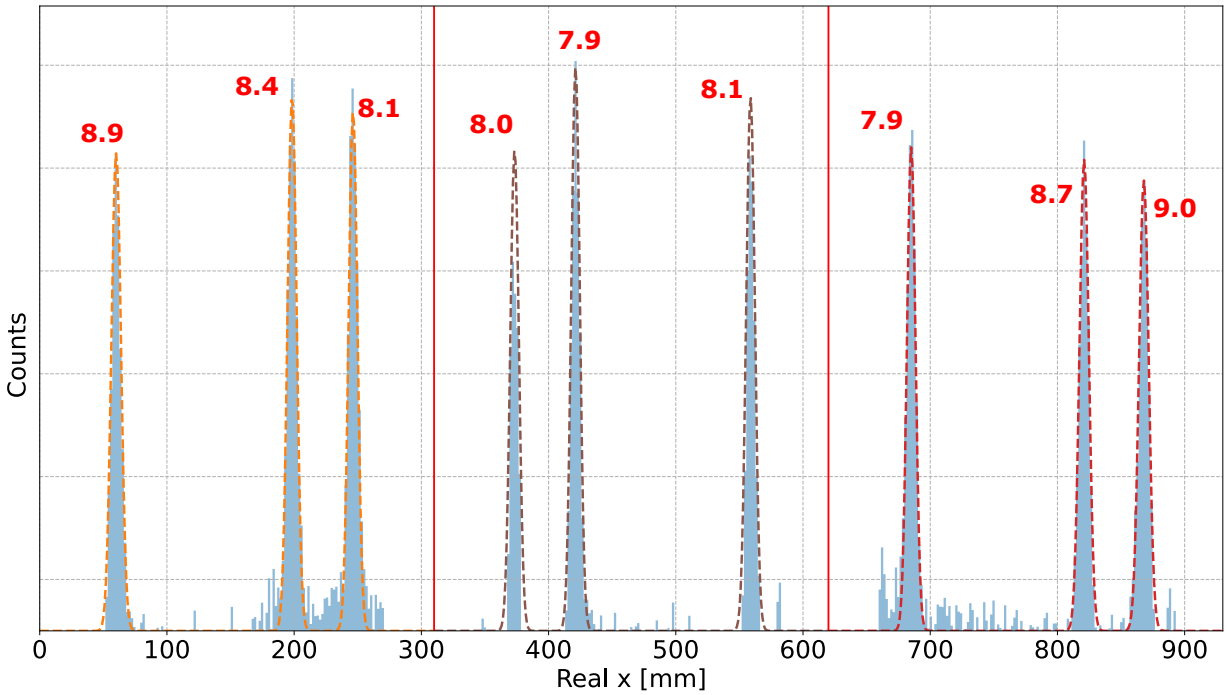

Figure 4.13: Real background-subtracted position spectrum of channel 7 of configuration C. The red horizontal lines denote the separation of each ^{3}He-tube. The reconstructed FWHM$_k$ of each Gaussian peak is denoted by the red texts, in units of mm.

Table 4.7: Reconstructed FWHM$_k$, FWHM$_s$, and intrinsic FWHM$_d$ values of each Gaussian peak of each tube for channel 7 of configuration A. The lowest reconstructed FWHM$_k$ and intrinsic FWHM$_d$ are highlighted in bold.

Configuration A - Channel 7			
Gaussian Peak	i	ii	iii
Tube 0			
FWHM$_k$ [mm]	10.6 ± 0.7	10.2 ± 0.6	9.2 ± 0.6
FWHM$_s$ [mm]	3.1 ± 0.1	3.1 ± 0.1	3.1 ± 0.1
FWHM$_d$ [mm]	10.2 ± 0.7	9.7 ± 0.6	8.6 ± 0.6
Tube 1			
FWHM$_k$ [mm]	$\mathbf{7.6 \pm 0.6}$	8.1 ± 0.4	9.2 ± 0.5
FWHM$_s$ [mm]	3.1 ± 0.1	3.1 ± 0.1	3.1 ± 0.1
FWHM$_d$ [mm]	$\mathbf{6.9 \pm 0.6}$	7.5 ± 0.5	8.7 ± 0.5
Tube 2			
FWHM$_k$ [mm]	8.6 ± 0.7	9.8 ± 0.7	8.3 ± 0.7
FWHM$_s$ [mm]	3.1 ± 0.1	3.1 ± 0.1	3.1 ± 0.1
FWHM$_d$ [mm]	8.1 ± 0.7	9.3 ± 0.7	7.7 ± 0.7

Table 4.8: Reconstructed $FWHM_k$, $FWHM_s$, and intrinsic $FWHM_d$ values of each Gaussian peak of each tube for channel 7 of configuration B. The lowest reconstructed $FWHM_k$ and intrinsic $FWHM_d$ are highlighted in bold.

Configuration B - Channel 7			
Gaussian Peak	i	ii	iii
Tube 0			
$FWHM_k$ [mm]	9.7 ± 0.4	8.2 ± 0.4	7.9 ± 0.3
$FWHM_s$ [mm]	3.1 ± 0.1	3.1 ± 0.1	3.1 ± 0.1
$FWHM_d$ [mm]	9.1 ± 0.4	7.6 ± 0.4	7.3 ± 0.4
Tube 1			
$FWHM_k$ [mm]	$\mathbf{7.1 \pm 0.3}$	7.7 ± 0.3	7.9 ± 0.3
$FWHM_s$ [mm]	3.1 ± 0.1	3.1 ± 0.1	3.1 ± 0.1
$FWHM_d$ [mm]	$\mathbf{6.4 \pm 0.3}$	7.0 ± 0.3	7.4 ± 0.3
Tube 2			
$FWHM_k$ [mm]	7.7 ± 0.3	8.4 ± 0.3	8.3 ± 0.3
$FWHM_s$ [mm]	3.1 ± 0.1	3.1 ± 0.1	3.1 ± 0.1
$FWHM_d$ [mm]	7.1 ± 0.3	7.8 ± 0.3	7.7 ± 0.4

Table 4.9: Reconstructed $FWHM_k$, $FWHM_s$, and intrinsic $FWHM_d$ values of each Gaussian peak of each tube for channel 7 of configuration C. The lowest reconstructed $FWHM_k$ and intrinsic $FWHM_d$ are highlighted in bold.

Configuration C - Channel 7			
Gaussian Peak	i	ii	iii
Tube 0			
$FWHM_k$ [mm]	8.9 ± 0.3	8.4 ± 0.2	8.1 ± 0.2
$FWHM_s$ [mm]	3.1 ± 0.1	3.1 ± 0.1	3.1 ± 0.1
$FWHM_d$ [mm]	8.3 ± 0.3	7.8 ± 0.3	7.5 ± 0.3
Tube 1			
$FWHM_k$ [mm]	8.0 ± 0.3	$\mathbf{7.9 \pm 0.2}$	8.1 ± 0.2
$FWHM_s$ [mm]	3.1 ± 0.1	3.1 ± 0.1	3.1 ± 0.1
$FWHM_d$ [mm]	7.3 ± 0.3	$\mathbf{7.3 \pm 0.2}$	7.5 ± 0.3
Tube 2			
$FWHM_k$ [mm]	7.9 ± 0.2	8.7 ± 0.2	9.0 ± 0.3
$FWHM_s$ [mm]	3.1 ± 0.1	3.1 ± 0.1	3.1 ± 0.1
$FWHM_d$ [mm]	7.3 ± 0.3	8.1 ± 0.3	8.4 ± 0.3

5 Summary and Outlook

This thesis has detailed the experimental work undertaken at LLB Saclay, France, wherein the principal goal of the experiment was to determine the performance of the ^{3}He-triplet detector system of the BIFROST instrument using an Am/Be neutron source. Slow neutron measurements with the three configurations of the ^{3}He-triplets using an Am/Be neutron source and moderator were performed. The position reconstruction spectra from selected ^{3}He-triplets were fitted using a superfunction, returning the best-fit parameters of the Gaussian peaks created from the slits of the Cd-mask. Finally, the performance of the position reconstruction is determined in terms of both the position reconstruction resolution, and the intrinsic spatial resolution of the detector system. At the time of writing, preparations for delivering the ^{3}He detector system to ESS has begun.

5.1 Attainment of Project Goals and Statement of Key Findings

The project goals stated in Section 1.2 were attained, as enumerated in the points below.

1. To validate the novel digitiser and the whole digital pulse processing read-out system, the pulse-height spectra and position reconstruction spectra from the measurement runs were analysed. The analysis of the pulse-height spectra validated the measured events as neutron-capture events expected from a ^{3}He-detector, while the analysis of the position reconstruction spectra validated the position-sensitivity capabilities of the ^{3}He-detector. The applied HV of 1400 V was close to the recommended upper limit by the manufacturer but benefited the position reconstruction performance.

2. The position reconstruction resolution and intrinsic spatial resolution of the ^{3}He-detectors was determined, providing a quantitative determination of the initial performance of the detector system.

3. Considering both the performance, and the overall functionality and stability of the ^{3}He-detector system, a qualitative and quantitative case may be presented in support for the approval of the factory acceptance test.

The key findings are as listed:

- The shape of the pulse-height spectra validates the measurement data as neutron-capture events.

- The digital pulse processing chain is able to separate between the read-out amplitudes A and B, and perform charge-division (Equation 2.5) to determine the reconstructed position of an event along a ^{3}He-triplet to an average position resolution of ~ 9 mm.

- The superfunction (Equation 4.1) can be used to fit the ROI of each tube in a position spectrum, albeit with under-fitting as indicated by the reduced chi-square values. The Gaussian peaks, however, can be fitted with reasonable confidence.
- The position reconstruction performance of the digital pulse processing chain is most reliable at the centre of tube 1. However, due to the continuous RC-circuit characteristic of position-sensitive ^{3}He-detectors, this performance is not as reliable at the read-out ends of tube 0 and tube 2, resulting in a non-linear response along the ^{3}He-triplet.
- A ^{3}He-triplet may be unpacked (Figure 4.8), whereupon a linear calibration function (Equation 4.3), using the fitted centroid (μ) values of the Gaussian peaks, converts the bin positions of the position spectra to physical lengths with reasonable confidence.
- The fitted standard deviation (σ) values of the Gaussian peaks, after conversion to physical length scale, can be used to determine the position reconstruction resolution based on FWHM$_k$.
- The intrinsic spatial resolution can furthermore be determined using Equation 4.6, meeting the position resolution performance requirement of $\sim 1\%$ of the total length of a ^{3}He-triplet (discussed in Section 1.1.1).

5.2 Future Work and Upgrades

The recommended future work is listed below:

1. To use a collimated beam of neutrons, from a fixed position, to illuminate the ^{3}He-detector system to reduce geometric and scattering effects caused by the position of the neutron source.
2. The separation of each tube in a position spectrum is created by the resistors between the ^{3}He-tubes (see Figure 3.1 (a)). The relationship between the resistance value and separation should be characterised to allow for an improved linear calibration of the bin positions.
3. To further investigate and optimise the reliability of position reconstruction by changing the characteristics of the RC-circuit of the ^{3}He-triplet using resistors of different values.

Acknowledgements

I would like to thank, first and foremost, my supervisors, Irina and Kristina, and my co-supervisor, Nicholai. Thank you, Irina, for offering me this project, and the warm welcome when I first joined the Detector Group, as well as the support in getting me settled and up-to-date with how the group, and ESS as a whole, functions. Thank you for enthusiastically sharing your knowledge and expertise whenever I had questions, and of course involving me with your numerous projects that allowed me to learn and apply myself to the fullest extent. Thank you, Kristina, for stepping-in to be my supervisor, and giving advice to help me focus on my thesis project. Thank you, Nicholai, for your technical expertise and data analysis advice, and for explaining concepts that would've taken hours of reading literature to understand. To all my supervisors, thank you for the constant feedback, comments, and discussions when I was writing this thesis, and for challenging me where needed so that I fully understand and convey correctly the theoretical concepts, data analysis, and results.

To Rasmus, thank you for the discussions and measurement data sets during the factory acceptance test at LLB Saclay, and to Philippe and all involved during our time at LLB, thank you for hosting us and expertise in running the experiment.

To Kevin Fissum, thank you for introducing me to the Detector group when I was looking for a masters thesis project, and checking-in on my work whenever possible. I appreciate the interest and ideas you gave whenever you came by for a quick chat. To Alex and Nathaly, thank you for your ideas and discussions in understanding the data, and on how to present them. To Hanno, for being my first supervisor, and priming me on working outside of the university setting. To everyone at the Detector Group, thank you for the great and sometimes informative stories during my time at Utgård!

References

[1] K. H. Andersen, D. N. Argyriou, A. J. Jackson, *et al.* The instrument suite of the European Spallation Source. *Nuclear Instruments and Methods in Physics Research Section A: Accelerators, Spectrometers, Detectors and Associated Equipment*, vol. 957 (2020), 163402. doi:10.1016/j.nima.2020.163402

[2] M. Klausz, K. Kanaki, T. Kittelmann, *et al.* A simulational study of the indirect-geometry neutron spectrometer BIFROST at the European Spallation Source, from neutron source position to detector position. *Journal of Applied Crystallography*, vol. 54 (2021), 263–279. doi:10.1107/S1600576720016192

[3] F. Groitl, E. Rantsiou, M. Bartkowiak, *et al.* A combined radial collimator and cooled beryllium filter for neutron scattering. *Nuclear Instruments and Methods in Physics Research Section A: Accelerators, Spectrometers, Detectors and Associated Equipment*, vol. 819 (2016), 99–103. doi:10.1016/j.nima.2016.02.056

[4] M. Markó, F. Groitl, J. O. Birk, *et al.* Prototype of the novel CAMEA concept—A backend for neutron spectrometers. *Review of Scientific Instruments*, vol. 89 (2018), 015105. doi:10.1063/1.5018233

[5] F. Groitl, D. Graf, J. O. Birk, *et al.* CAMEA—A novel multiplexing analyzer for neutron spectroscopy. *Review of Scientific Instruments*, vol. 87 (2016), 035109. doi:10.1063/1.4943208

[6] H. Ronnow. ESS Instrument Construction Proposal - CAMEA (2013). URL `https://ess-public-legacy.esss.se/sites/default/files/camea_proposal_0.pdf`

[7] J. Chadwick. The existence of a neutron. *Proceedings of the Royal Society of London. Series A, Containing Papers of a Mathematical and Physical Character*, vol. 136 (1932), 692–708. doi:10.1098/rspa.1932.0112

[8] E. Rutherford. LIV. Collision of α particles with light atoms. IV. An anomalous effect in nitrogen. *The London, Edinburgh, and Dublin Philosophical Magazine and Journal of Science*, vol. 37 (1919), 581–587. doi:10.1080/14786440608635919

[9] J. J. Thomson. XL. Cathode Ray. *The London, Edinburgh, and Dublin Philosophical Magazine and Journal of Science*, vol. 44 (1897), 293–316. doi:10.1080/14786449708621070

[10] T. Prohaska, J. Irrgeher, J. Benefield, *et al.* Standard atomic weights of the elements 2021 (IUPAC Technical Report). *Pure and Applied Chemistry*, vol. 94 (2022), 573–600. doi:10.1515/pac-2019-0603

[11] G. Gamow. Mass defect curve and nuclear constitution. *Proceedings of the Royal Society of London. Series A, Containing Papers of a Mathematical and Physical Character*, vol. 126 (1930), 632–644. doi:10.1098/rspa.1930.0032

[12] C. F. v. Weizsäcker. Zur Theorie der Kernmassen. *Zeitschrift für Physik*, vol. 96 (1935), 431–458. doi:10.1007/BF01337700

[13] H. A. Bethe. Nuclear Physics B. Nuclear Dynamics, Theoretical. *Reviews of Modern Physics*, vol. 9 (1937), 69–244. doi:10.1103/RevModPhys.9.69

[14] E. Rutherford. Discussion on the structure of atomic nuclei. *Proceedings of the Royal Society of London. Series A, Containing Papers of a Mathematical and Physical Character*, vol. 123 (1929), 373–390. doi:10.1016/b978-0-08-006630-1.50010-6

[15] E. Gapon, D. Iwanenko. Zur Bestimmung der Isotopenzahl. *Die Naturwissenschaften*, vol. 20 (1932), 792–793. doi:10.1007/bf01494007

[16] E. Feenberg, E. Wigner. On the Structure of the Nuclei Between Helium and Oxygen. *Physical Review*, vol. 51 (1937), 95–106. doi:10.1103/physrev.51.95

[17] M. G. Mayer. On Closed Shells in Nuclei. *Physical Review*, vol. 74 (1948), 235–239. doi:10.1103/physrev.74.235

[18] M. G. Mayer. On Closed Shells in Nuclei. II. *Physical Review*, vol. 75 (1949), 1969–1970. doi:10.1103/physrev.75.1969

[19] O. Haxel, J. H. D. Jensen, H. E. Suess. On the "Magic Numbers" in Nuclear Structure. *Physical Review*, vol. 75 (1949), 1766–1766. doi:10.1103/physrev.75.1766.2

[20] A. Belyaev, D. Ross. *Nuclear Masses and the Semi-Empirical Mass Formula*, 37–52. Springer International Publishing (2021). doi:10.1007/978-3-030-80116-8_3

[21] K. S. Krane. *Introductory Nuclear Physics*, chap. 3. Nuclear Properties, 44–79. Wiley, New York, NY (1988)

[22] A. Belyaev, D. Ross. *The Basics of Nuclear and Particle Physics*, chap. 4. The Nuclear Shell Model, 53–66. Springer International Publishing, Cham (2021). ISBN 978-3-030-80116-8. doi:10.1007/978-3-030-80116-8

[23] G. F. Knoll. *Radiation Detection and Measurement 4th ed.*, chap. 6. Proportional Counters, 159–206. John Wiley & Sons, Inc. (2010)

[24] A. Belyaev, D. Ross. *The Basics of Nuclear and Particle Physics*, chap. 5. Radioactivity, 67–88. Springer International Publishing, Cham (2021). ISBN 978-3-030-80116-8. doi:10.1007/978-3-030-80116-8_5

[25] K. S. Krane. *Introductory Nuclear Physics*, chap. 5. Nuclear Models, 116–158. Wiley, New York, NY (1988)

[26] A. Belyaev, D. Ross. Gamma Decay, In *The Basics of Nuclear and Particle Physics*, 127–144. Springer International Publishing (2021). doi:10.1007/978-3-030-80116-8_8

[27] K. S. Krane. *Introductory Nuclear Physics*, chap. 10. Gamma Decay, 327–377. Wiley, New York, NY (1988)

[28] N. Bohr. Transmutations of Atomic Nuclei. *Science*, vol. 86 (1937), 161–165. doi:10.1126/science.86.2225.161

[29] V. Weisskopf. The formation of the compound nucleus. *Physica*, vol. 22 (1956), 952–958. doi:10.1016/s0031-8914(56)90052-0

[30] J. Carpenter, C. K. Loong. About neutrons, In *Elements of Slow-Neutron Scattering*, 10–48. Cambridge University Press (2015). doi:10.1017/cbo9781139029315.004

[31] W. R. Leo. Passage of Radiation Through Matter, In *Techniques for Nuclear and Particle Physics Experiments*, chap. 2. Passage of Radiation Through Matter, 17–68. Springer Berlin Heidelberg (1994). doi:10.1007/978-3-642-57920-2_2

[32] G. F. Knoll. *Radiation Detection and Measurement 4th ed.*, chap. 2. Radiation Interaction, IV: Interaction of Neutrons, 53–55. John Wiley & Sons, Inc. (2010)

[33] D. A. Shea, D. L. Morgan. The helium-3 shortage: Supply, demand, and options for congress (2010)

[34] G. F. Knoll. *Radiation Detection and Measurement 4th ed.*, chap. 14. Slow Neutron Detection Methods, 519–552. John Wiley & Sons, Inc. (2010)

[35] Detectors, In *Elements of Slow-Neutron Scattering*, 281–314. Cambridge University Press (2015). doi:10.1017/cbo9781139029315.011

[36] D. Brown, M. Chadwick, R. Capote, *et al.* ENDF/B-VIII.0: The 8th Major Release of the Nuclear Reaction Data Library with CIELO-project Cross Sections, New Standards and Thermal Scattering Data. *Nuclear Data Sheets*, vol. 148 (2018), 1–142. doi:10.1016/j.nds.2018.02.001

[37] Z. Ge, R. Xu, H. Wu, *et al.* CENDL-3.2: The new version of Chinese general purpose evaluated nuclear data library. *EPJ Web of Conferences*, vol. 239 (2020), 09001. doi:10.1051/epjconf/202023909001

[38] G. F. Knoll. *Radiation Detection and Measurement 4th ed.*, chap. 1. Radiation Sources, V: Neutron Sources, 19–26. John Wiley & Sons, Inc. (2010)

[39] W. R. Leo. Basic Nuclear Processes in Radioactive Sources, In *Techniques for Nuclear and Particle Physics Experiments*, chap. 1. Basic Nuclear Processes in Radioactive Sources, 1–15. Springer Berlin Heidelberg (1994). doi:10.1007/978-3-642-57920-2_1

[40] J. Marsh, D. Thomas, M. Burke. High resolution measurements of neutron energy spectra from AmBe and AmB neutron sources. *Nuclear Instruments and Methods in Physics Research Section A: Accelerators, Spectrometers, Detectors and Associated Equipment*, vol. 366 (1995), 340–348. doi:10.1016/0168-9002(95)00613-3

[41] J. Carpenter, C. K. Loong. Neutron production, moderation, and characterization of sources, In *Elements of Slow-Neutron Scattering*, 49–86. Cambridge University Press (2015). doi:10.1017/cbo9781139029315.005

[42] K. C. Kelley. *Gadolinium-148 and other spallation production cross section measurements for accelerator target facilities*. Ph.D. thesis (2004)

[43] A. Didi, M. Bencheikh, A. Dadouch, *et al.* Spallation Yield of Neutrons Produced in Tungsten and Bismuth Target Bombarded with 0.1 to 3 GeV Proton Beam. *Moscow University Physics Bulletin*, vol. 73 (2018), 612–617. doi:10.3103/S0027134918060085

[44] J. Habainy, Y. Dai, Y. Lee, S. Iyengar. Mechanical properties of tungsten irradiated with high-energy protons and spallation neutrons. *Journal of Nuclear Materials*, vol. 514 (2019), 189–195. doi:10.1016/j.jnucmat.2018.12.003

[45] J. S. E. Townsend. IV. The diffusion of ions into gases. *Philosophical Transactions of the Royal Society of London. Series A, Containing Papers of a Mathematical or Physical Character*, vol. 193 (1900), 129–158. doi:10.1098/rsta.1900.0004

[46] W. R. Leo. Ionization Detectors, In *Techniques for Nuclear and Particle Physics Experiments*, chap. 6. Ionization Detectors, 127–156. Springer Berlin Heidelberg (1994). doi:10.1007/978-3-642-57920-2_6

[47] M. McPheeters, K. McKinny, E. Yokie. Position and gain non-uniformities in Helium-3 filled position sensitive proportional counters. *Nuclear Instruments and Methods in Physics Research Section A: Accelerators, Spectrometers, Detectors and Associated Equipment*, vol. 1040 (2022), 167156. doi:10.1016/j.nima.2022.167156

[48] B. Fischer. A digital processor for position sensitive detectors. *Nuclear Instruments and Methods*, vol. 141 (1977), 173–181. doi:10.1016/0029-554x(77)90763-7

[49] V. Popov, S. Majewski, A. Weisenberger, R. Wojcik. Analog readout system with charge division type output. In *2001 IEEE Nuclear Science Symposium Conference Record (Cat. No.01CH37310)* (2001). IEEE. doi:10.1109/nssmic.2001.1009203

[50] G. F. Knoll. *Radiation Detection and Measurement 4th ed.*, chap. 16. Pulse Processing, 595–624. John Wiley & Sons, Inc. (2010)

[51] G. F. Knoll. *Radiation Detection and Measurement 4th ed.*, chap. 17. Pulse Shaping, Counting, and Timing, 625–704. John Wiley & Sons, Inc. (2010)

[52] G. F. Knoll. *Radiation Detection and Measurement 4th ed.*, chap. 18. Multichannel Pulse Analysis, 705–732. John Wiley & Sons, Inc. (2010)

[53] W. R. Leo. Electronics for Pulse Signal Processing, In *Techniques for Nuclear and Particle Physics Experiments*, chap. 14. Electronics for Pulse Signal Processing, 277–302. Springer Berlin Heidelberg (1994). doi:10.1007/978-3-642-57920-2_14

[54] CAEN. R5560. URL `https://www.caen.it/products/r5560/`

[55] Leviton. Cat 6A: Interactive Reference Guide. URL `https://www.anixter.com/content/dam/Suppliers/Leviton/Brochures/Leviton-Cat6AReferenceGuide.051518pdf.pdf`

[56] R. Conway. ESS: BIFROST Instrument. Confidential Private Correspondence (2021)

[57] Python 3.11.7 documentation. URL `https://docs.python.org/3.11/`

[58] pandas documentation (2023). URL `https://pandas.pydata.org/pandas-docs/version/2.0.0/`

[59] C. R. Harris, K. J. Millman, S. J. van der Walt, *et al.* Array programming with NumPy. *Nature*, vol. 585 (2020), 357–362. doi:10.1038/s41586-020-2649-2

[60] P. Virtanen, R. Gommers, T. E. Oliphant, *et al.* SciPy 1.0: Fundamental Algorithms for Scientific Computing in Python. *Nature Methods*, vol. 17 (2020), 261–272. doi:10.1038/s41592-019-0686-2

[61] E. Rossi. *Characterisation of the Spatial Resolution and the Gamma-ray Discrimination of Helium-3 Proportional Counters*. Master's thesis (2017). doi:10.48550/ARXIV.1702.06501

[62] F. Piscitelli. Report on the IN5 Demonstrator: Electronic Needs. Private Correspondence (2014)

[63] M. K. Kopp, C. J. Borkowski. Position-sensitive proportional counters using resistance-capacitance position encoding. Tech. rep. (1975). doi:10.2172/4130048

[64] X.-F. Jiang, J.-R. Zhou, H. Luo, *et al.* A large area ^{3}He tube array detector with vacuum operation capacity for the SANS instrument at the CSNS. *Nuclear Science and Techniques*, vol. 33 (2022), 1–10. doi:10.1007/s41365-022-01067-1

[65] A. Uritani, N. Marnada, Y. Takenaka, C. Mori, H. Miyahara. A study on the position resolution of position-sensitive ^{3}He proportional counters. *Nuclear Instruments and Methods in Physics Research Section A: Accelerators, Spectrometers, Detectors and Associated Equipment*, vol. 350 (1994), 286–290. doi:10.1016/0168-9002(94)91175-4

Appendices

Pulse-Height Spectra and Heat-maps of the Detector Modules

Measurement runs of the three configurations were taken with the Am/Be neutron source at the LLB, Saclay, France. The neutron source locations, and measurement times are as listed:

- Configuration A
  A_H: Source-to-detector distance: 140 cm, Height: 120 cm, Run-time: 3.33 hrs
  A_L: Source-to-detector distance: 210 cm, Height: 40 cm, Run-time: 16.33 hrs

- Configuration B
  Source-to-detector distance: 185 cm, Height: 120 cm, Run-time: 15.07 hrs

- Configuration C
  C_H: Source-to-detector distance: 175 cm, Height: 100 cm, Run-time: 24.04 hrs
  C_L: Source-to-detector distance: 175 cm, Height: 50 cm, Run-time: 18.57 hrs

Note that the measurement runs introduced in Section 3.2 for configuration A and C is relabelled to A_H and C_H to reflect the additional two measurement runs, A_L and C_L. The two additional measurement runs were performed to better illuminate arcs 0 and 1 of the detector modules and thus have a complete characterisation of all tubes of all triplets included in this configuration. Figure A.1 illustrates the experimental set-up of all five measurement runs.

Figures A.2 - A.6 is the pulse-height spectra of all 15 channels of each configuration, of each measurement run. Figures A.7 - A.11 show the heat-map of *each tube* of all 15 channels of each measurement run. By observing the pulse-height spectrum and corresponding heat-map of a channel, an "at a glance" determination of the operational status of the ^{3}He-tube and -triplet may be determined. For example, the pulse-height spectrum of channel 0 of measurement run A_H is reasonable, while channel 14 of the same measurement run is not. Coupled with the distribution of event counts between the three tubes of the corresponding channels presented in the heat-map, where the distribution for channel 0 is observed to be within the same magnitude, while not for channel 14. These observations raises questions for channel 14; is the ^{3}He-triplet functioning properly? Or is there some electrical issue caused by sparking?

Another thought with the heat-map was to illustrate, and determine, if the position of the Am/Be neutron source affects the number of counts registered by the detector modules. A consistent pattern in the difference in counts between the ^{3}He-tubes in a ^{3}He-triplet may hint at geometric and "shadowing" effects caused by scattering of the incident neutrons. It is observed that in some channels, tube 2 under-counts slightly as compared to tubes 0 and 1, but an overall consistent pattern is not observed.

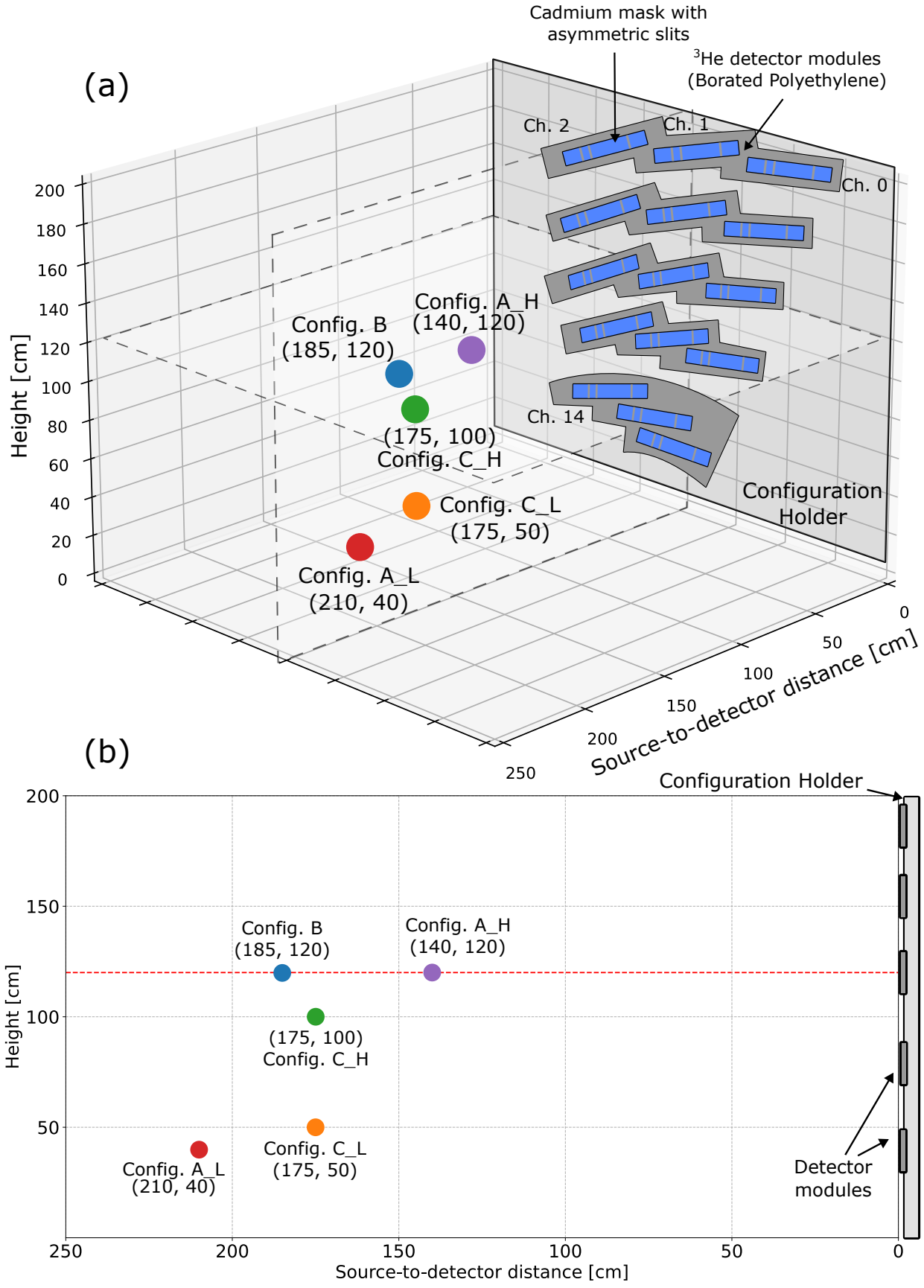

Figure A.1: (a) Isometric view of the experimental set-up. (b) Side-view of the experimental set-up. The neutron source locations for the three configurations are marked with their (source-to-detector, height) positions. The red dashed-line represents arc 2 of the detector module.

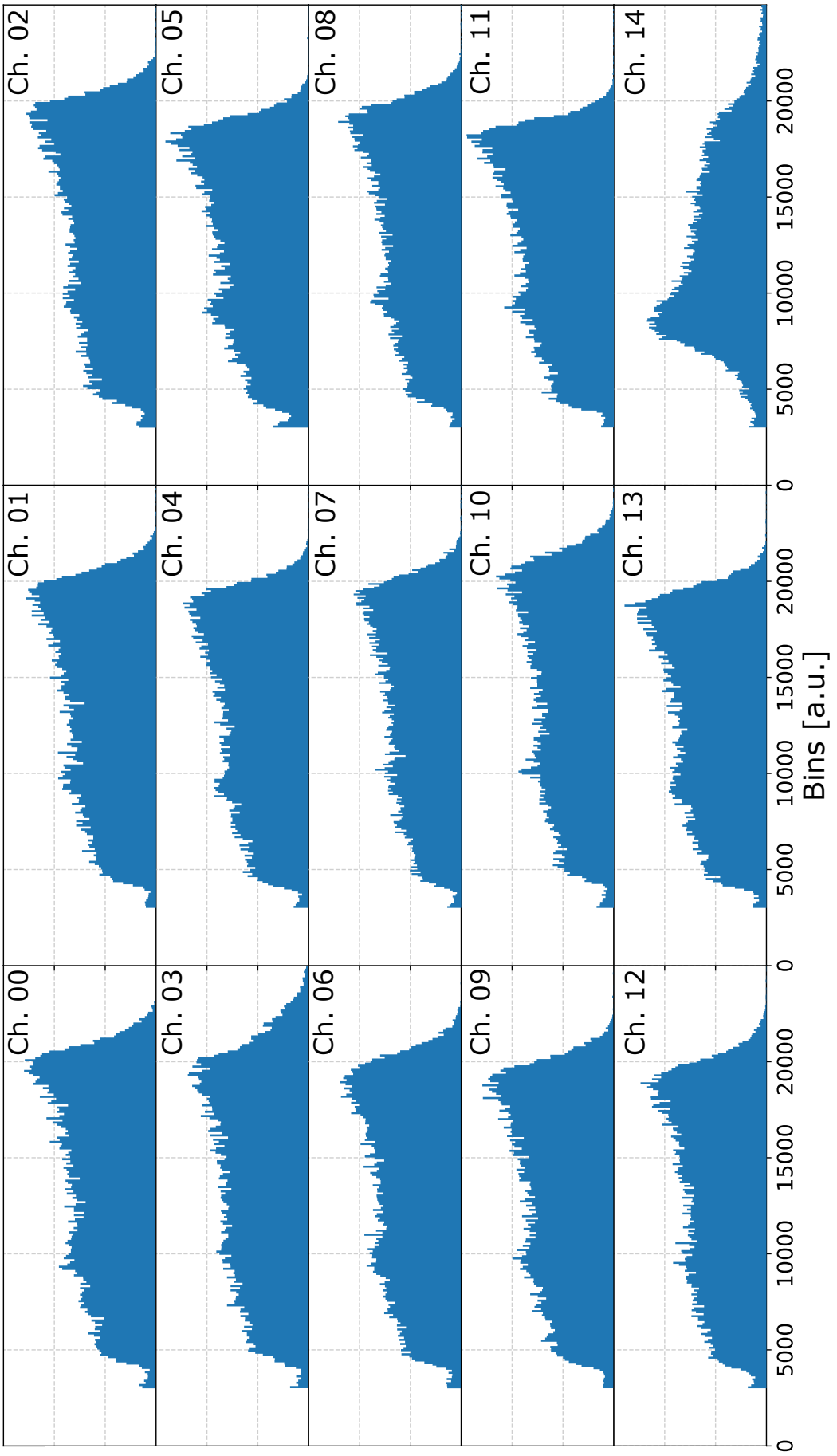

Figure A.2: Pulse-height spectra of configuration A, measurement run **A_H**.

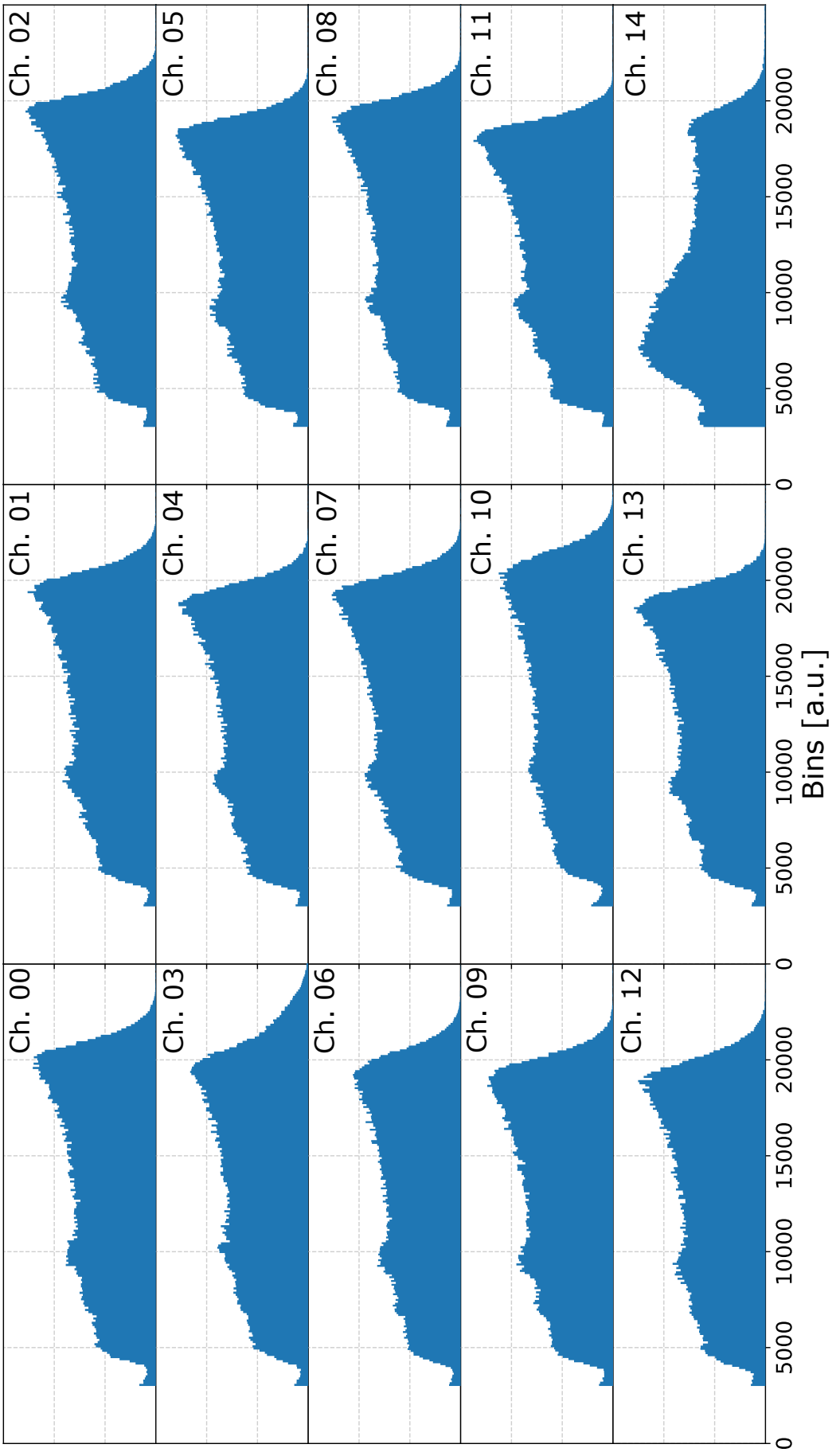

Figure A.3: Pulse-height spectra of configuration A, measurement run **A_L**.

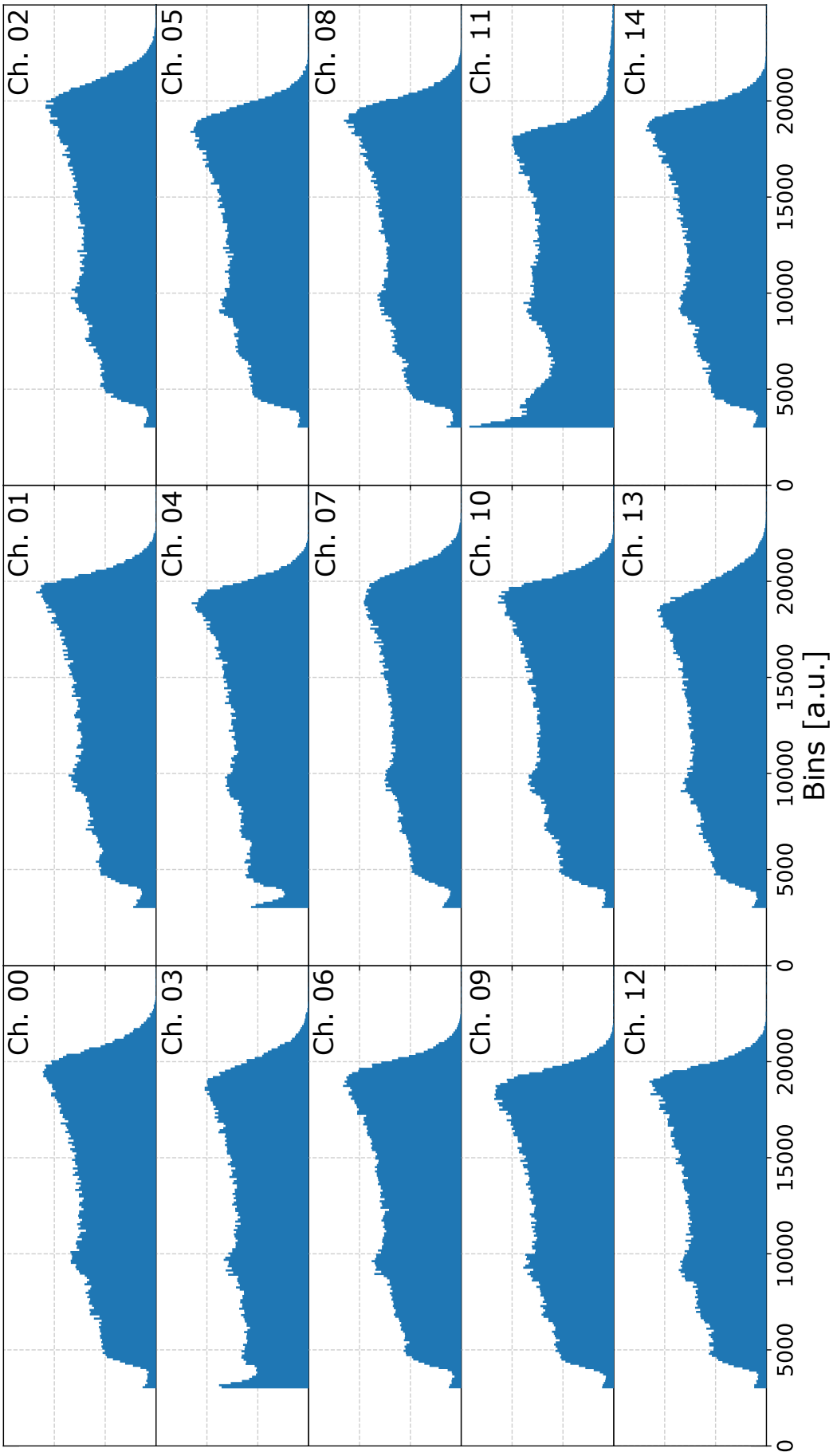

Figure A.4: Pulse-height spectra of configuration B, measurement run **B**.

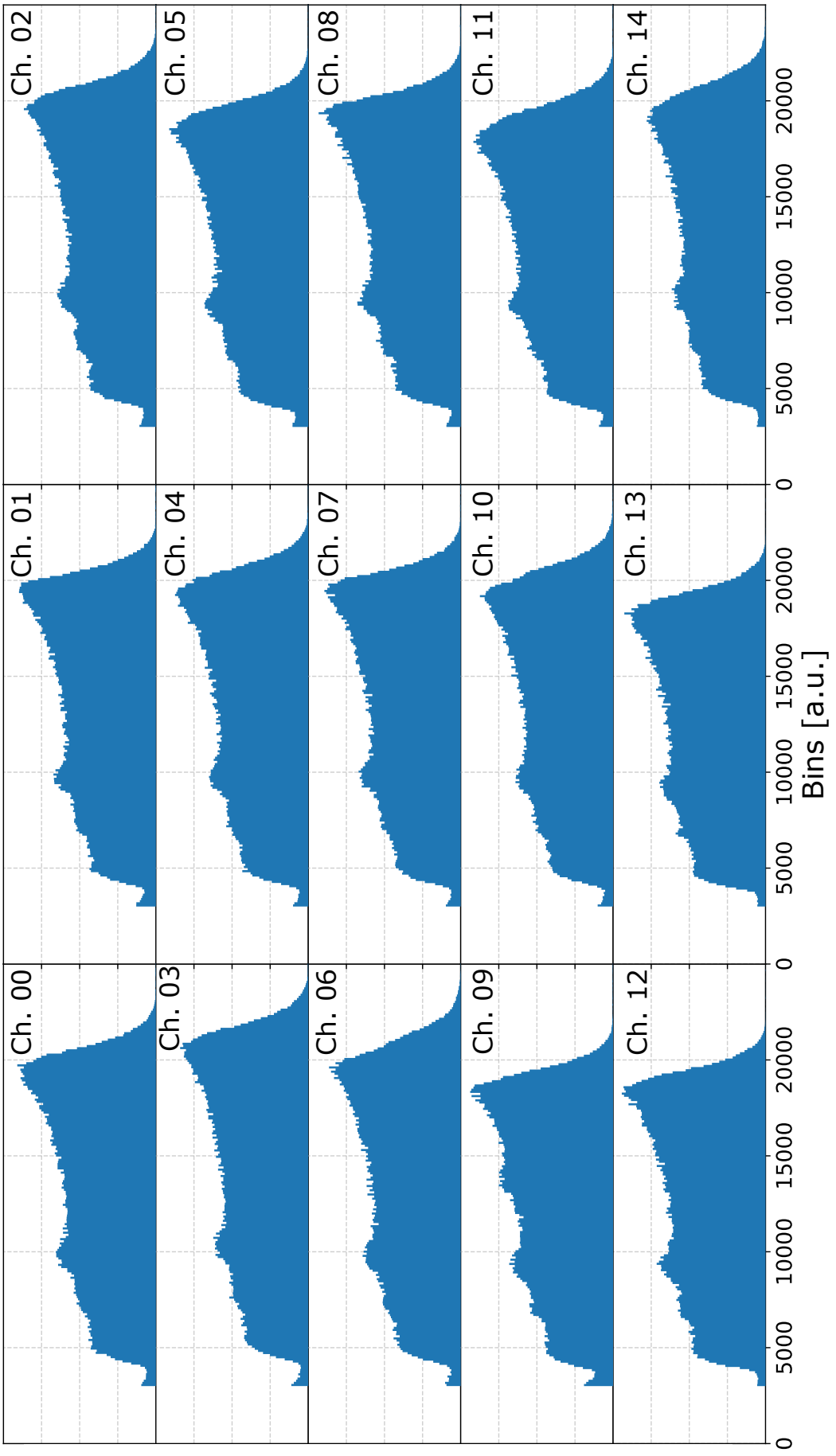

Figure A.5: Pulse-height spectra of configuration C, measurement run **C_H**.

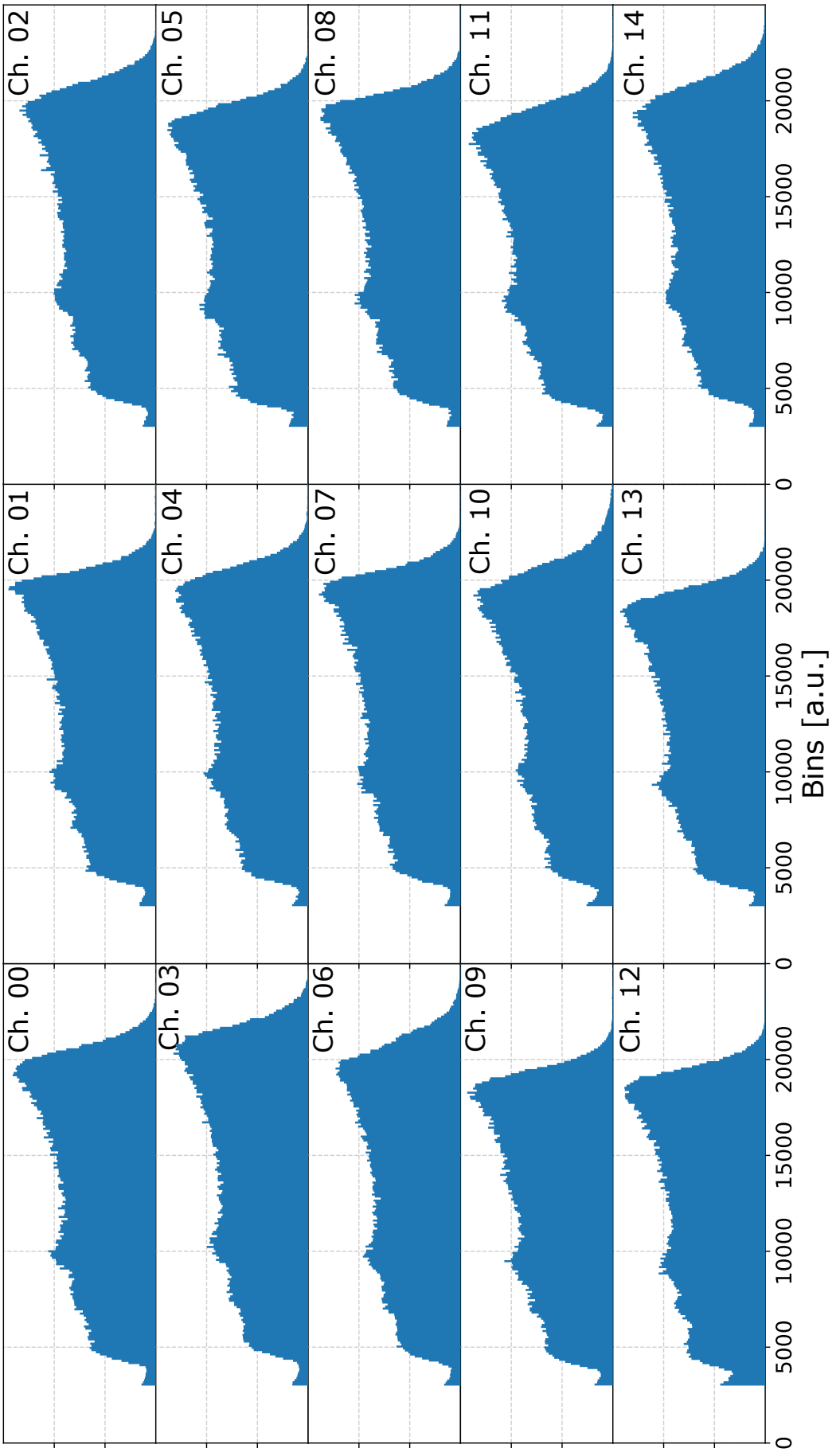

Figure A.6: Pulse-height spectra of configuration C, measurement run **C_L**.

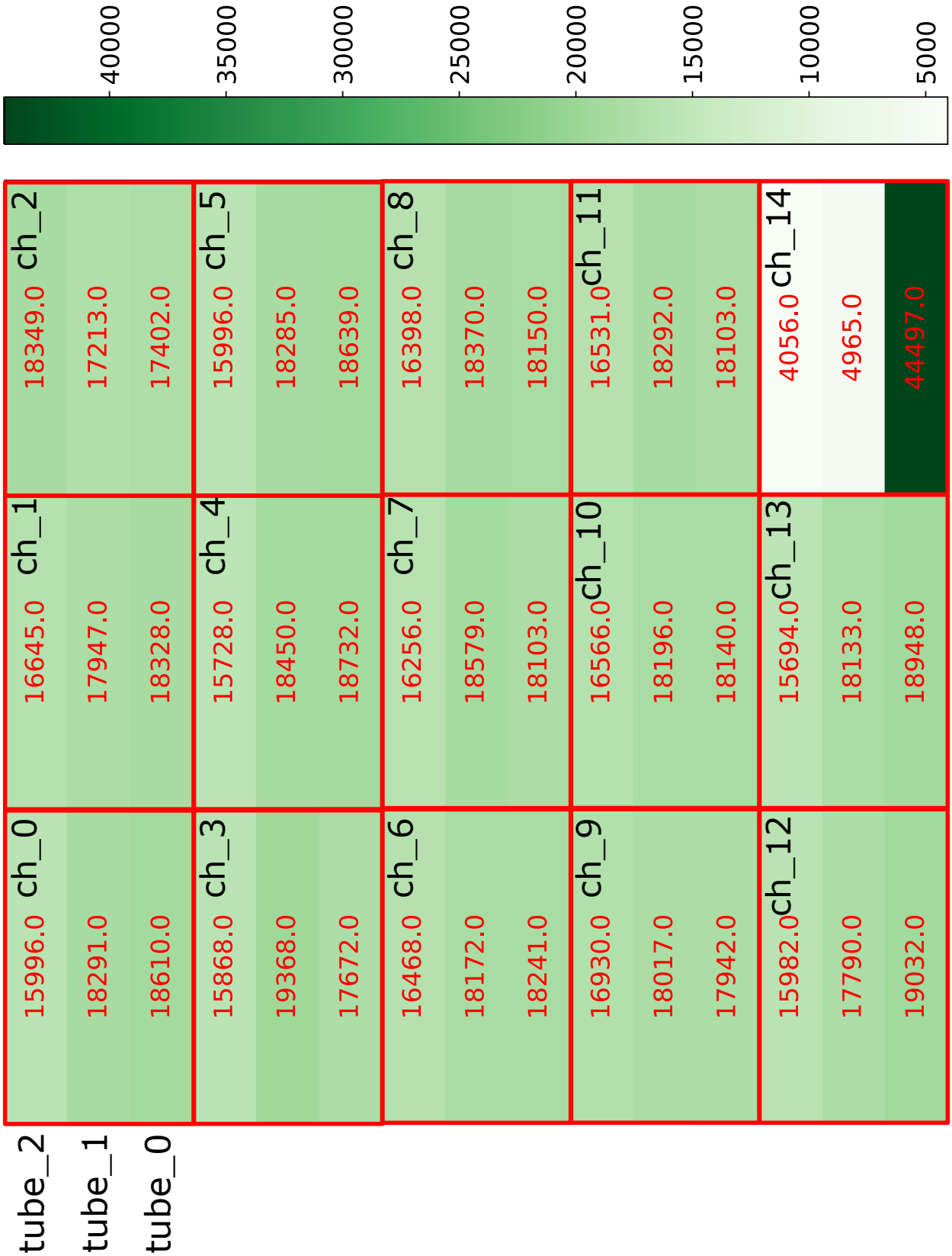

Figure A.7: Heat-map of configuration A, measurement run **A_H**.

Figure A.8: Heat-map of configuration A, measurement run **A_L**.

Figure A.9: Heat-map of configuration B, measurement run **B**.

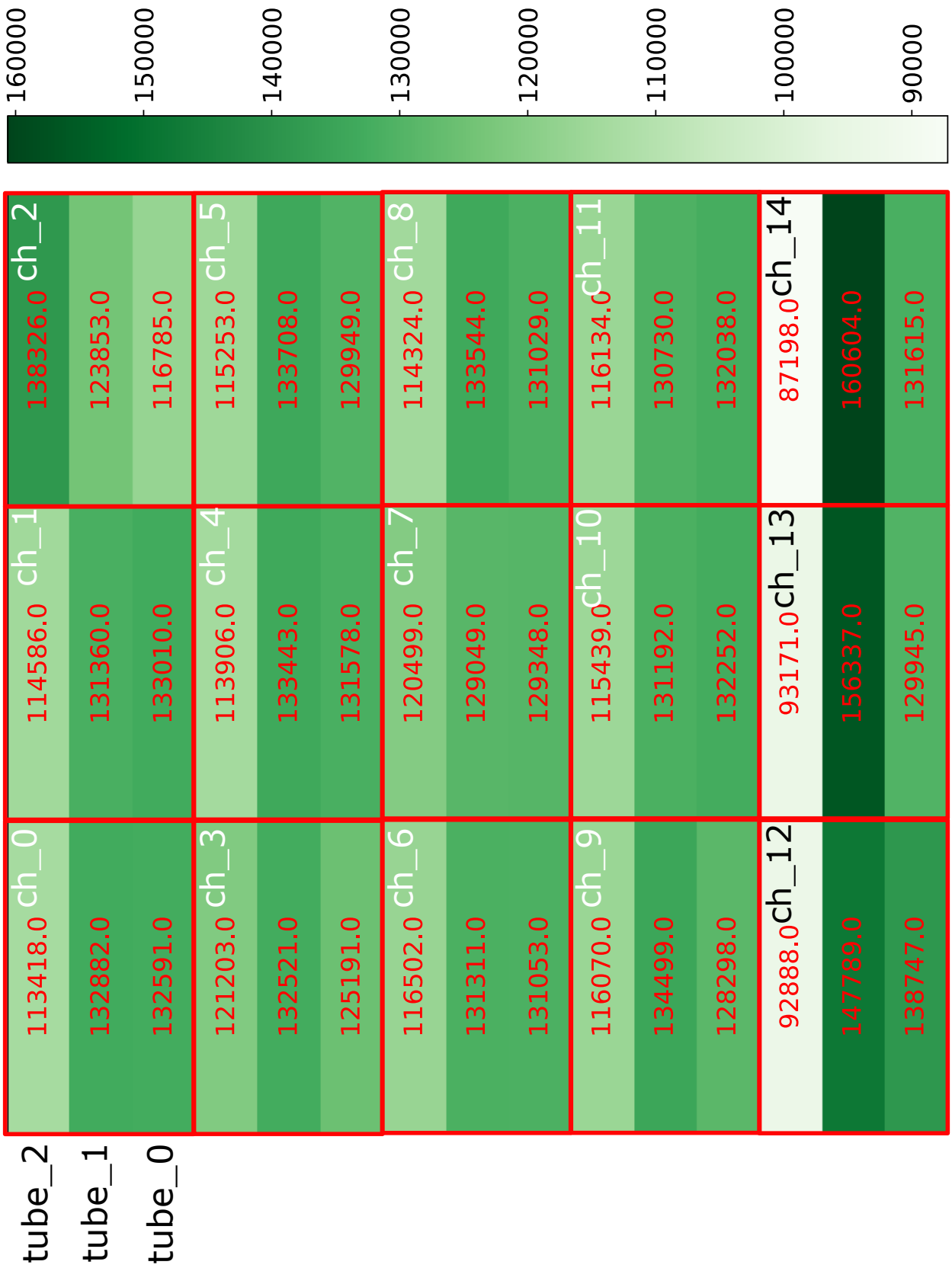

Figure A.10: Heat-map of configuration C, measurement run **C_H**.

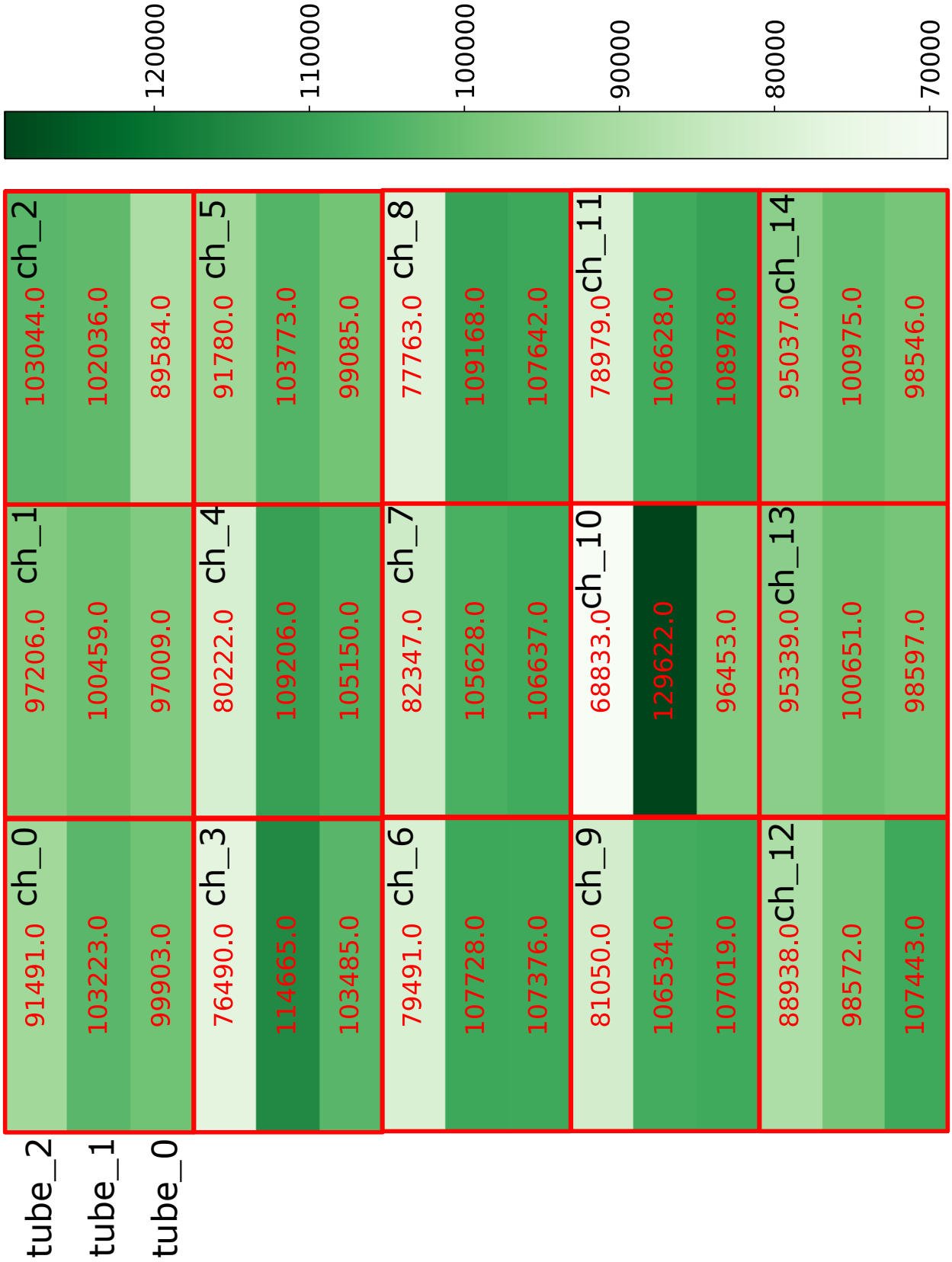

Figure A.11: Heat-map of configuration C, measurement run **C_L**.

Position Reconstruction Spectra

The source code, written in Python 3.11 programming language, presented directly below, is used to perform the piece-wise function fitting for each tube of a ^{3}He-triplet. The best-fit parameters, standard variation errors, and FWHM$_f$ is returned in a `.csv` file.

Figures B.1 - B.5 presents the position reconstruction spectra overlaid with the best-fit of the superfunction function of each tube for all 15 channels of the five measurement runs. Channels, or specific tubes, without an overlaid best-fit, indicate a failure to fit the spectra. This can be due to a lack of distinct peaks (e.g. measurement run **C_H** - channel 12-13), or flashing effects that have masked the peaks (e.g. measurement run **A_L** - channel 14).

```python
import glob
import os
import numpy as np
import matplotlib.pyplot as plt
import pandas as pd
import pickle
from scipy.optimize import curve_fit
from scipy.signal import find_peaks

'''
BIFROST piece-wise function fitting script

Splits each channel (triplet) into 3 tubes using fnc: binDataSlicer
Fits superfunction (fnc: s_fit) on each tube using curve_fit
Returns optimal parameters (from popt), FWHM, and standard deviation errors (from pcov)

User-input required to define superfunction boundaries,
and gaussian peak locations
'''

def binDataSlicer(x_input, y_input, start, stop):
    """
    Helper method for slicing binned x,y data-set between 'start' and 'stop' x-values.
    """
    y = np.empty(0)
    x = np.empty(0)
    for i in range(len(x_input)):
        if x_input[i] >= start and x_input[i] <= stop:
            x = np.append(x, x_input[i])
            #Get x-values in range to fit
            y = np.append(y, y_input[i])
            #Get y-values in range to fit
    return x, y

def s_fit(x, p2, p1, p0, # x-data and polynomial to 2nd degree
          a0, mu0, sig0, # Gaussian peaks
          a1, mu1, sig1,
          a2, mu2, sig2):
    ''' Superfunction to fit quadratic with three gaussian peaks on each tube '''
```

```
    poly = (p2*x**2)+(p1*x)+(p0)
    gaus0 = a0*np.exp(-((x-mu0)**2/(2.*sig0**2)))
    gaus1 = a1*np.exp(-((x-mu1)**2/(2.*sig1**2)))
    gaus2 = a2*np.exp(-((x-mu2)**2/(2.*sig2**2)))
    return poly + gaus0 + gaus1 + gaus2

# Create histogram of position spectra with specified bin number, datafile, and channel
bins=500; df=a_h; i=7
counts, binss = np.histogram(df[i].posx, bins)

# To identify a total of 9 Gaussian peaks of each channel
peaks, _ = find_peaks(counts, height=500, distance=20)

# Split histogram into each tube, splicing BETWEEN ROI. The tubes are named 0-2
t0=binDataSlicer(binss, counts, -0.929, -0.423)
t1=binDataSlicer(binss, counts, -0.252, 0.253)
t2=binDataSlicer(binss, counts, 0.425, 0.933)

# Fitting the superfunction, tube by tube
sig_g=0.01 # Inital parameter for sigma of gaussian peak; can be adjusted
fwhm=2*np.sqrt(2*np.log(2))

param0=np.array([1,1,1,
                 counts[peaks][0],binss[peaks][0], sig_g,
                 counts[peaks][1],binss[peaks][1], sig_g,
                 counts[peaks][2],binss[peaks][2], sig_g,
                 ])
popt_0, pcov_0 = curve_fit(s_fit, t0[0],t0[1], p0=param0)
perr_0 = np.sqrt(np.diag(pcov_0))
pfwhm_0= np.abs(np.array([fwhm*popt_0[5],fwhm*popt_0[8],fwhm*popt_0[11]]))
pfit_0 = pd.DataFrame([popt_0, perr_0, pfwhm_0])

param1=np.array([1,1,1,
                 counts[peaks][3],binss[peaks][3], sig_g,
                 counts[peaks][4],binss[peaks][4], sig_g,
                 counts[peaks][5],binss[peaks][5], sig_g,
                 ])
popt_1, pcov_1 = curve_fit(s_fit, t1[0],t1[1], p0=param1)
perr_1 = np.sqrt(np.diag(pcov_1))
pfwhm_1= np.abs(np.array([fwhm*popt_1[5],fwhm*popt_1[8],fwhm*popt_1[11]]))
pfit_1 = pd.DataFrame([popt_1, perr_1, pfwhm_1])

param2=np.array([1,1,1,
                 counts[peaks][6],binss[peaks][6], sig_g,
                 counts[peaks][7],binss[peaks][7], sig_g,
                 counts[peaks][8],binss[peaks][8], sig_g,
                 ])
popt_2, pcov_2 = curve_fit(s_fit, t2[0],t2[1], p0=param2)
perr_2 = np.sqrt(np.diag(pcov_2))
pfwhm_2= np.abs(np.array([fwhm*popt_2[5],fwhm*popt_2[8],fwhm*popt_2[11]]))
pfit_2 = pd.DataFrame([popt_2, perr_2, pfwhm_2])

''' Save best-fit parameters, standard variation error,
and fwhm_f of each Gaussian peak to a .csv file '''
psave=pd.concat([pfit_0,pfit_1,pfit_2])
psave.to_csv('params.csv', header=False, index=False)

# Plot position spectra with the three fitted superfunctions
plt.figure()
```

```
plt.step(binss[:-1],counts, where='mid')
plt.plot(np.arange(-1,-0.33,0.0001), s_fit(np.arange(-1,-0.33,0.0001), *popt_0),
         ls='--', label='tube_0')
plt.plot(np.arange(-0.33,0.33,0.0001), s_fit(np.arange(-0.33,0.33,0.0001), *popt_1),
         ls='--', label='tube_1')
plt.plot(np.arange(0.33,1,0.0001), s_fit(np.arange(0.33,1,0.0001), *popt_2),
         ls='--', label='tube_2')
plt.xlabel('posx [a.u.]', fontsize=20)
plt.ylabel('Counts', fontsize=20)
plt.legend()
plt.ylim(0)
plt.xlim(-1,1)
plt.tight_layout()
plt.show()
```

Position Spectra over Time

Figures B.6 and B.7 are chosen examples to illustrate the position reconstruction spectra over time. Both figures are from the same measurement run **B**, of configuration B, where figure B.6 is the position spectrum of channel 7, and figure B.7 is the position spectrum of channel 3. There are four spectra within each figure, each representing the spectra at time t, as indicated above each spectrum.

The spectrum of channel 7 over time, where the peaks are distinct in all four spectra, is the expected position reconstruction spectra. For channel 3, a flash peak is observed initially at $t = 1.52$ hr around bin position 0.9. Over time, the flash peak stops rising, and the nine distinct peaks are more apparent. However, at the end of the measurement run, $t = 15.07$ hr, the flash peak has grown again. The idea that a flash peak originates from dust and moisture present on the ^{3}He-tubes could explain the initial growth of a flash peak, but not the later growth of the same flash peak. It is speculated that grounding issues could contribute to this later growth. In general, the factors that lead to a flash peak, when, and to what extent, require further work to be ascertained.

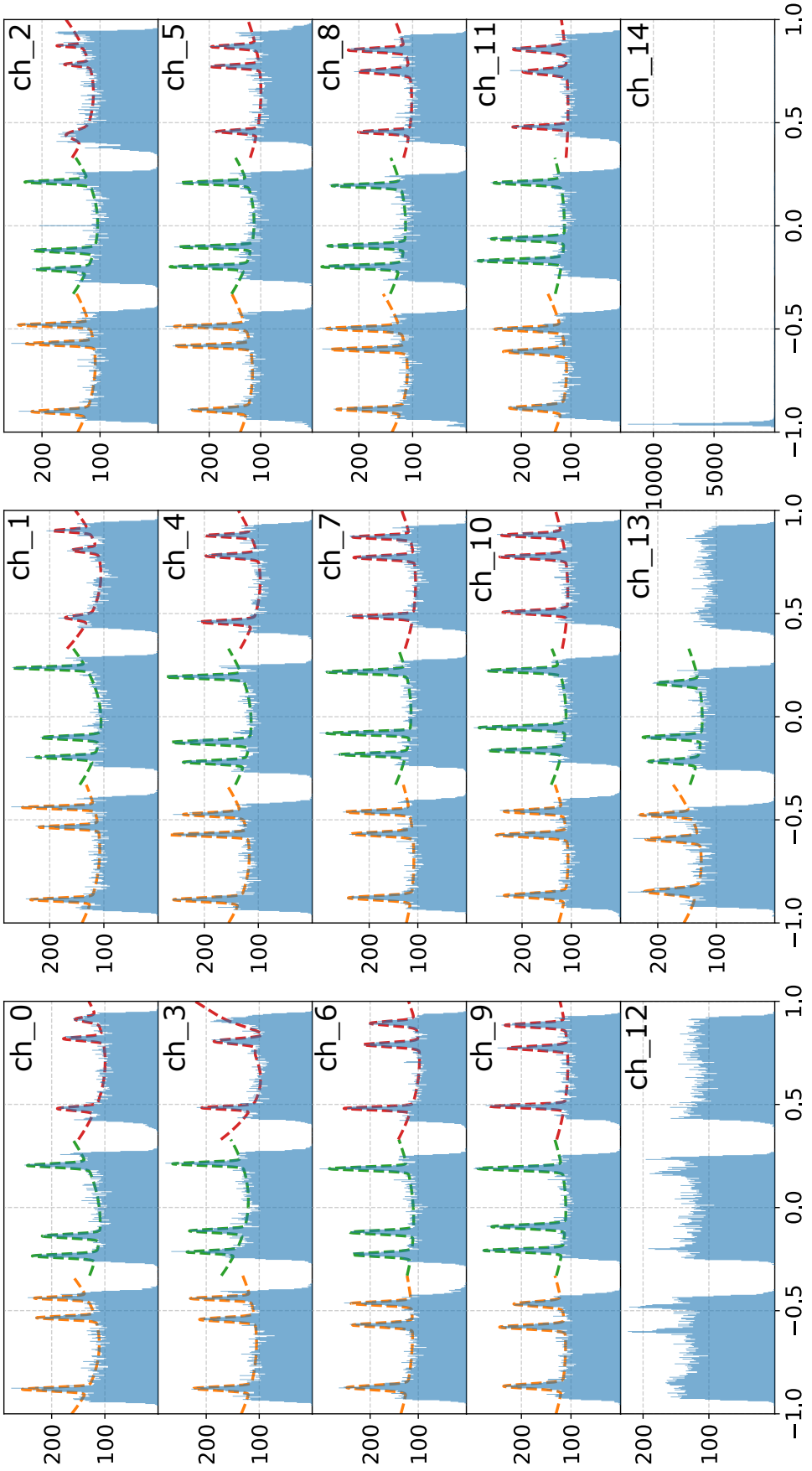

Figure B.1: Position spectra of configuration A, measurement run **A_H**.

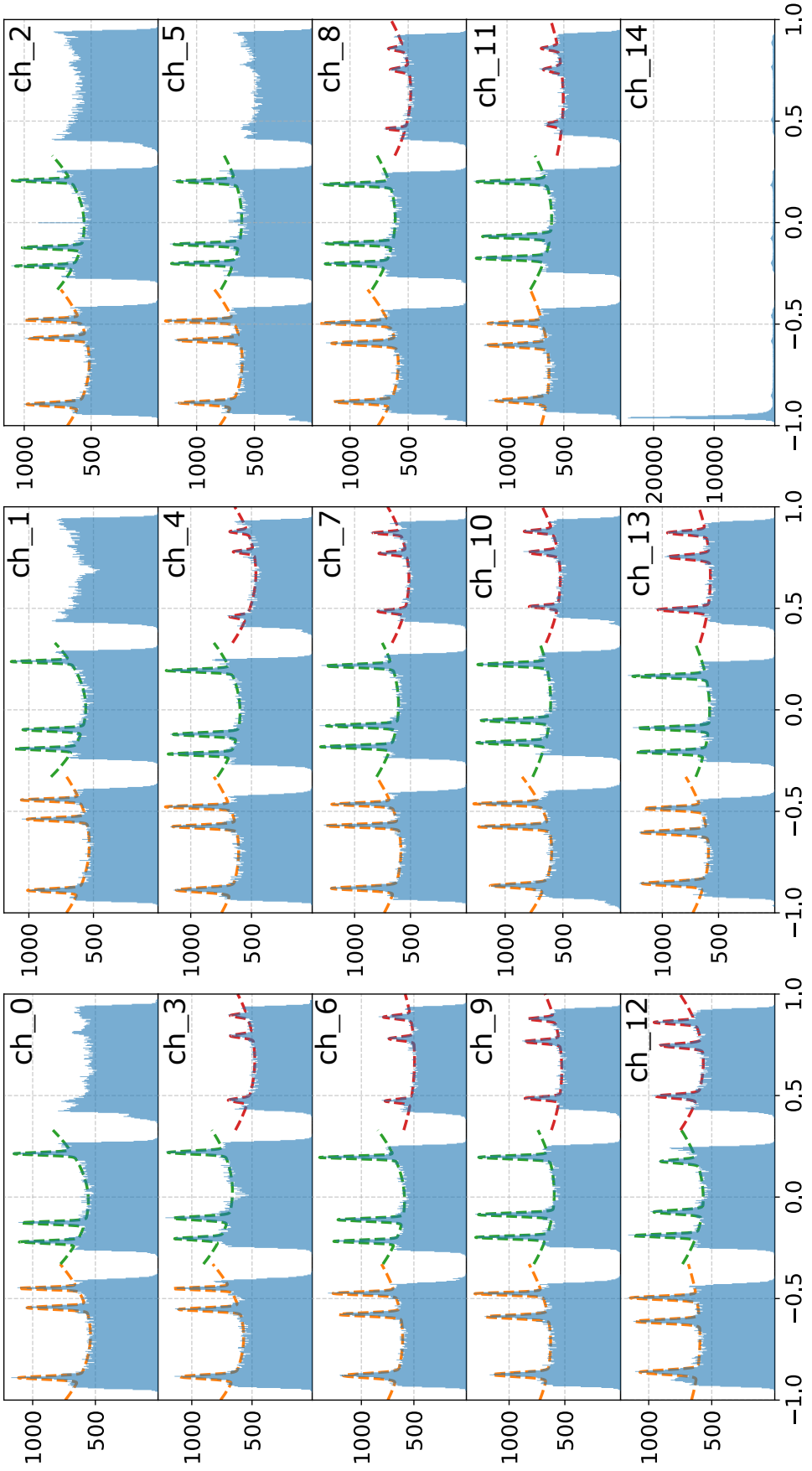

Figure B.2: Position spectra of configuration A, measurement run **A_L**.

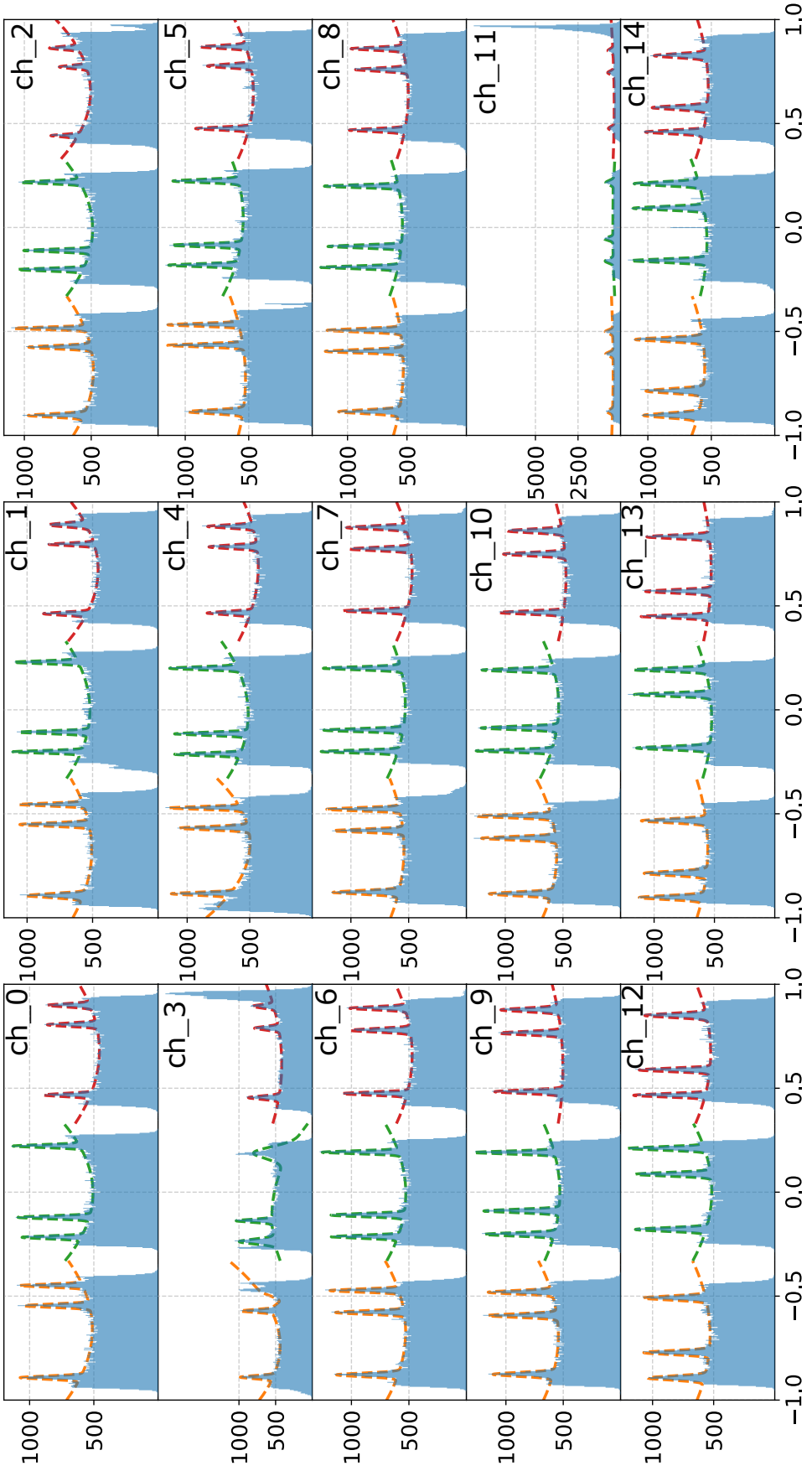

Figure B.3: Position spectra of configuration B, measurement run **B**.

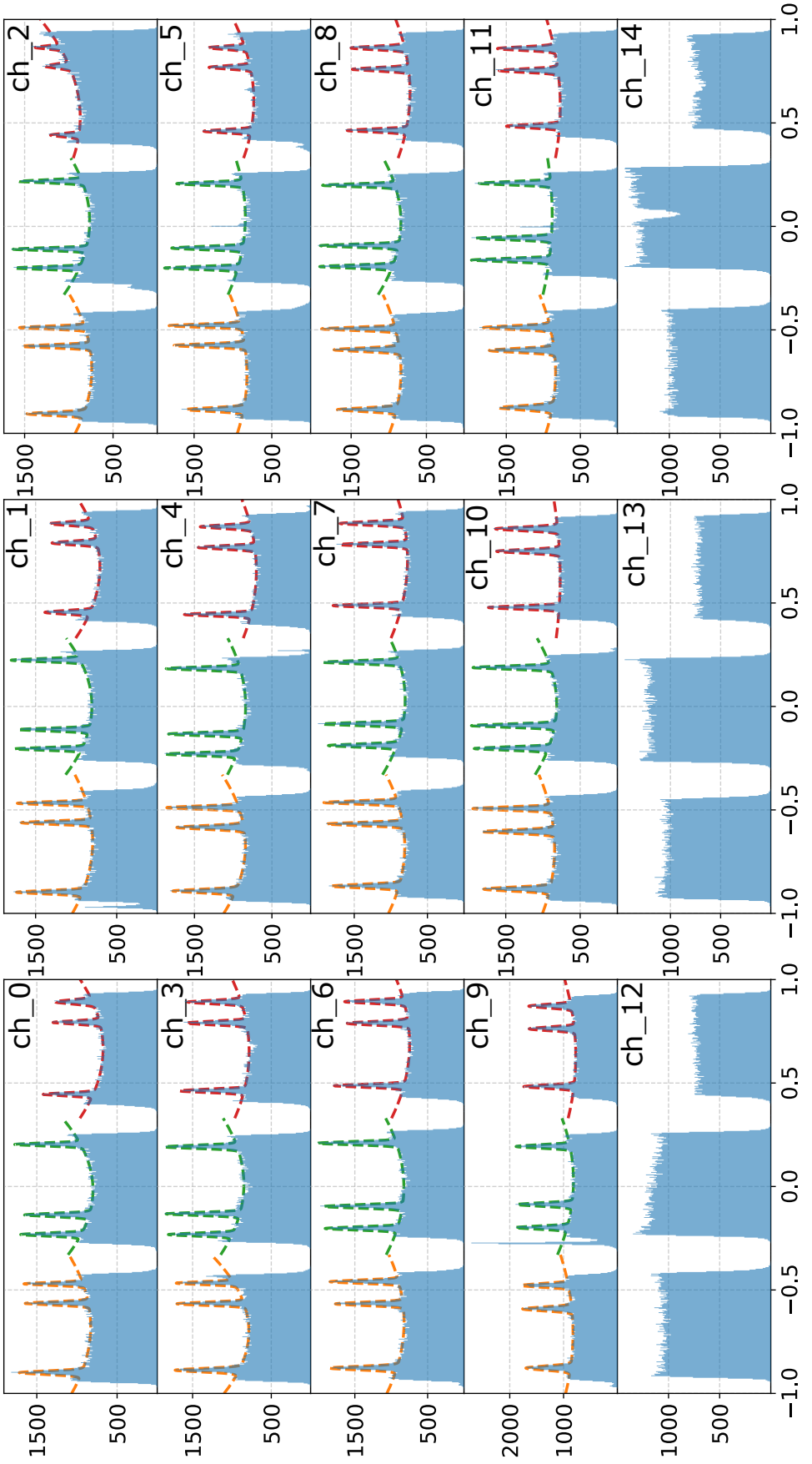

Figure B.4: Position spectra of configuration C, measurement run **C_H**.

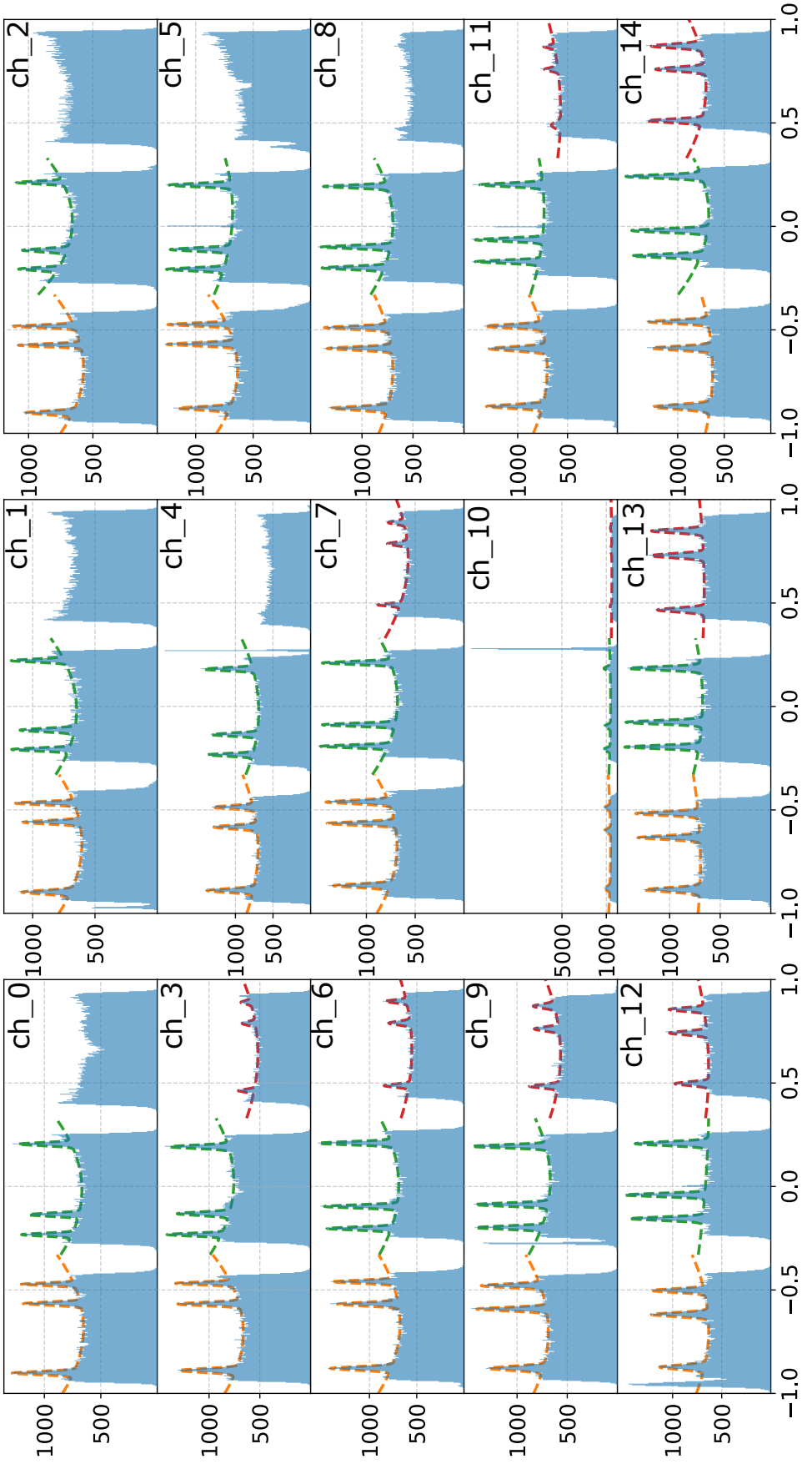

Figure B.5: Position spectra of configuration C, measurement run **C_L**.

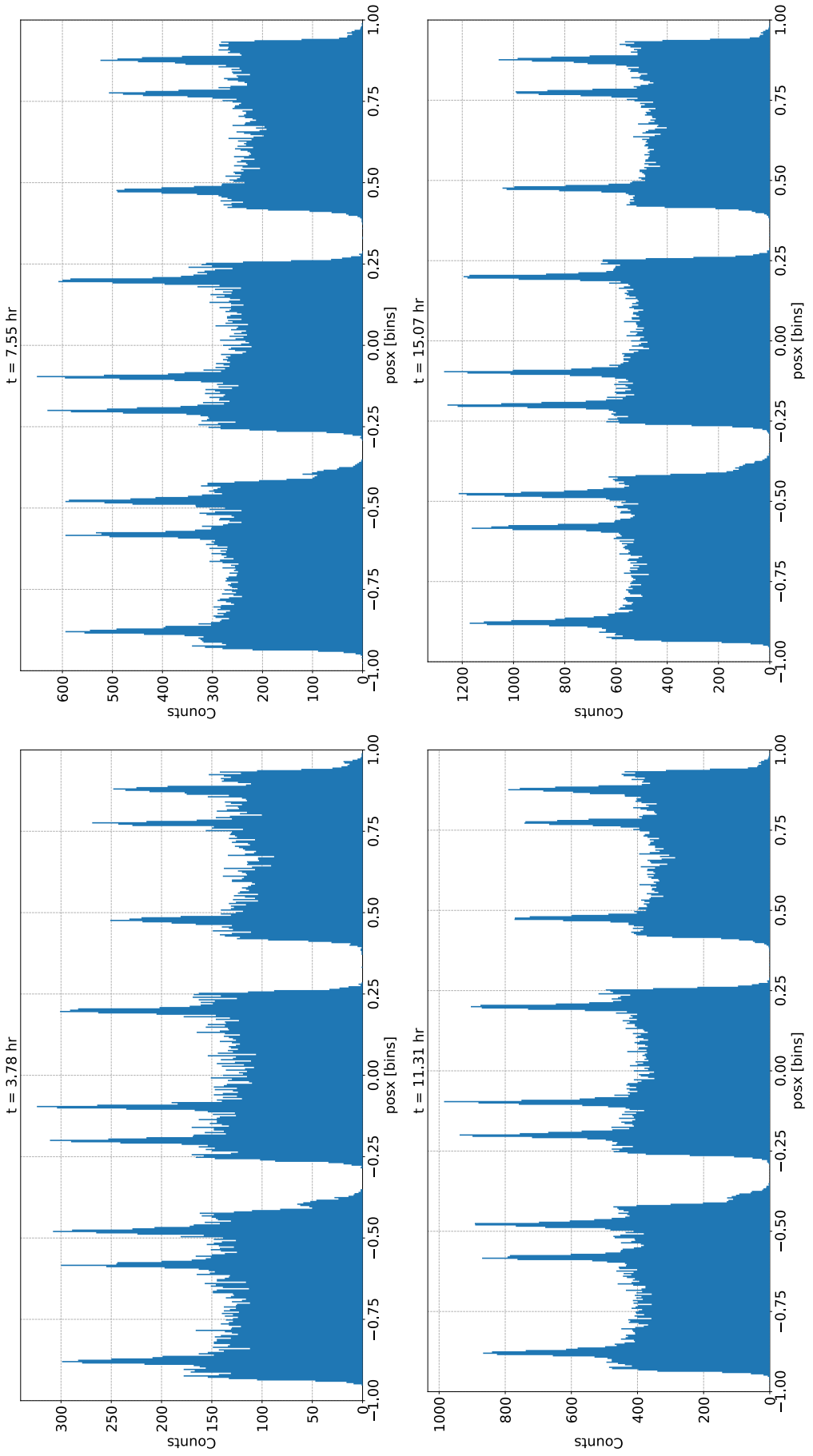

Figure B.6: Position spectra over time of channel 7 of configuration B, measurement run **B**.

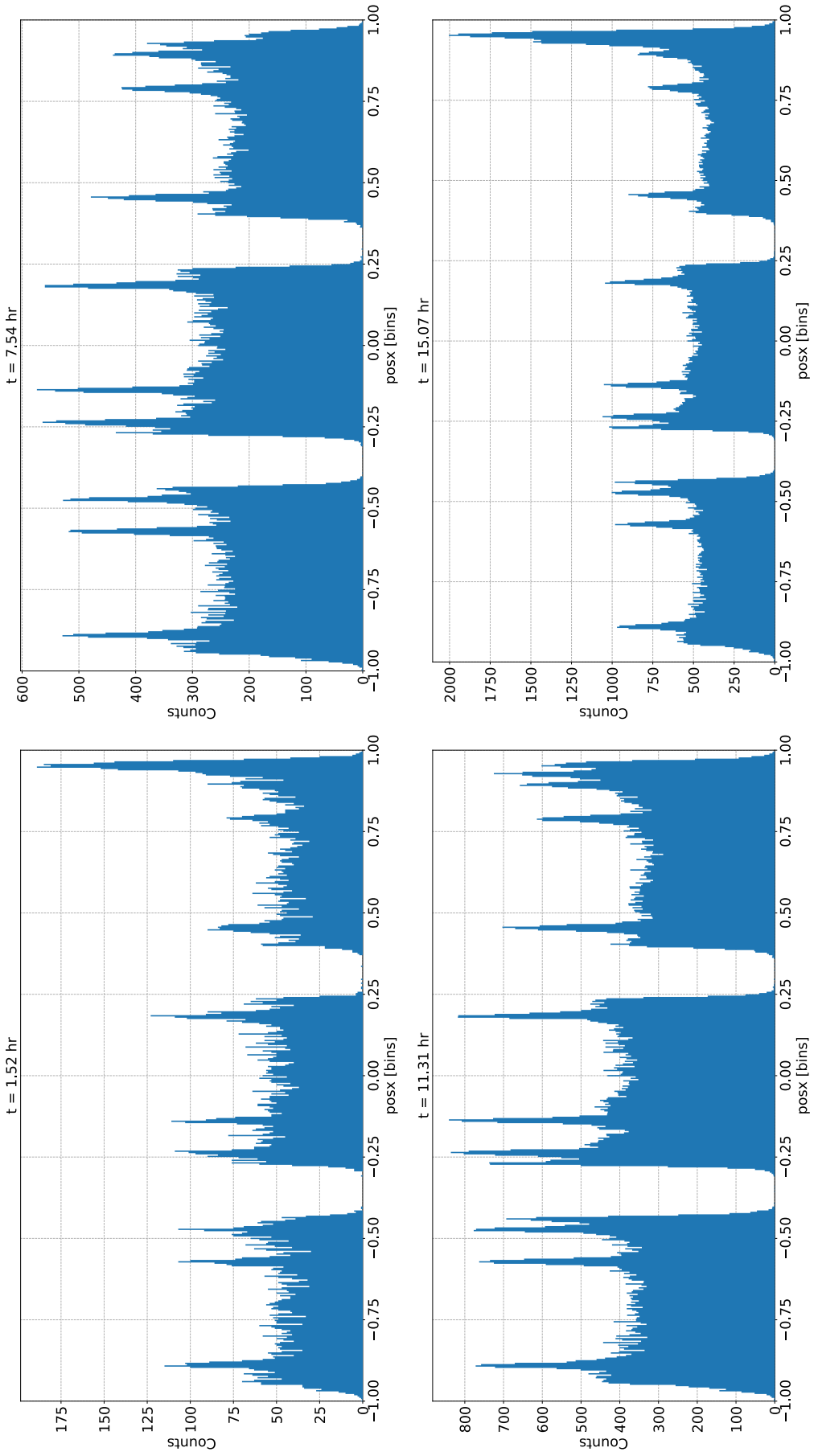

Figure B.7: Position spectra over time of channel 3 of configuration B, measurement run **B**.

Position Reconstruction Resolution and Intrinsic Resolution

The total length (L) of a ^{3}He-tube, and expected position reconstruction resolution FWHM$_k$ ($\sim 1\%$ of $3L$) for an unpacked ^{3}He-triplet ($3L$) is listed in Table C.1. Within the same table, the expected reconstruction resolution FWHM$_k$ ($\sim 1\%$ of L) for individual tubes of a ^{3}He-triplet is listed in parentheses. The expected reconstructed FWHM$_k$ of a ^{3}He-triplet can be compared with the experimental position reconstruction resolution, FWHM$_k$, and the intrinsic resolution, FWHM$_d$, tabulated in Tables C.2 - C.6, for each measurement run. Among the tables, some channels are marked with a † symbol. This denotes that the fitting of the position spectra using the superfunction (Equation 4.1) was not successful, either due to a lack of, or distinction of Gaussian peaks caused by flashing effects or low statistics.

As discussed in Section 4.3.2, the value of reconstructed FWHM$_k$ originates from the standard deviation, σ, by fitting of the position spectra using the superfunction (Equation 4.1). The standard deviation then converted to its FWHM$_f$ equivalent using Equation 4.5, and scaled to a physical range with parameter k from the linear calibration function (Equation 4.3). The uncertainty of reconstructed FWHM$_k$ is derived from the uncertainty of the standard deviation σ, but scaled up with parameter k.

The value of intrinsic FWHM$_d$ is evaluated from reconstructed FWHM$_k$ and FWHM$_s$ of the actual illuminated width X using Equation 4.6. The derivation of Equation 4.6 assumes that each FWHM has a Gaussian shape, and can be expressed in their standard deviation equivalent using Equation 4.5. This allows for the combination of Gaussian distributions, where $\sigma_k = \sqrt{\sigma_d^2 + \sigma_s^2}$. The value of FWHM$_s$ is also defined as the actual illuminated width X, and also assumes that the neutron distribution contributing to the illuminated width is Gaussian shaped. The uncertainty of FWHM$_s$ is from the uncertainty of the thickness t. The thickness of the Cd-mask is estimated, while the embedded depth of a ^{3}He-triplet is measured with a caliper. The uncertainty of intrinsic FWHM$_d$ is then, expressed as the linear combination of the uncertainties of reconstructed FWHM$_k$ and FWHM$_s$, in the form of $\mathrm{err}_d = \sqrt{\mathrm{err}_k^2 + \mathrm{err}_s^2}$, where err is the uncertainty.

The tabulated experimental position reconstruction resolution FWHM$_k$ and expected reconstructed resolution of a ^{3}He-triplet are visualised in Figures C.1 - C.15. The horizontal green dash-dot line denotes the expected reconstructed resolution, i.e. $\sim 1\%$ of $3L$, and the vertical red dashed lines separate the individual tubes in the ^{3}He-triplet. The data points with associated uncertainty values are colour-coded to identify between the five measurement runs (detailed in Appendix A). Missing data points, such as the extreme case seen in Figure C.15, signify the fitting of the position spectra using the superfunction (Equation 4.1) was not successful, and therefore no reconstructed FWHM$_k$ is available. Note that the x-axes of Figures C.1 - C.15 are indices, and therefore no pattern of the data points within each tube should be discerned.

Table C.1: Total length (L) of a tube, expected reconstructed FWHM$_k$ of an unpacked ^{3}He-triplet (and its individual tube in parenthesis) for all 15 ^{3}He-triplets, listed in its corresponding channel number.

Channel #	L **[mm]**	**Expected triplet FWHM$_k$ (tube) [mm]**
0	353.0	10.6 (3.5)
1	346.0	10.4 (3.5)
2	341.0	10.2 (3.4)
3	336.0	10.1 (3.4)
4	329.0	9.9 (3.3)
5	320.0	9.6 (3.2)
6	317.0	9.5 (3.2)
7	310.0	9.3 (3.1)
8	303.0	9.1 (3.0)
9	298.0	8.9 (3.0)
10	291.0	8.7 (2.9)
11	284.0	8.5 (2.8)
12	276.0	8.3 (2.8)
13	268.0	8.0 (2.7)
14	260.0	7.8 (2.6)

Table C.2: Evaluated reconstructed FWHM_k and intrinsic FWHM_d, and corresponding expected reconstructed resolution FWHM_k and total length ($3L$) of the ^{3}He-triplets for configuration A, measurement run **A_H**.

		Channel 0			Channel 1			Channel 2		
Gaussian Peak		i	ii	iii	i	ii	iii	i	ii	iii
FWHM_k [mm]	Tube 0	10.1 ± 0.9	9.6 ± 0.9	8.3 ± 1.0	9.2 ± 0.8	9.6 ± 0.8	8.2 ± 0.7	10.4 ± 1.1	9.4 ± 0.8	8.8 ± 0.7
	Tube 1	10.4 ± 0.9	10.9 ± 0.9	10.7 ± 0.9	9.0 ± 0.8	10.3 ± 0.8	7.9 ± 0.6	9.2 ± 1.2	9.6 ± 1.0	9.9 ± 1.0
	Tube 2	11.3 ± 1.2	10.9 ± 1.2	13.5 ± 2.8	11.9 ± 2.3	10.8 ± 1.9	8.0 ± 1.2	22.5 ± 6.2	8.8 ± 2.1	5.7 ± 1.6
FWHM_d [mm]	Tube 0	9.6 ± 0.9	9.1 ± 0.9	7.7 ± 1.0	8.6 ± 0.8	9.1 ± 0.8	7.6 ± 0.7	10.0 ± 1.1	8.9 ± 0.8	8.2 ± 0.7
	Tube 1	9.9 ± 0.9	10.4 ± 0.9	10.2 ± 0.9	8.5 ± 0.8	9.8 ± 0.8	7.2 ± 0.6	8.7 ± 1.2	9.1 ± 1.0	9.4 ± 1.0
	Tube 2	10.9 ± 1.3	10.4 ± 1.2	13.1 ± 2.8	11.5 ± 2.3	10.4 ± 1.9	7.4 ± 1.2	22.3 ± 6.2	8.2 ± 2.1	4.8 ± 1.6
Expected triplet FWHM_k ($3L$) [mm]		10.6 (1059.0)			10.4 (1038.0)			10.3 (1023.0)		
		Channel 3			Channel 4			Channel 5		
FWHM_k [mm]	Tube 0	10.7 ± 0.8	11.2 ± 0.8	8.8 ± 0.8	10.7 ± 0.8	8.9 ± 0.6	9.9 ± 0.9	10.4 ± 0.8	8.5 ± 0.5	8.9 ± 0.6
	Tube 1	7.9 ± 1.0	9.5 ± 0.9	9.0 ± 0.7	9.4 ± 0.9	10.8 ± 0.7	8.9 ± 0.7	7.9 ± 0.6	7.6 ± 0.6	8.6 ± 0.7
	Tube 2	8.4 ± 0.9	14.3 ± 1.8	45.6 ± 9.5	10.0 ± 0.8	10.7 ± 0.8	8.2 ± 0.8	8.5 ± 1.1	8.8 ± 0.9	9.1 ± 1.0
FWHM_d [mm]	Tube 0	10.2 ± 0.8	10.7 ± 0.9	8.2 ± 0.8	10.2 ± 0.8	8.3 ± 0.6	9.4 ± 0.9	9.9 ± 0.8	7.9 ± 0.5	8.4 ± 0.6
	Tube 1	7.3 ± 1.0	8.9 ± 0.9	8.4 ± 0.7	8.8 ± 0.9	10.4 ± 0.7	8.3 ± 0.7	7.2 ± 0.6	7.0 ± 0.6	8.0 ± 0.7
	Tube 2	7.8 ± 1.0	14.0 ± 1.8	45.4 ± 9.5	9.5 ± 0.8	10.2 ± 0.8	7.5 ± 0.8	7.9 ± 1.1	8.2 ± 0.9	8.6 ± 1.0
Expected triplet FWHM_k ($3L$) [mm]		10.1 (1008.0)			9.9 (987.0)			9.6 (960.0)		
		Channel 6			Channel 7			Channel 8		
FWHM_k [mm]	Tube 0	11.5 ± 0.8	10.6 ± 0.8	9.4 ± 0.8	10.6 ± 0.7	10.2 ± 0.6	9.2 ± 0.6	9.0 ± 0.7	8.6 ± 0.5	9.6 ± 0.6
	Tube 1	10.3 ± 0.8	9.7 ± 0.7	8.8 ± 0.5	7.6 ± 0.6	8.1 ± 0.4	9.2 ± 0.5	8.8 ± 0.6	9.1 ± 0.6	8.6 ± 0.7
	Tube 2	8.2 ± 0.5	10.7 ± 0.7	11.2 ± 1.0	8.6 ± 0.7	9.8 ± 0.7	8.3 ± 0.7	8.4 ± 0.7	11.1 ± 0.8	9.5 ± 0.7
FWHM_d [mm]	Tube 0	11.1 ± 0.8	10.2 ± 0.8	8.9 ± 0.8	10.2 ± 0.7	9.7 ± 0.6	8.6 ± 0.6	8.4 ± 0.7	8.1 ± 0.5	9.1 ± 0.6
	Tube 1	9.8 ± 0.8	9.2 ± 0.7	8.2 ± 0.5	6.9 ± 0.6	7.5 ± 0.5	8.7 ± 0.5	8.3 ± 0.6	8.5 ± 0.6	8.1 ± 0.7
	Tube 2	7.6 ± 0.5	10.2 ± 0.7	10.8 ± 1.0	8.1 ± 0.7	9.3 ± 0.7	7.7 ± 0.7	7.8 ± 0.7	10.6 ± 0.8	9.0 ± 0.7
Expected triplet FWHM_k ($3L$) [mm]		9.5 (951.0)			9.3 (930.0)			9.1 (909.0)		
		Channel 9			Channel 10			Channel 11		
FWHM_k [mm]	Tube 0	10.8 ± 0.8	10.2 ± 0.6	11.1 ± 1.0	11.0 ± 0.7	10.2 ± 0.6	9.4 ± 0.7	10.9 ± 1.0	10.8 ± 0.8	8.8 ± 0.7
	Tube 1	8.0 ± 0.4	9.8 ± 0.5	8.8 ± 0.4	8.4 ± 0.5	9.0 ± 0.4	8.6 ± 0.5	8.1 ± 0.5	8.6 ± 0.5	8.6 ± 0.6
	Tube 2	8.2 ± 0.5	9.5 ± 0.7	9.8 ± 0.8	9.6 ± 0.7	9.5 ± 0.6	8.6 ± 0.7	7.8 ± 0.6	12.1 ± 0.9	11.4 ± 0.8
FWHM_d [mm]	Tube 0	10.4 ± 0.8	9.7 ± 0.6	10.6 ± 1.0	10.5 ± 0.7	9.8 ± 0.6	8.8 ± 0.7	10.4 ± 1	10.4 ± 0.8	8.2 ± 0.7
	Tube 1	7.4 ± 0.5	9.3 ± 0.5	8.2 ± 0.4	7.8 ± 0.5	8.4 ± 0.4	8.0 ± 0.5	7.5 ± 0.5	8.0 ± 0.5	8.0 ± 0.6
	Tube 2	7.5 ± 0.5	9.0 ± 0.7	9.3 ± 0.8	9.0 ± 0.7	9.0 ± 0.6	8 ± 0.7	7.2 ± 0.6	11.7 ± 0.9	11.0 ± 0.8
Expected triplet FWHM_k ($3L$) [mm]		8.9 (894.0)			8.7 (873.0)			8.5 (852.0)		
		Channel 12 †			Channel 13 †			Channel 14 †		
FWHM_k [mm]	Tube 0	-	-	-	13.2 ± 1.3	10.3 ± 1.1	8.2 ± 1.1	-	-	-
	Tube 1	-	-	-	9.1 ± 1.1	8.8 ± 0.8	10.2 ± 1.2	-	-	-
	Tube 2	-	-	-	-	-	-	-	-	-
FWHM_d [mm]	Tube 0	-	-	-	12.8 ± 1.3	9.8 ± 1.1	7.6 ± 1.1	-	-	-
	Tube 1	-	-	-	8.5 ± 1.1	8.2 ± 0.8	9.7 ± 1.2	-	-	-
	Tube 2	-	-	-	-	-	-	-	-	-
Expected triplet FWHM_k ($3L$) [mm]		8.3 (828.0)			8.0 (804.0)			7.8 (780.0)		

Table C.3: Evaluated reconstructed FWHM_k and intrinsic FWHM_d, and corresponding expected reconstructed resolution FWHM_k and total length ($3L$) of the ^{3}He-triplets for configuration A, measurement run **A_L**.

		Channel 0 †			Channel 1 †			Channel 2 †		
Gaussian Peak		i	ii	iii	i	ii	iii	i	ii	iii
FWHM_k [mm]	Tube 0	9.5 ± 0.5	9.8 ± 0.5	7.2 ± 0.5	9.4 ± 0.5	9.3 ± 0.4	7.6 ± 0.4	10.4 ± 0.6	9.2 ± 0.5	7.8 ± 0.5
	Tube 1	8.1 ± 0.5	8.5 ± 0.4	8 ± 0.5	7.2 ± 0.5	8.5 ± 0.5	6.3 ± 0.4	6.9 ± 0.7	8.0 ± 0.7	7.3 ± 0.7
	Tube 2	-	-	-	-	-	-	-	-	-
FWHM_d [mm]	Tube 0	8.9 ± 0.5	9.3 ± 0.5	6.5 ± 0.5	8.9 ± 0.5	8.7 ± 0.4	6.9 ± 0.4	9.9 ± 0.6	8.6 ± 0.5	7.2 ± 0.5
	Tube 1	7.5 ± 0.5	7.9 ± 0.4	7.4 ± 0.5	6.5 ± 0.5	7.9 ± 0.5	5.5 ± 0.4	6.1 ± 0.7	7.4 ± 0.7	6.6 ± 0.7
	Tube 2	-	-	-	-	-	-	-	-	-
Expected triplet FWHM_k ($3L$) [mm]		10.6 (1059.0)			10.4 (1038.0)			10.3 (1023.0)		
		Channel 3			Channel 4			Channel 5 †		
FWHM_k [mm]	Tube 0	11.2 ± 0.6	9.6 ± 0.4	7.3 ± 0.4	11.8 ± 0.7	9.5 ± 0.5	8.1 ± 0.5	9.6 ± 0.6	9.2 ± 0.5	7.4 ± 0.4
	Tube 1	8.3 ± 0.9	10.3 ± 0.7	9 ± 0.7	7.6 ± 0.4	9.7 ± 0.4	8.1 ± 0.4	7.5 ± 0.5	7.9 ± 0.5	8.6 ± 0.6
	Tube 2	9.9 ± 1.1	10.1 ± 0.9	8.6 ± 1.3	8.6 ± 1.4	8.4 ± 1.1	7.9 ± 1.3	-	-	-
FWHM_d [mm]	Tube 0	10.8 ± 0.6	9.0 ± 0.5	6.6 ± 0.5	11.4 ± 0.7	9 ± 0.5	7.4 ± 0.5	9.1 ± 0.6	8.7 ± 0.5	6.7 ± 0.4
	Tube 1	7.7 ± 0.9	9.8 ± 0.7	8.4 ± 0.7	6.9 ± 0.4	9.2 ± 0.4	7.5 ± 0.4	6.9 ± 0.5	7.2 ± 0.5	8 ± 0.6
	Tube 2	9.4 ± 1.1	9.6 ± 0.9	8.1 ± 1.3	8.0 ± 1.4	7.8 ± 1.1	7.3 ± 1.3	-	-	-
Expected triplet FWHM_k ($3L$) [mm]		10.1 (1008.0)			9.9 (987.0)			9.6 (960.0)		
		Channel 6			Channel 7			Channel 8		
FWHM_k [mm]	Tube 0	11.6 ± 0.5	9.1 ± 0.4	7.9 ± 0.4	9.8 ± 0.4	8.0 ± 0.3	7.6 ± 0.4	8.7 ± 0.4	9.8 ± 0.4	8.2 ± 0.4
	Tube 1	7.0 ± 0.3	8.2 ± 0.3	6.7 ± 0.2	7.6 ± 0.4	8.1 ± 0.4	8.2 ± 0.4	7.7 ± 0.4	7.7 ± 0.3	7.6 ± 0.4
	Tube 2	8.9 ± 1.0	9.0 ± 1.1	9.2 ± 1.1	8.9 ± 0.9	8.2 ± 0.7	6.3 ± 0.7	5.6 ± 0.7	10.3 ± 1.0	8.7 ± 1.3
FWHM_d [mm]	Tube 0	11.1 ± 0.5	8.5 ± 0.4	7.3 ± 0.4	9.2 ± 0.4	7.4 ± 0.3	7.0 ± 0.4	8.1 ± 0.5	9.3 ± 0.4	7.6 ± 0.4
	Tube 1	6.3 ± 0.3	7.6 ± 0.3	6.0 ± 0.3	6.9 ± 0.4	7.5 ± 0.4	7.6 ± 0.4	7.1 ± 0.4	7 ± 0.4	7 ± 0.4
	Tube 2	8.3 ± 1.1	8.5 ± 1.1	8.6 ± 1.1	8.3 ± 0.9	7.6 ± 0.7	5.5 ± 0.7	4.7 ± 0.7	9.8 ± 1.1	8.2 ± 1.3
Expected triplet FWHM_k ($3L$) [mm]		9.5 (951.0)			9.3 (930.0)			9.1 (909.0)		
		Channel 9			Channel 10			Channel 11		
FWHM_k [mm]	Tube 0	10.1 ± 0.5	9.0 ± 0.4	6.8 ± 0.3	9.9 ± 0.5	8.3 ± 0.3	6.9 ± 0.3	10.3 ± 0.6	8.8 ± 0.4	7.8 ± 0.5
	Tube 1	7.2 ± 0.3	8.1 ± 0.3	7.9 ± 0.3	7.8 ± 0.3	8.2 ± 0.3	7.9 ± 0.4	7.4 ± 0.3	8.4 ± 0.4	7.5 ± 0.4
	Tube 2	7.6 ± 0.5	8.5 ± 0.5	7.4 ± 0.7	6.9 ± 0.6	9.9 ± 0.7	7.6 ± 0.7	10.5 ± 1.4	11.1 ± 1.2	8 ± 1.1
FWHM_d [mm]	Tube 0	9.6 ± 0.5	8.4 ± 0.4	6.1 ± 0.3	9.4 ± 0.5	7.7 ± 0.3	6.1 ± 0.4	9.8 ± 0.6	8.3 ± 0.4	7.2 ± 0.5
	Tube 1	6.5 ± 0.3	7.5 ± 0.3	7.3 ± 0.3	7.1 ± 0.4	7.6 ± 0.4	7.3 ± 0.5	6.7 ± 0.4	7.8 ± 0.4	6.8 ± 0.4
	Tube 2	7.0 ± 0.5	7.9 ± 0.5	6.7 ± 0.7	6.2 ± 0.6	9.4 ± 0.7	6.9 ± 0.7	10.0 ± 1.4	10.7 ± 1.2	7.4 ± 1.1
Expected triplet FWHM_k ($3L$) [mm]		8.9 (894.0)			8.7 (873.0)			8.5 (852.0)		
		Channel 12			Channel 13			Channel 14 †		
FWHM_k [mm]	Tube 0	10.2 ± 0.5	9.1 ± 0.4	7.9 ± 0.3	9.3 ± 0.4	9.2 ± 0.3	7.8 ± 0.4	-	-	-
	Tube 1	6.9 ± 0.3	8.8 ± 0.5	7.9 ± 0.6	7.3 ± 0.3	7.6 ± 0.3	7.2 ± 0.3	-	-	-
	Tube 2	8.9 ± 0.5	9.2 ± 0.5	7.3 ± 0.5	8.6 ± 0.5	9.8 ± 0.5	8.5 ± 0.6	-	-	-
FWHM_d [mm]	Tube 0	9.8 ± 0.5	8.5 ± 0.4	7.3 ± 0.4	8.8 ± 0.4	8.7 ± 0.4	7.1 ± 0.4	-	-	-
	Tube 1	6.2 ± 0.4	8.2 ± 0.5	7.3 ± 0.6	6.6 ± 0.4	6.9 ± 0.3	6.5 ± 0.3	-	-	-
	Tube 2	8.3 ± 0.6	8.7 ± 0.5	6.6 ± 0.5	8.0 ± 0.5	9.3 ± 0.5	7.9 ± 0.6	-	-	-
Expected triplet FWHM_k ($3L$) [mm]		8.3 (828.0)			8.0 (804.0)			7.8 (780.0)		

Table C.4: Evaluated reconstructed FWHM_k and intrinsic FWHM_d, and corresponding expected reconstructed resolution FWHM_k and total length ($3L$) of the ^{3}He-triplets for configuration B, measurement run **B**.

		Channel 0			Channel 1			Channel 2		
Gaussian Peak		i	ii	iii	i	ii	iii	i	ii	iii
FWHM_k [mm]	Tube 0	9.3 ± 0.5	9.4 ± 0.4	8.4 ± 0.5	11.3 ± 0.6	9.7 ± 0.4	8.0 ± 0.4	9.5 ± 0.5	9.5 ± 0.4	7.1 ± 0.3
	Tube 1	8.1 ± 0.4	8.6 ± 0.4	8.2 ± 0.4	7.4 ± 0.4	8.2 ± 0.4	8.0 ± 0.5	7.6 ± 0.4	7.7 ± 0.4	8.0 ± 0.5
	Tube 2	8.7 ± 0.5	9.5 ± 0.5	9.3 ± 0.6	8.3 ± 0.6	7.7 ± 0.5	10.9 ± 0.8	7.1 ± 0.8	8.7 ± 0.9	8.6 ± 0.9
FWHM_d [mm]	Tube 0	8.7 ± 0.5	8.9 ± 0.5	7.9 ± 0.5	10.9 ± 0.6	9.2 ± 0.4	7.4 ± 0.4	9 ± 0.5	9 ± 0.4	6.4 ± 0.3
	Tube 1	7.5 ± 0.5	8.0 ± 0.4	7.6 ± 0.4	6.7 ± 0.4	7.6 ± 0.4	7.3 ± 0.5	7 ± 0.4	7 ± 0.4	7.4 ± 0.5
	Tube 2	8.1 ± 0.5	9.0 ± 0.5	8.8 ± 0.6	7.7 ± 0.6	7.1 ± 0.5	10.5 ± 0.8	6.4 ± 0.9	8.1 ± 0.9	8.0 ± 0.9
Expected triplet FWHM_k ($3L$) [mm]		10.6 (1059.0)			10.4 (1038.0)			10.3 (1023.0)		
		Channel 3			Channel 4			Channel 5		
FWHM_k [mm]	Tube 0	8.3 ± 0.9	7.3 ± 0.9	22.9 ± 4.3	7.8 ± 0.6	9.6 ± 0.6	7.4 ± 0.5	10.2 ± 0.5	8.3 ± 0.3	7.5 ± 0.3
	Tube 1	12.9 ± 1.7	7.9 ± 1.1	31.9 ± 3.5	7.5 ± 0.4	8.2 ± 0.3	7.9 ± 0.4	7.3 ± 0.4	8.3 ± 0.4	8.2 ± 0.4
	Tube 2	9.0 ± 0.5	9.5 ± 0.7	9.2 ± 0.8	8.6 ± 0.5	9.2 ± 0.4	8.7 ± 0.5	7.5 ± 0.5	9.1 ± 0.6	8.1 ± 0.6
FWHM_d [mm]	Tube 0	7.7 ± 0.9	6.6 ± 0.9	22.7 ± 4.3	7.1 ± 0.6	9.1 ± 0.6	6.7 ± 0.5	9.8 ± 0.5	7.7 ± 0.3	6.9 ± 0.4
	Tube 1	12.5 ± 1.7	7.2 ± 1.1	31.8 ± 3.5	6.8 ± 0.4	7.6 ± 0.3	7.3 ± 0.4	6.7 ± 0.4	7.7 ± 0.4	7.6 ± 0.4
	Tube 2	8.4 ± 0.6	9.0 ± 0.7	8.7 ± 0.8	8.1 ± 0.5	8.7 ± 0.5	8.1 ± 0.5	6.9 ± 0.5	8.6 ± 0.6	7.5 ± 0.6
Expected triplet FWHM_k ($3L$) [mm]		10.1 (1008.0)			9.9 (987.0)			9.6 (960.0)		
		Channel 6			Channel 7			Channel 8		
FWHM_k [mm]	Tube 0	9.2 ± 0.4	8.8 ± 0.3	7.8 ± 0.3	9.7 ± 0.4	8.2 ± 0.4	7.9 ± 0.3	9.6 ± 0.5	8.3 ± 0.3	8.5 ± 0.4
	Tube 1	7.8 ± 0.3	8.2 ± 0.3	7.4 ± 0.3	7.1 ± 0.3	7.7 ± 0.3	7.9 ± 0.3	7.0 ± 0.3	7.5 ± 0.3	6.9 ± 0.3
	Tube 2	7.8 ± 0.3	9.1 ± 0.3	8 ± 0.3	7.7 ± 0.3	8.4 ± 0.3	8.3 ± 0.3	7.8 ± 0.3	8.3 ± 0.4	7.3 ± 0.3
FWHM_d [mm]	Tube 0	8.7 ± 0.4	8.2 ± 0.3	7.2 ± 0.3	9.1 ± 0.4	7.6 ± 0.4	7.3 ± 0.4	9.1 ± 0.5	7.7 ± 0.3	7.9 ± 0.4
	Tube 1	7.1 ± 0.3	7.6 ± 0.3	6.7 ± 0.3	6.4 ± 0.3	7.0 ± 0.3	7.3 ± 0.3	6.3 ± 0.3	6.8 ± 0.3	6.1 ± 0.3
	Tube 2	7.1 ± 0.3	8.6 ± 0.3	7.3 ± 0.4	7.1 ± 0.3	7.8 ± 0.3	7.7 ± 0.4	7.2 ± 0.4	7.7 ± 0.4	6.6 ± 0.4
Expected triplet FWHM_k ($3L$) [mm]		9.5 (951.0)			9.3 (930.0)			9.1 (909.0)		
		Channel 9			Channel 10			Channel 11		
FWHM_k [mm]	Tube 0	9.5 ± 0.4	8.8 ± 0.3	8.4 ± 0.4	8.9 ± 0.4	8.6 ± 0.3	7.7 ± 0.3	8.1 ± 0.5	9.0 ± 0.4	8.3 ± 0.4
	Tube 1	7.9 ± 0.3	8.2 ± 0.3	7.2 ± 0.3	6.6 ± 0.3	7.8 ± 0.3	7.5 ± 0.3	9.1 ± 0.9	7.2 ± 0.7	9.9 ± 1.1
	Tube 2	8.6 ± 0.4	8.5 ± 0.4	8.9 ± 0.5	7.5 ± 0.3	8.5 ± 0.3	8.8 ± 0.4	8.4 ± 0.9	8.5 ± 0.8	7.5 ± 0.9
FWHM_d [mm]	Tube 0	9.0 ± 0.4	8.3 ± 0.3	7.9 ± 0.4	8.4 ± 0.4	8.1 ± 0.3	7.1 ± 0.3	7.5 ± 0.5	8.4 ± 0.4	7.7 ± 0.4
	Tube 1	7.3 ± 0.3	7.6 ± 0.3	6.5 ± 0.3	5.9 ± 0.3	7.2 ± 0.3	6.8 ± 0.3	8.6 ± 0.9	6.5 ± 0.7	9.4 ± 1.1
	Tube 2	8.0 ± 0.4	7.9 ± 0.4	8.4 ± 0.5	6.9 ± 0.3	7.9 ± 0.4	8.2 ± 0.4	7.8 ± 0.9	7.9 ± 0.8	6.8 ± 0.9
Expected triplet FWHM_k ($3L$) [mm]		8.9 (894.0)			8.7 (873.0)			8.5 (852.0)		
		Channel 12			Channel 13			Channel 14		
FWHM_k [mm]	Tube 0	9.3 ± 0.7	8.8 ± 0.6	8.9 ± 0.7	8.5 ± 0.6	9.3 ± 0.7	8.7 ± 0.6	9.8 ± 0.9	9.2 ± 0.8	8.4 ± 0.7
	Tube 1	8.0 ± 0.6	8.0 ± 0.6	7.5 ± 0.5	7.6 ± 0.6	7.1 ± 0.5	7.0 ± 0.5	7.4 ± 0.7	7.4 ± 0.7	8.1 ± 0.9
	Tube 2	7.1 ± 0.5	7.3 ± 0.5	8.9 ± 0.7	6.7 ± 0.5	7.2 ± 0.5	7.9 ± 0.6	7.3 ± 0.6	8.4 ± 0.7	8.2 ± 0.7
FWHM_d [mm]	Tube 0	8.7 ± 0.7	8.2 ± 0.6	8.4 ± 0.7	7.9 ± 0.6	8.8 ± 0.7	8.1 ± 0.6	9.3 ± 0.9	8.7 ± 0.8	7.8 ± 0.7
	Tube 1	7.4 ± 0.6	7.4 ± 0.6	6.8 ± 0.5	6.9 ± 0.6	6.4 ± 0.5	6.3 ± 0.5	6.7 ± 0.7	6.7 ± 0.7	7.5 ± 0.9
	Tube 2	6.4 ± 0.5	6.6 ± 0.5	8.4 ± 0.7	6.0 ± 0.5	6.4 ± 0.5	7.3 ± 0.6	6.6 ± 0.6	7.8 ± 0.7	7.6 ± 0.7
Expected triplet FWHM_k ($3L$) [mm]		8.3 (828.0)			8.0 (804.0)			7.8 (780.0)		

Table C.5: Evaluated reconstructed FWHM_k and intrinsic FWHM_d, and corresponding expected reconstructed resolution FWHM_k and total length ($3L$) of the ^{3}He-triplets for configuration C, measurement run **C_H**.

		Channel 0			Channel 1			Channel 2		
Gaussian Peak		i	ii	iii	i	ii	iii	i	ii	iii
FWHM_k [mm]	Tube 0	10.4 ± 0.4	9.7 ± 0.4	8.3 ± 0.4	9.6 ± 0.3	9.0 ± 0.3	8.3 ± 0.3	9.6 ± 0.5	$9 - 0 \pm 0.4$	8.4 ± 0.4
	Tube 1	8.8 ± 0.4	9.7 ± 0.3	8.5 ± 0.3	7.6 ± 0.3	8.3 ± 0.3	8.5 ± 0.3	7.7 ± 0.4	7.7 ± 0.3	8.6 ± 0.4
	Tube 2	8.9 ± 0.4	9.7 ± 0.4	11.8 ± 0.7	9.5 ± 0.5	10.3 ± 0.4	9.6 ± 0.5	9.4 ± 0.9	11.5 ± 1.1	8.4 ± 1.0
FWHM_d [mm]	Tube 0	10.0 ± 0.4	9.1 ± 0.4	7.7 ± 0.4	9.0 ± 0.4	8.5 ± 0.3	7.7 ± 0.3	9.0 ± 0.5	8.4 ± 0.4	7.8 ± 0.4
	Tube 1	8.2 ± 0.4	9.2 ± 0.4	7.9 ± 0.3	6.9 ± 0.3	7.7 ± 0.3	7.9 ± 0.3	7.1 ± 0.4	7.1 ± 0.3	8 ± 0.4
	Tube 2	8.3 ± 0.4	9.2 ± 0.4	11.4 ± 0.7	9.0 ± 0.5	9.9 ± 0.4	9.1 ± 0.5	8.8 ± 1.0	11.0 ± 1.1	7.8 ± 1.0
Expected triplet FWHM_k ($3L$) [mm]		10.6 (1059.0)			10.4 (1038.0)			10.3 (1023.0)		
		Channel 3			Channel 4			Channel 5		
FWHM_k [mm]	Tube 0	9.9 ± 0.5	8.6 ± 0.4	7.7 ± 0.4	9.7 ± 0.3	10.4 ± 0.3	8.5 ± 0.3	10 ± 0.4	9.0 ± 0.3	8.0 ± 0.3
	Tube 1	8.1 ± 0.4	8.4 ± 0.3	8.8 ± 0.3	7.9 ± 0.3	8.3 ± 0.3	8.4 ± 0.3	7.8 ± 0.4	8.5 ± 0.4	8.3 ± 0.5
	Tube 2	8.9 ± 0.4	9.7 ± 0.4	9.3 ± 0.5	8.4 ± 0.3	9.5 ± 0.3	9.8 ± 0.4	8.7 ± 0.4	8.8 ± 0.5	8.8 ± 0.5
FWHM_d [mm]	Tube 0	9.4 ± 0.5	8.0 ± 0.4	7.1 ± 0.4	9.2 ± 0.3	9.9 ± 0.3	7.9 ± 0.3	9.5 ± 0.4	8.4 ± 0.3	7.4 ± 0.3
	Tube 1	7.5 ± 0.4	7.8 ± 0.3	8.2 ± 0.4	7.2 ± 0.3	7.7 ± 0.3	7.8 ± 0.3	7.1 ± 0.4	7.9 ± 0.4	7.7 ± 0.5
	Tube 2	8.3 ± 0.4	9.2 ± 0.4	8.7 ± 0.5	7.8 ± 0.3	9.0 ± 0.3	9.3 ± 0.4	8.1 ± 0.5	8.2 ± 0.5	8.3 ± 0.6
Expected triplet FWHM_k ($3L$) [mm]		10.1 (1008.0)			9.9 (987.0)			9.6 (960.0)		
		Channel 6			Channel 7			Channel 8		
FWHM_k [mm]	Tube 0	9.2 ± 0.3	8.7 ± 0.3	8.2 ± 0.3	8.9 ± 0.3	8.4 ± 0.2	8.1 ± 0.2	9.3 ± 0.4	9.2 ± 0.3	7.9 ± 0.3
	Tube 1	8.0 ± 0.3	8.4 ± 0.2	8.2 ± 0.2	8.0 ± 0.3	7.9 ± 0.2	8.1 ± 0.2	7.8 ± 0.3	7.8 ± 0.2	7.2 ± 0.3
	Tube 2	8.0 ± 0.3	9.4 ± 0.3	8.7 ± 0.3	7.9 ± 0.2	8.7 ± 0.2	9 ± 0.3	7.7 ± 0.3	8.9 ± 0.4	8.7 ± 0.4
FWHM_d [mm]	Tube 0	8.6 ± 0.3	8.2 ± 0.3	7.6 ± 0.3	8.3 ± 0.3	7.8 ± 0.3	7.5 ± 0.3	8.8 ± 0.4	8.7 ± 0.3	7.2 ± 0.3
	Tube 1	7.4 ± 0.3	7.8 ± 0.2	7.6 ± 0.3	7.3 ± 0.3	7.3 ± 0.2	7.5 ± 0.3	7.1 ± 0.3	7.1 ± 0.3	6.5 ± 0.3
	Tube 2	7.4 ± 0.3	8.9 ± 0.3	8.2 ± 0.4	7.3 ± 0.3	8.1 ± 0.3	8.4 ± 0.3	7.1 ± 0.4	8.3 ± 0.4	8.1 ± 0.4
Expected triplet FWHM_k ($3L$) [mm]		9.5 (951.0)			9.3 (930.0)			9.1 (909.0)		
		Channel 9			Channel 10			Channel 11		
FWHM_k [mm]	Tube 0	10.1 ± 0.4	9.5 ± 0.3	8.6 ± 0.3	9.4 ± 0.4	9.0 ± 0.3	7.7 ± 0.2	10.2 ± 0.5	9.5 ± 0.3	8.7 ± 0.3
	Tube 1	7.5 ± 0.2	8.4 ± 0.2	8.1 ± 0.2	7.7 ± 0.2	8.0 ± 0.2	7.7 ± 0.2	7.5 ± 0.4	7.7 ± 0.4	7.8 ± 0.4
	Tube 2	8.1 ± 0.3	8.6 ± 0.3	8.8 ± 0.3	7.8 ± 0.3	8.8 ± 0.3	9.1 ± 0.3	8.1 ± 0.3	8.5 ± 0.3	8.3 ± 0.3
FWHM_d [mm]	Tube 0	9.6 ± 0.4	9.0 ± 0.3	8.1 ± 0.3	8.9 ± 0.4	8.4 ± 0.3	7.0 ± 0.3	9.8 ± 0.5	9.0 ± 0.3	8.2 ± 0.3
	Tube 1	6.9 ± 0.3	7.8 ± 0.2	7.5 ± 0.3	7.1 ± 0.2	7.3 ± 0.2	7.0 ± 0.2	6.9 ± 0.4	7.0 ± 0.4	7.1 ± 0.4
	Tube 2	7.5 ± 0.3	8.0 ± 0.3	8.2 ± 0.3	7.1 ± 0.3	8.3 ± 0.3	8.5 ± 0.3	7.5 ± 0.3	7.9 ± 0.3	7.7 ± 0.3
Expected triplet FWHM_k ($3L$) [mm]		8.9 (894.0)			8.7 (873.0)			8.5 (852.0)		
		Channel 12 †			Channel 13 †			Channel 14 †		
FWHM_k [mm]	Tube 0	-	-	-	-	-	-	-	-	-
	Tube 1	-	-	-	-	-	-	-	-	-
	Tube 2	-	-	-	-	-	-	-	-	-
FWHM_d [mm]	Tube 0	-	-	-	-	-	-	-	-	-
	Tube 1	-	-	-	-	-	-	-	-	-
	Tube 2	-	-	-	-	-	-	-	-	-
Expected triplet FWHM_k ($3L$) [mm]		8.3 (828.0)			8.0 (804.0)			7.8 (780.0)		

Table C.6: Evaluated reconstructed FWHM_k and intrinsic FWHM_d, and corresponding expected reconstructed resolution FWHM_k and total length ($3L$) of the ^{3}He-triplets for configuration C, measurement run **C_L**.

		Channel 0 †			Channel 1 †			Channel 2 †		
Gaussian Peak		i	ii	iii	i	ii	iii	i	ii	iii
FWHM_k [mm]	Tube 0	9.6 ± 0.4	9.3 ± 0.4	7.9 ± 0.4	10.9 ± 0.6	10.0 ± 0.5	8.5 ± 0.4	10.3 ± 0.8	8.3 ± 0.5	8.3 ± 0.5
	Tube 1	8.4 ± 0.5	9.5 ± 0.5	9.0 ± 0.5	8.4 ± 0.6	9.6 ± 0.6	8.5 ± 0.6	8.3 ± 0.8	9.3 ± 0.7	7.8 ± 0.6
	Tube 2	-	-	-	-	-	-	-	-	-
FWHM_d [mm]	Tube 0	9.1 ± 0.4	8.8 ± 0.4	7.2 ± 0.4	10.5 ± 0.6	9.5 ± 0.5	7.9 ± 0.4	9.9 ± 0.8	7.7 ± 0.5	7.7 ± 0.5
	Tube 1	7.8 ± 0.5	9.0 ± 0.5	8.4 ± 0.5	7.8 ± 0.6	9.1 ± 0.6	7.9 ± 0.6	7.7 ± 0.8	8.8 ± 0.7	7.2 ± 0.7
	Tube 2	-	-	-	-	-	-	-	-	-
Expected triplet FWHM_k ($3L$) [mm]		10.6 (1059.0)			10.4 (1038.0)			10.3 (1023.0)		
		Channel 3			Channel 4 †			Channel 5 †		
FWHM_k [mm]	Tube 0	10.6 ± 0.5	9.0 ± 0.4	7.8 ± 0.4	10.4 ± 0.5	10.5 ± 0.5	9.0 ± 0.5	9.5 ± 0.7	9.0 ± 0.5	7.8 ± 0.5
	Tube 1	7.5 ± 0.5	9.9 ± 0.5	9.4 ± 0.5	7.7 ± 0.3	8.7 ± 0.3	8.4 ± 0.3	8.3 ± 0.9	8.9 ± 0.9	8.9 ± 0.9
	Tube 2	7.9 ± 1	9.9 ± 1.3	8.7 ± 2.2	-	-	-	-	-	-
FWHM_d [mm]	Tube 0	10.1 ± 0.5	8.5 ± 0.4	7.2 ± 0.4	10.0 ± 0.5	10.0 ± 0.5	8.4 ± 0.5	9.0 ± 0.7	8.5 ± 0.5	7.1 ± 0.5
	Tube 1	6.8 ± 0.5	9.4 ± 0.5	8.8 ± 0.5	7.1 ± 0.4	8.2 ± 0.4	7.8 ± 0.4	7.7 ± 0.9	8.4 ± 0.9	8.3 ± 0.9
	Tube 2	7.3 ± 1.0	9.4 ± 1.3	8.1 ± 2.2	-	-	-	-	-	-
Expected triplet FWHM_k ($3L$) [mm]		10.1 (1008.0)			9.9 (987.0)			9.6 (960.0)		
		Channel 6			Channel 7			Channel 8 †		
FWHM_k [mm]	Tube 0	9.2 ± 0.4	9.4 ± 0.4	7.8 ± 0.4	9.6 ± 0.4	9.0 ± 0.3	9.0 ± 0.4	9.7 ± 0.5	8.9 ± 0.4	8.6 ± 0.4
	Tube 1	7.8 ± 0.3	7.9 ± 0.3	8.3 ± 0.3	7.4 ± 0.3	7.9 ± 0.3	7.8 ± 0.3	8.0 ± 0.4	8.1 ± 0.3	7.8 ± 0.4
	Tube 2	8.2 ± 0.6	9.4 ± 0.7	7.7 ± 0.7	6.4 ± 0.7	8.8 ± 0.9	8.4 ± 1.2	-	-	-
FWHM_d [mm]	Tube 0	8.7 ± 0.4	8.9 ± 0.4	7.2 ± 0.4	9.1 ± 0.4	8.4 ± 0.3	8.4 ± 0.4	9.2 ± 0.5	8.4 ± 0.4	8.0 ± 0.5
	Tube 1	7.1 ± 0.3	7.3 ± 0.3	7.7 ± 0.3	6.7 ± 0.3	7.2 ± 0.3	7.2 ± 0.3	7.4 ± 0.4	7.5 ± 0.4	7.2 ± 0.4
	Tube 2	7.6 ± 0.6	8.9 ± 0.7	7.0 ± 0.7	5.6 ± 0.7	8.3 ± 0.9	7.8 ± 1.2	-	-	-
Expected triplet FWHM_k ($3L$) [mm]		9.5 (951.0)			9.3 (930.0)			9.1 (909.0)		
		Channel 9			Channel 10			Channel 11		
FWHM_k [mm]	Tube 0	10.4 ± 0.5	9 ± 0.3	8.8 ± 0.4	9.7 ± 0.4	9.3 ± 0.3	8.2 ± 0.3	9.1 ± 0.5	10.5 ± 0.5	8.9 ± 0.4
	Tube 1	7.9 ± 0.3	8.4 ± 0.3	7.7 ± 0.3	7.2 ± 0.3	8.1 ± 0.3	8.6 ± 0.3	7.4 ± 0.6	7.8 ± 0.6	8.6 ± 0.7
	Tube 2	8.4 ± 0.6	10 ± 0.8	9.9 ± 1.0	9.5 ± 1.1	12.0 ± 1.4	10.9 ± 2	14.8 ± 3.5	8.3 ± 1.3	6.6 ± 1.5
FWHM_d [mm]	Tube 0	10 ± 0.5	8.5 ± 0.3	8.3 ± 0.4	9.1 ± 0.4	8.8 ± 0.3	7.6 ± 0.3	8.5 ± 0.5	10.1 ± 0.5	8.4 ± 0.5
	Tube 1	7.2 ± 0.3	7.8 ± 0.3	7.1 ± 0.3	6.5 ± 0.3	7.4 ± 0.3	8.0 ± 0.4	6.7 ± 0.6	7.1 ± 0.6	8.0 ± 0.7
	Tube 2	7.9 ± 0.7	9.5 ± 0.8	9.4 ± 1.0	8.9 ± 1.1	11.6 ± 1.4	10.4 ± 2.0	14.4 ± 3.5	7.7 ± 1.3	5.8 ± 1.5
Expected triplet FWHM_k ($3L$) [mm]		8.9 (894.0)			8.7 (873.0)			8.5 (852.0)		
		Channel 12			Channel 13			Channel 14 †		
FWHM_k [mm]	Tube 0	10.3 ± 0.5	9.5 ± 0.4	8.4 ± 0.4	9.7 ± 0.5	8.5 ± 0.3	8.4 ± 0.4	10.8 ± 0.5	9.2 ± 0.4	8.2 ± 0.4
	Tube 1	7.9 ± 0.5	7.6 ± 0.3	9.1 ± 0.5	7.4 ± 0.3	8.2 ± 0.3	8.1 ± 0.3	7.5 ± 0.3	8.2 ± 0.3	7.9 ± 0.3
	Tube 2	8.4 ± 0.7	8.7 ± 0.5	8.0 ± 0.6	9.1 ± 0.5	9.3 ± 0.4	8.4 ± 0.4	7.6 ± 0.4	9.0 ± 0.4	8.6 ± 0.5
FWHM_d [mm]	Tube 0	9.8 ± 0.6	9 ± 0.4	7.8 ± 0.4	9.1 ± 0.5	7.9 ± 0.4	7.8 ± 0.4	10.3 ± 0.5	8.7 ± 0.4	7.6 ± 0.4
	Tube 1	7.3 ± 0.5	6.9 ± 0.4	8.6 ± 0.5	6.8 ± 0.3	7.6 ± 0.3	7.4 ± 0.3	6.8 ± 0.3	7.6 ± 0.3	7.3 ± 0.3
	Tube 2	7.8 ± 0.7	8.2 ± 0.5	7.4 ± 0.6	8.5 ± 0.5	8.8 ± 0.4	7.8 ± 0.4	6.9 ± 0.4	8.4 ± 0.4	8.0 ± 0.5
Expected triplet FWHM_k ($3L$) [mm]		8.3 (828.0)			8.0 (804.0)			7.8 (780.0)		

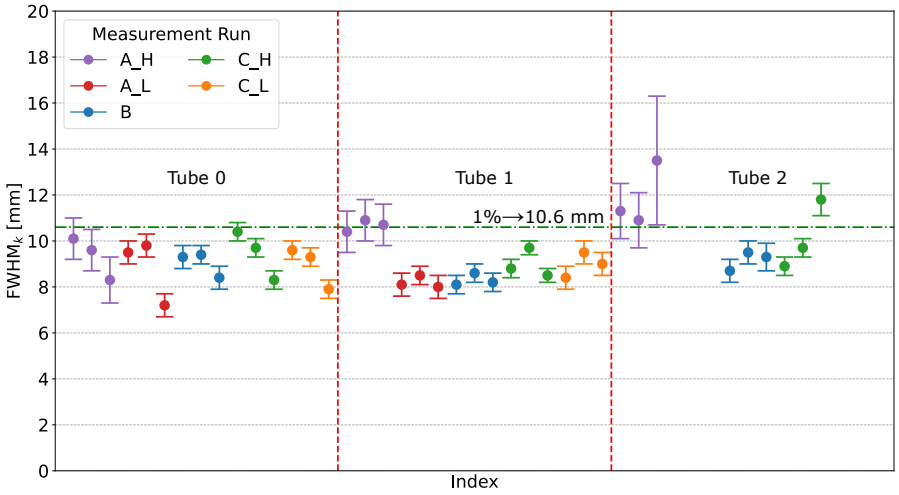

Figure C.1: Index of evaluated reconstructed FWHM$_k$ for channel 0 of all five measurement runs.

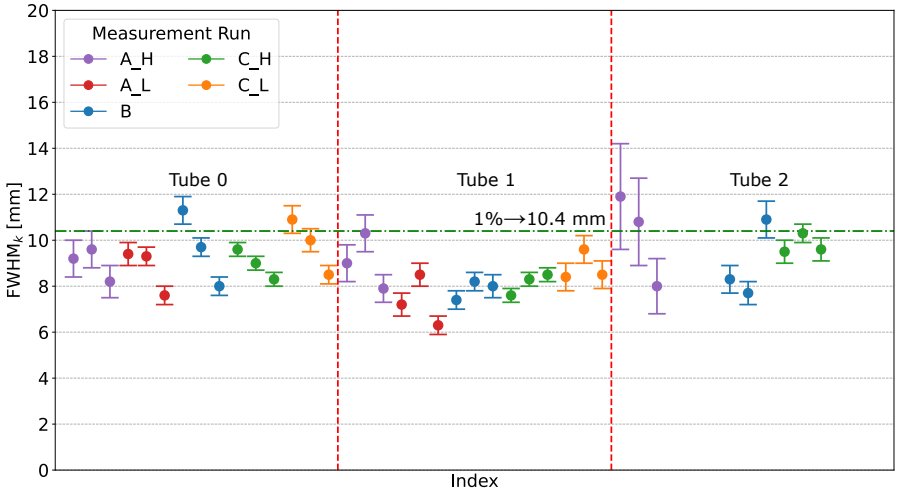

Figure C.2: Index of evaluated reconstructed FWHM$_k$ for channel 1 of all five measurement runs.

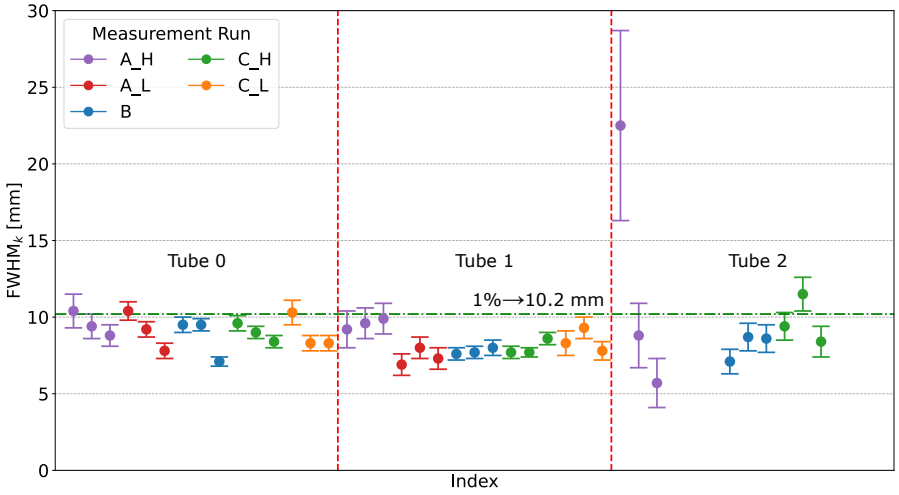

Figure C.3: Index of evaluated reconstructed FWHM$_k$ for channel 2 of all five measurement runs.

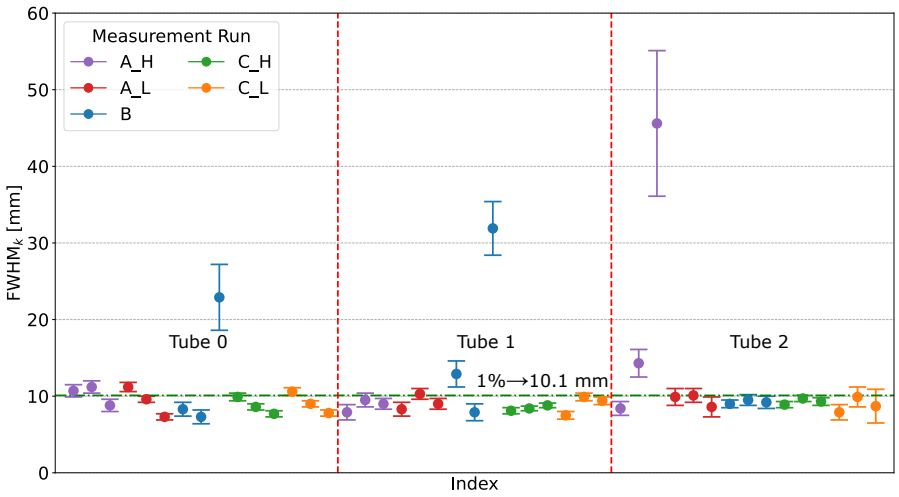

Figure C.4: Index of evaluated reconstructed FWHM$_k$ for channel 3 of all five measurement runs.

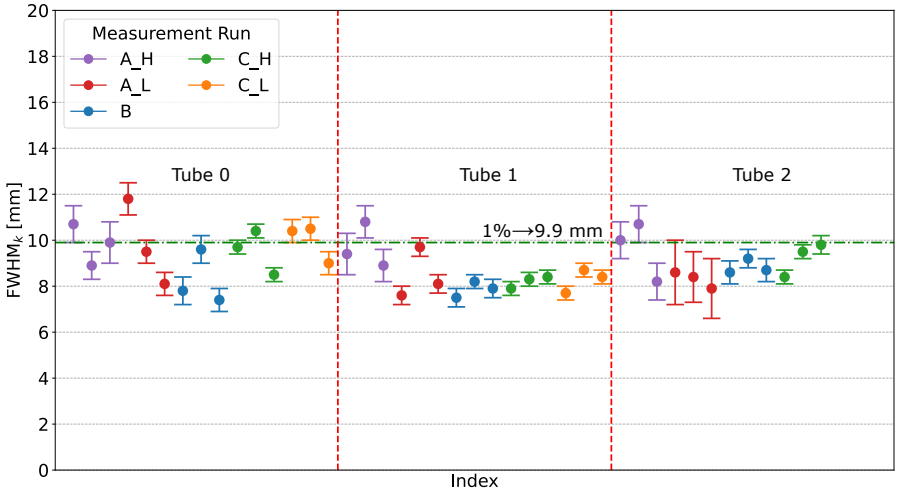

Figure C.5: Index of evaluated reconstructed FWHM$_k$ for channel 4 of all five measurement runs.

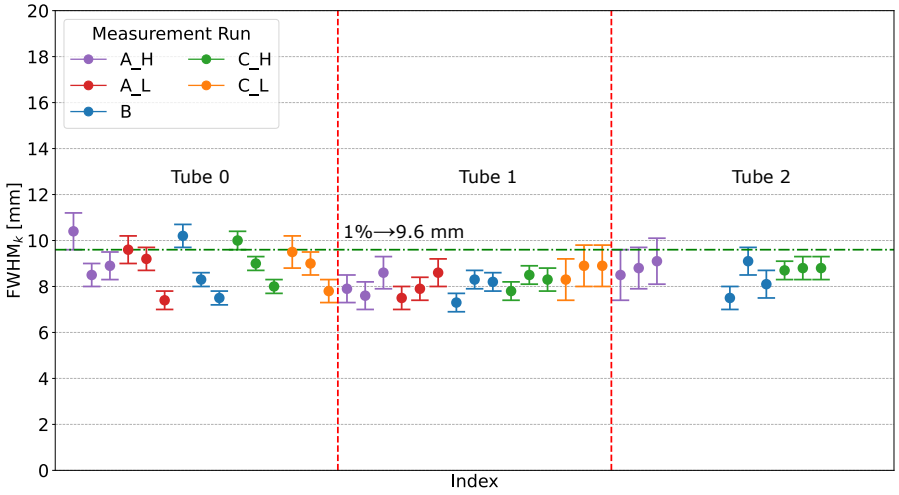

Figure C.6: Index of evaluated reconstructed FWHM$_k$ for channel 5 of all five measurement runs.

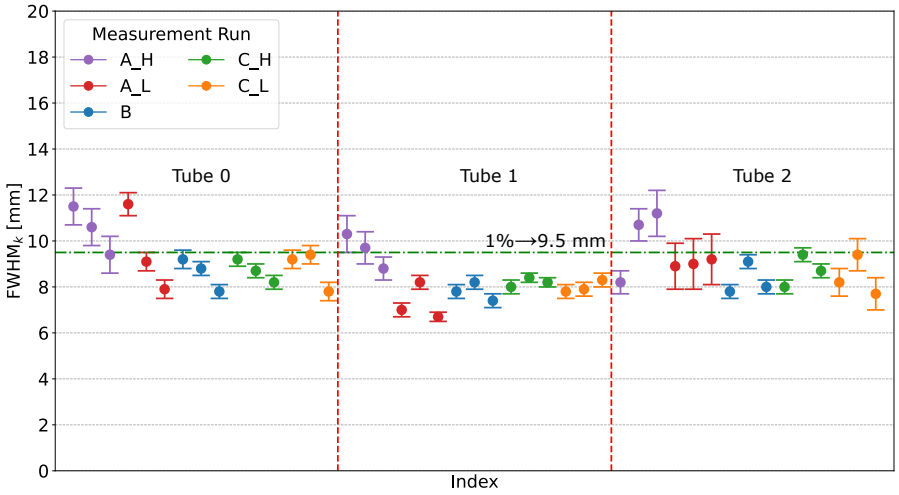

Figure C.7: Index of evaluated reconstructed FWHM$_k$ for channel 6 of all five measurement runs.

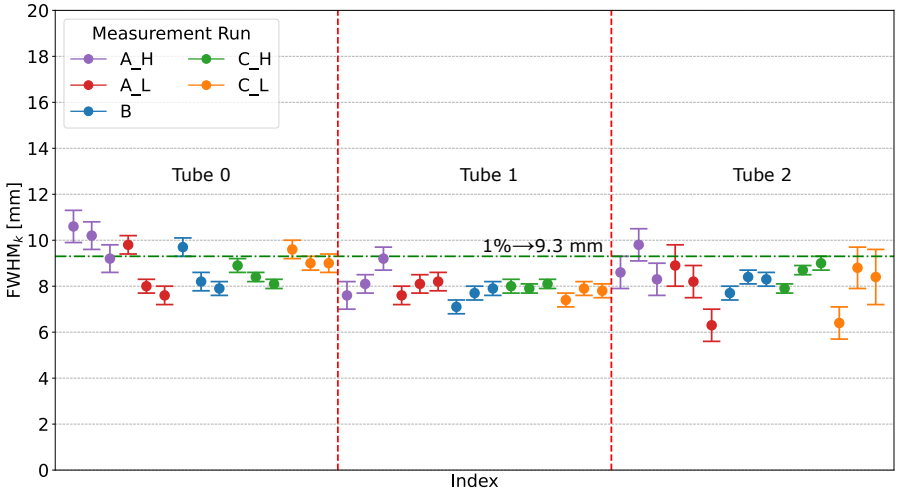

Figure C.8: Index of evaluated reconstructed FWHM$_k$ for channel 7 of all five measurement runs.

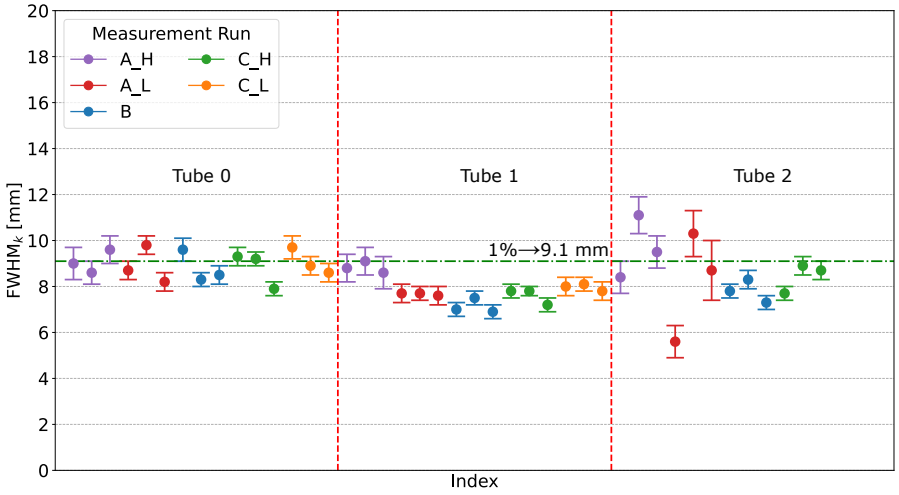

Figure C.9: Index of evaluated reconstructed FWHM$_k$ for channel 8 of all five measurement runs.

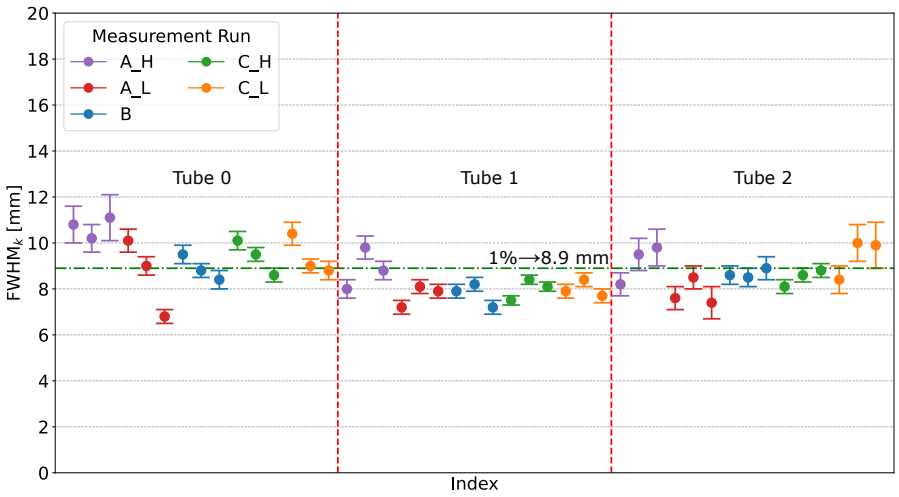

Figure C.10: Index of evaluated reconstructed FWHM$_k$ for channel 9 of all five measurement runs.

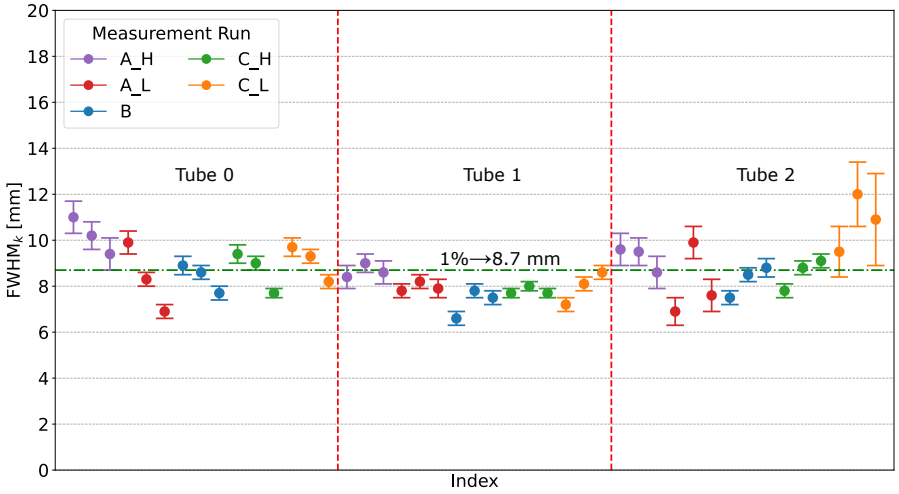

Figure C.11: Index of evaluated reconstructed FWHM$_k$ for channel 10 of all five measurement runs.

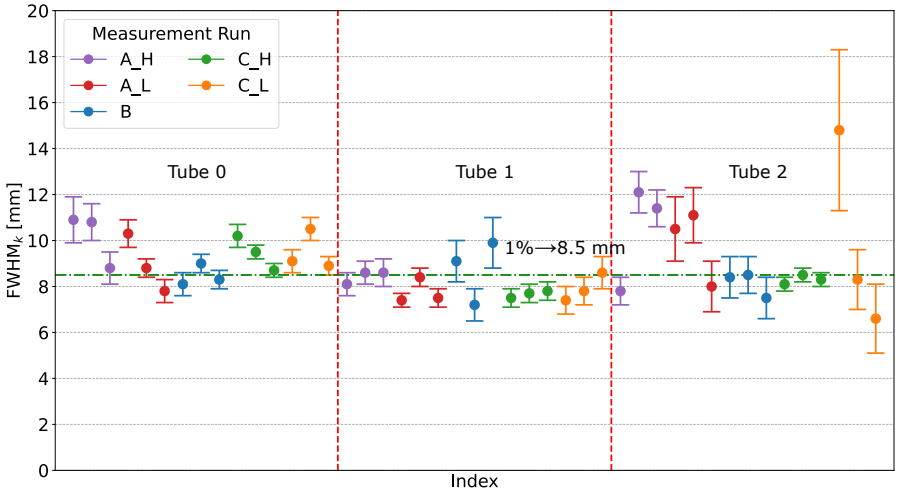

Figure C.12: Index of evaluated reconstructed FWHM$_k$ for channel 11 of all five measurement runs.

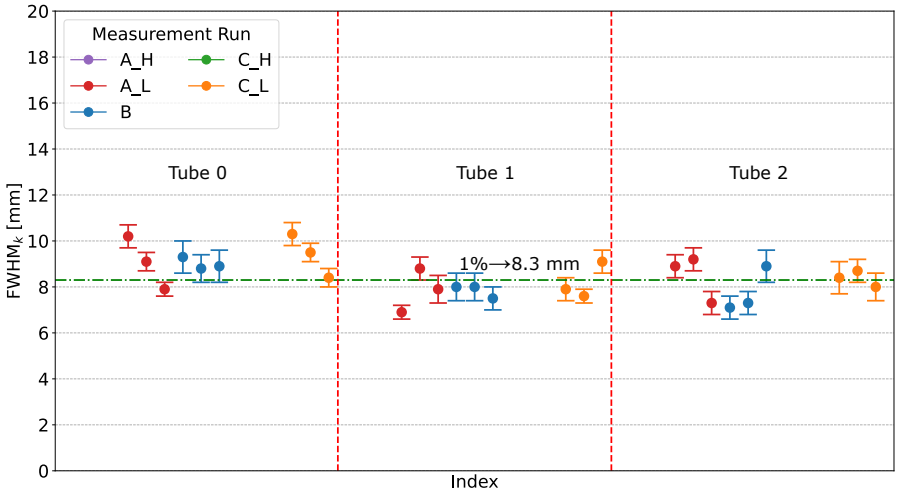

Figure C.13: Index of evaluated reconstructed FWHM$_k$ for channel 12 of all five measurement runs.

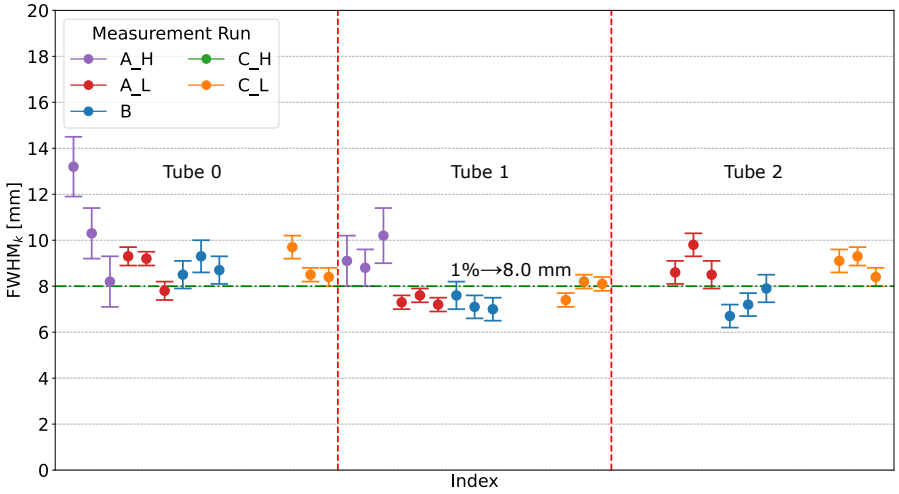

Figure C.14: Index of evaluated reconstructed FWHM$_k$ for channel 13 of all five measurement runs.

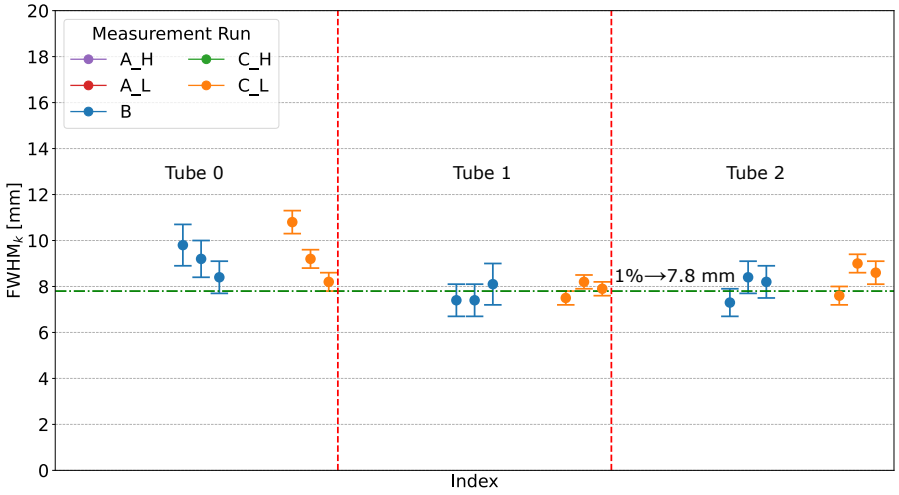

Figure C.15: Index of evaluated reconstructed FWHM$_k$ for channel 14 of all five measurement runs.